UNIVERSITÀ DEGLI STUDI DI BARI

Dipartimento Interateneo di Fisica "M. Merlin"

DOTTORATO DI RICERCA IN FISICA

Ciclo XXXII

Settore scientifico disciplinare Fis/01

The CMS RPC system upgrade project for HL-LHC

Supervisore:

Ch.ma Prof.ssa Gabriella Pugliese

Dottorando:

Dott. Andrea Gelmi

Coordinatore:

Ch.mo Prof. Giuseppe Iaselli

ESAME FINALE 2020

Contents

1 Introduction **1**

2 Physics research at LHC **3**

2.1 The Large Hadron Collider (LHC) 3

2.1.1 LHC parameters and performance 3

2.1.2 High Luminosity-LHC (HL-LHC) 5

2.1.3 LHC experiments 7

3 The Compact Muon Solenoid (CMS) experiment and its upgrade for HL-LHC **9**

3.1 Overview of the CMS detector 9

3.1.1 The solenoid magnet 10

3.1.2 The tracker system 11

3.1.3 The calorimeter system 12

3.1.3.1 Electromagnetic Calorimeter 12

3.1.3.2 Hadron Calorimeter 13

3.1.4 The muon spectrometer 13

3.1.4.1 Drift Tubes 14

3.1.4.2 Cathode Strip Chambers 15

3.1.4.3 Resistive Plate Chambers 16
3.1.5 The trigger 20
3.2 The CMS upgrade project for HL-LHC 21
3.2.1 The CMS Muon system upgrade 23

4 Aging studies on CMS RPC **27**
4.1 Aging studies of the CMS RPC system during LHC 27
4.1.1 Background radiation study 27
4.1.2 Performance study 30
4.1.3 Current study 31
4.2 Hydrogen Fluoride (HF) study 34
4.2.1 HF study at GIF++ 35
4.2.2 HF study in CMS 40
4.3 Long-term aging studies on CMS RPC for HL-LHC 43
4.3.1 Detectors parameters monitoring 47
4.3.2 Detectors performance monitoring 51

5 Extension of the CMS RPC system to the very forward region **61**
5.1 iRPC technology 62
5.1.1 iRPC performance at GIF++ 64
5.1.2 The new iRPC front-end electronics 65
5.2 iRPC sensitivity study and background rate estimation at HL-LHC . . 69
5.2.1 iRPC sensitivity study at GIF++ 69
5.2.2 Background rate study for the iRPC at HL-LHC 73
5.3 iRPC longevity studies 76
5.3.1 Detector parameters and performance monitoring 77
5.3.2 HPL surface analysis 80
5.3.3 Oiling improvement test 87

6 Search for RPC eco-friendly gas mixture **91**

6.1 Eco-friendly gas mixture characterization under irradiation at GIF++ . 93

6.2 Longevity test at GIF++ using eco-friendly gas mixture 96

6.3 HF study using eco-friendly gas mixture 98

7 L1 Muon trigger study **99**

7.1 Optimization of the RPC cluster size cut for the L1 muon trigger . . . 102

8 Conclusions **109**

List of Figures **112**

List of Tables **122**

Bibliography **125**

1 Introduction

This PhD thesis is devoted to the upgrade project of the Resistive Plate Chambers (RPC) system of the CERN Compact Muon Solenoid (CMS) experiment in view of High Luminosity-LHC (HL-LHC), when the accelerator instantaneous luminosity will increase by a factor 5. After a brief introduction about the LHC and the CMS experiment, the RPC upgrade project is described in details, each chapter concerns a different aspect of the project.

- Chapter 2 **Physics research at LHC**:

  a brief overview of the Large Hadron Collider is given, describing its characteristics, parameters, performance and the future plan about the HL-LHC.

- Chapter 3 **The Compact Muon Solenoid (CMS) experiment and its upgrade for HL-LHC**:

  the CMS experiment is described, focusing on the muon spectrometer. The CMS upgrade projects in view of HL-LHC is summarized, with particular regards to the muon upgrade project, and in more details for the RPC upgrade project.

- Chapter 4 **Aging studies on CMS RPC**:

  in this chapter is presented the longevity study for the RPC system during LHC period. The RPC system performance has been studied during the first seven years of operation. The Hydrogen Fluoride (HF) production in the RPC has been studied at GIF++ and in CMS, as a possible cause of the detector aging.

  Finally, a detailed description of the longevity studies ongoing at GIF++ to certify the RPC system for HL-LHC is given. After having collected a significant

amount of integrated charge, the study and the monitoring of the main detector performance and parameters are reported.

- Chapter 5 **Extension of the CMS RPC system at the very forward region**:

  in this chapter is reported the RPC system extension project at the high eta region. The new detectors developed to instrument the RE3-4/1 stations are described. The detector sensitivity has been studied using Monte Carlo methods in order to estimate the expected background rate during HL-LHC, and therefore to define the minimum detector rate capability.

  The detectors performance has been studied at GIF++ to validate the detector technology and the new front end electronics board at the expected background.

  Finally, preliminary results about the detectors longevity studies at GIF++ are reported.

- Chapter 6 **Search for RPC eco-friendly gas mixture**:

  a collaboration among CMS, ATLAS, ALICE and CERN EP-DT groups was set up to search an RPC eco-friendly gas mixture. A new ecogas mixture has been characterized at GIF++ under several irradiation levels studying the main detectors parameters.

  The detectors longevity study is studied and preliminary results are reported, including the HF study.

- Chapter 7 **L1 Muon trigger study**:

  in this chapter is described the optimization study of the RPC information usage at the L1 muon trigger. The study was focused on the optimization of the RPC cluster size cut applied at the MTF level. All the relevant parameters and the performance that could be affected by the RPC cluster size cut have been studied and the results are reported.

2 Physics research at LHC

2.1 The Large Hadron Collider (LHC)

The Large Hadron Collider (LHC) [1–3] is a proton-proton/heavy-ion superconducting accelerator and collider built at CERN between 1998 and 2008. The purpose of LHC and its experiments is to study the physics phenomena at high energy scale, and test the predictions of the physics models based on theories, such as the Standard Model (SM) [4].

2.1.1 LHC parameters and performance

The energy available to generate new particles and process is one of the most important LHC parameter. The total energy at the collisions determines the center-of-mass energy ($\sqrt{s}$), which depends on the particles energies of the two beams, and on their momenta. The LHC nominal collisional energy in the center of mass is $\sqrt{s} = 7 + 7 = 14\ TeV$. Since only a fraction of the protons energy contributes to the hard scattering, the center-of-mass energy of the beam must be much higher than the mass of the particle that has to be produced. In fact, when two protons collide, two of its partons (quarks and gluons) can take part in a hard interaction with high transferred p_T. The effective centre-of-mass energy of the hard scattering ($\sqrt{\hat{s}}$) is smaller than the energy of the machine, and it is proportional to the fractional energies x_a and x_b carried by the two interacting partons:

$$\sqrt{\hat{s}} = \sqrt{x_a x_b s} \tag{2.1}$$

The interaction of two protons forms a primary vertex, from which the particles created in the interaction originate. Several independent proton-proton interactions can take place in a bunch crossing at the interaction point, this is known as pile-up. The number of interactions on average depends on the beam parameters, e.g. number of particles in a bunch and the focusing area size. The nominal average pile-up in LHC is ≈ 25.

The instantaneous luminosity is defined as the number of collisions per unit time and cross-sectional area of the beams:

$$\mathcal{L} = \frac{N_1 N_2 n_b f}{A} \tag{2.2}$$

where N_1 and N_2 are the number of particles in the two colliding bunches, A is the overlap area of the two bunches transverse to the beam, n_b is the number of bunches in one beam, and f is the revolution frequency of one bunch (with a design value of 11245 Hz). The nominal LHC instantaneous luminosity is $\mathcal{L} \approx 1 \times 10^{34} cm^{-2} s^{-1}$ [5].

The integrated luminosity ($\mathcal{L}_{int}$) is derived by integrating the instantaneous luminosity over a given period of time, as in Formula 2.3. The integral is taken over the sensitive time, i.e., excluding possible dead time of LHC. It is often expressed in inverse femtobarn fb^{-1} [1].

$$\mathcal{L}_{int} = \int_{t_0}^{t_1} \mathcal{L}\, dt \tag{2.3}$$

The integrated luminosity multiplied by the interaction cross-section (σ_p) for a process, gives the total number of events (N) produced during a time period. This parameter characterizes the efficiency of obtaining physical information from LHC.

$$N = \mathcal{L}_{int} \times \sigma_p \tag{2.4}$$

In the Table 2.1 the nominal LHC beam parameters are summarized.

On 20^{th} November 2009, LHC started its first proton-proton collisions. At this moment the LHC machine officially became the world's most powerful particle accelerator and entered in its Physics Run-I that lasted until February 2013. During Run-I

[1] The barn is a unit of area equal to $10^{-28} m^2$. Originally used in nuclear physics for expressing the cross sectional area of nuclei and nuclear reactions, today it is also used in all fields of high-energy physics to express the cross sections of any scattering process, and is best understood as a measure of the probability of interaction between particles.

Parameters	Units	LHC Design
Center of Mass Energy	TeV	14
Proton Energy per beam	TeV	7
Bunch Spacing	ns	25
Peak Luminosity	$\mathrm{cm}^{-2}\mathrm{s}^{-1}$	1×10^{34}
Number of Bunches	N/A	2808
Proton per Bunch	N/A	1.1×10^{11}
Pile-up	N/A	25

Table 2.1: Nominal LHC beam parameters

.

of the LHC program, the center-of-mass energy was $\sqrt{s} = 7\ TeV$, half of the nominal energy. Nevertheless, the energy and luminosity displayed during Run-I were enough for both CMS and ATLAS experiments to discover the Higgs boson [6–10]. After two years of Long Shutdown (LS1) for upgrades, the LHC started again in 2015 for Run-II with center-of-mass energy $\sqrt{s} = 13$ TeV, and on 3^{rd} December 2018 ended with a last heavy ion run [11]. During the operations, the instantaneous luminosity was successfully brought to a value of $\approx 2 \times 10^{34} cm^{-2} s^{-1}$, exceeding the design value. Run-II has been the occasion to acquire more data to study the properties of the Higgs boson with more precision. From the end of 2018 to early 2021 the LS2 will take place. This second maintenance stop will be the occasion to boost once again the beam energy to finally reach the design energy of LHC, 14 TeV.

The Run-III is scheduled to operate at $\sqrt{s} = 14$ TeV and at $\approx 2 \times 10^{34} cm^{-2} s^{-1}$ as instantaneous luminosity. During these 3 years of run, the LHC will deliver as much integrated luminosity as what brought during the almost 7 years of both Run-I and Run-II of data taking. Phase-I will end with an overall 300 fb^{-1} delivered.

2.1.2 High Luminosity-LHC (HL-LHC)

From 2026 the accelerator will enter in the Phase-II, or High Luminosity LHC (HL-LHC) configuration. The HL-LHC project was announced as the top priority of the European Strategy for Particle Physics in 2013, with the aims to crank up the performance of the LHC in order to increase the potential for discoveries. The objective is to increase the integrated luminosity by a factor of 10 beyond the LHCs design value. During the LS3 the accelerator infrastructure will be improved in order to achieve un-

precedented levels, five times more than designed instantaneous luminosity 5 to 7.5 $\times$ $10^{34} cm^{-2} s^{-1}$ resulting in total 3000 to 4000 fb^{-1} of integrated luminosity for the full accelerator lifetime. Many search channels are statistics limited, and their sensitivity increases in proportion to the integrated luminosity. For many proposed scenarios, including Supersymmetry and new heavy gauge bosons, the attainable mass range can be improved at HL-LHC by at least one TeV [12–14]. The properties of the discovered Higgs boson will be measured with higher precision, which will allow searches for new physics associated with the Higgs sector. Also the accuracy for many SM tests will improve considerably, in particular, the sensitivity to rare processes increases linearly with luminosity. The searches for new physics will be extended to exotic models, with challenging signatures from the experimental point of view: long-lived particles decaying leptonically, final states with low p_T muons, heavy slowly moving charged particles, or highly boosted dimuons, requiring improved muon detection and trigger capabilities.

Figure 2.1 report the LHC and HL-LHC plan, showing the evolution of the beam energy, the instantaneous and integrated luminosity.

Figure 2.1: Plan of LHC and HL-LHC operation, showing the evolution of the beam energy, the instantaneous and integrated luminosity.

2.1.3 LHC experiments

Along the accelerator ring there are four main interaction points (IP) where the two proton beams, travelling in separate vacuum pipes, are made collide. The LHC detectors are located in the interaction points to allow physicists to test the predictions of different theories of particle physics. The four main experiments are briefly described below.

- **A Large Ion Collider Experiment (ALICE)** [15]: a particle detector located at IP2, dedicated to the measurements of the nuclear matter properties at high energy densities. The focus of ALICE detector is the study of Quark Gluon Plasma (QGP) and different features of heavy-ion physics by means of lead-lead and proton-lead collisions [16].

- **Large Hadron Collider beauty (LHCb)** [17]: a single-sided spectrometer located at IP8, built to investigate matter-antimatter asymmetry, focused on the physics with hadrons originating from bottom quarks and the measure of CP violation parameters. The biggest discovery of LHCb collaboration at CERN has observed the matter-antimatter asymmetry, known as CP violation, in the decays of a D^0 meson for the first time [18].

- **A Toroidal LHC ApparatuS (ATLAS)** [19]: a general-purpose particle detector located at IP1, designed to cover wide range of precise measurements of the possible physics processes, such as electroweak and strong physics. The detectors were formulated especially to provide the best possible sensitivity to Higgs boson and new physics such as Supersymmetry (SUSY), dark matter, extra-dimensions, etc. The main feature of the ATLAS detector is its enormous doughnut-shaped magnet system. This consists of eight 25 m long superconducting magnet coils, arranged to form a cylinder around the beam pipe through the centre of the detector. ATLAS is the largest volume collider detector ever constructed.

- **Compact Muon Solenoid (CMS)** [20] a multi-purpose particle detector located at IP5, with the same physics research program as ATLAS, but different technical solutions and design. CMS is discussed in details in chapter 3.

3

The Compact Muon Solenoid (CMS) experiment and its upgrade for HL-LHC

The Compact Muon Solenoid (CMS) is a general-purpose detector at LHC having a broad physics programme ranging from studying the Standard Model (including the Higgs boson) to searching for physics beyond the SM [20]. Although it has the same scientific goals as the ATLAS experiment, it uses different technical solutions and a different magnet-system design.

3.1 Overview of the CMS detector

The CMS detector has a cylindrical barrel shape closed by two endcap disks, with a full length of $\approx 21\ m$, a diameter of $\approx 15\ m$, and a total weight of about 14000 tonnes. The CMS detector uses an onion like layout around the interaction point in order to maximize the acceptance. Each layer constitutes a subdetector designed to stop, track or measure a different type of particle emerging from LHC collisions. The innermost layer is a silicon-based tracker. Surrounding it is a scintillating crystal electromagnetic calorimeter, which is itself surrounded by a sampling calorimeter for hadrons. The tracker and the calorimeters are compact enough to fit inside the CMS solenoid. Outside the magnet are the large muon detectors, which are inside the return yoke of the magnet. The overall view of the CMS detector is shown in Figure 3.1.

A Cartesian coordinate system is chosen as the reference frame for the measurement of the physical quantities at the CMS detector. Its origin is the interaction point, the z-axis is collinear along the beam, the x-axis points radially toward the center of

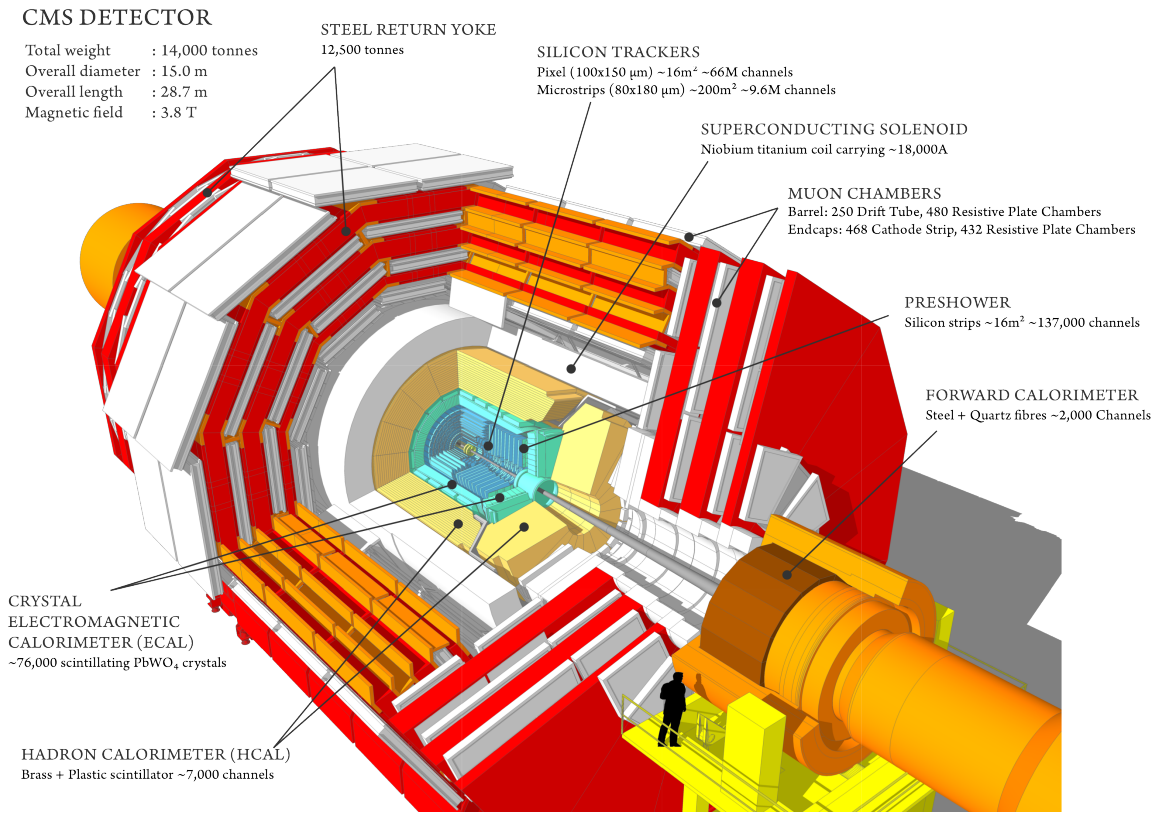

Figure 3.1: Overall view of CMS detector and its subdetectors.

the LHC ring, and the y-axis is perpendicular to the x-z plane and points upward. Reconstruction algorithms, however, use a spherical coordinate system based on the radial distance $R = \sqrt{x^2 + y^2}$ from the z-axis, the azimuthal angle ϕ with respect to the y-axis, and polar angle θ with respect to the beam line. However, taking into account that the particles produced by proton collisions are strongly pressed to the collision axis and distributed over the angle θ very unevenly, it is customary to use a different, more convenient, kinematic variable called pseudorapidity (η) [21]. The η value is determined by the Formula 3.1:

$$\eta = -ln(tan(\frac{\theta}{2})) \tag{3.1}$$

3.1.1 The solenoid magnet

A magnetic field is essential for identifying the particles emerging from collisions: it curves their trajectory allowing to calculate their momentum and to establish whether

they have a positive or negative charge. Stronger magnetic field allows to obtain higher momentum measurements resolution. The CMS superconducting solenoid magnet has an internal diameter of 6 m, length of 12.5 m, and it is designed to produce uniform field in the axial direction of 4 T, approximately 100000 times stronger than the earth's magnetic field [22]. The flux return is assured by an external iron yoke with three layers, capable of stopping almost all particles (except muons and neutrinos), in between which the muon system is installed.

3.1.2 The tracker system

The innermost sub-detector of CMS, surrounding the interaction point, is the silicon tracker [23, 24]. Its aim is the accurate, robust and efficient tracking of the charged particles produced by the collisions. Of fundamental importance is the precise measurement of secondary vertices with a resolution of 10 μm. At the LHC design, each bunch-crossing produces about one thousand particles crossing the tracker every 25 ns. This large number of tracks, coming from different primary vertices, needs a fast, high-granularity and radiation-resistant detector. The full volume of the tracker has a length of 5.8 m, a diameter of 2.5 m, and can provide tracking coverage up to $|\eta| < 2.5$. The tracker consists of two subsystems: the pixel tracker and the strip tracker. A general overview of the CMS tracker system is given in Figure 3.2, with its subsystems: Pixel, Tracker Inner Barrel (TIB) and Tracker Inner Disks (TID), Tracker Outer Barrel (TOB) and Tracker Endcaps (TEC).

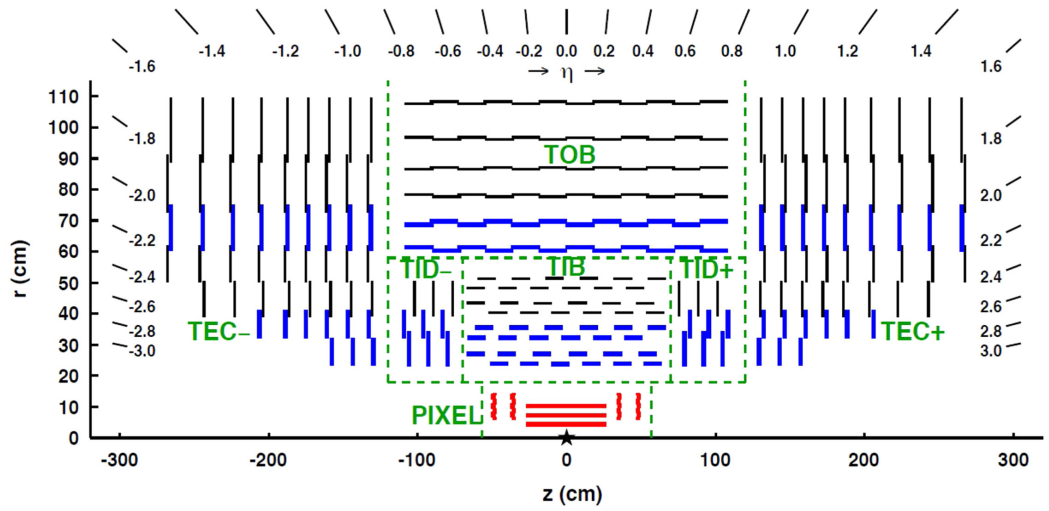

Figure 3.2: Overview of the CMS tracker system.

Pixel detector: the inner pixel detector is installed within a distance of 20 cm from the beam pipe. It provides high-resolution 3-D measurements for the charged track reconstruction. In overall, the pixel detector consists of three barrel layers (BPix) with two endcap disks (EPix) on each side of the barrel.

Strips detector: in addition to the pixel detectors, the inner tracker is composed of several layers of silicon microstrip detectors: four-layer Tracker Inner Barrel (TIB), six-layer tracker outer barrel (TOB) and on each side three-disk Tracker Inner Disks (TID) and nine-disk Tracker Endcaps (TEC). The full tracker consists of 15148 microstrip detectors, with a pitch size ranging from 80 to 180 μm.

3.1.3 The calorimeter system

Two types of calorimeters are installed in CMS: the internal electromagnetic calorimeter (ECAL) and the external hadron calorimeter (HCAL). Electrons, photons and hadrons are stopped by the calorimeters allowing their energy to be measured. Neutrinos, as well as all the non interacting particles, escape direct detection but their presence can be inferred as an apparent energy imbalance in a collision.

3.1.3.1 Electromagnetic Calorimeter

The CMS electromagnetic calorimeter covers the pseudorapidity range $|\eta| < 3$ [25]. It is an hermetic homogeneous calorimeter consisting of 75848 lead-tunstate ($PbWO_4$) scintillating crystals, designed to fully absorb the energy of electromagnetically interacting particles, mainly photons and electrons. One of the driving criteria in the design was the capability to detect the decay into two photons of the Higgs boson ($H \to \gamma\gamma$). The reason to choose $PbWO_4$ material is due to its radiation resistance, high density of 8.28 g/cm^3, small Moliére length of 0.89 cm and a short radiation length 2.2 cm which results in high granularity and high energy resolution of ECAL. The ionized atoms in the $PbWO_4$ crystal induce the blue scintillating light ($\lambda \approx 420$ nm), which is then measured in photodetectors. The total amount of scintillating light produced is proportional to the energy deposited in the crystals by the electrons and photons.

3.1.3.2 Hadron Calorimeter

The hadronic calorimeter plays an essential role in the identification of quarks, gluons, and neutrinos by measuring the energy and direction of the jets and of the missing transverse energy flow in events [26]. The reconstruction of jets and missing transverse energy (MET) is crucial for many analysis which involves neutrinos and neutralinos. The HCAL is a sampling calorimeter with brass as absorber, plastic scintillator tiles as active medium, and wavelength shifting fibers to transfer the light to the detector. The HCAL consists of about 70000 scintillating tiles and is divided into a barrel region (HB) up to $|\eta| < 1.3$, an endcap region (HE) up to $|\eta| < 3$ and a forward region (HF) further down the beam pipe at 11.2 m that increases the coverage up to $|\eta| < 5.2$. The limited space for stopping power in the barrel region is overcome with an additional calorimeter outside (HO) the solenoid up to $|\eta| < 1.3$ that uses the coil and a 19.5 cm layer of steel yoke as the absorber.

Muons and neutrinos produced in the interactions go unregistered in the HCAL except for a small muon MIP trace. The statistical fluctuations in the sampling and leakage degrade the performance of the HCAL in comparison to the ECAL.

3.1.4 The muon spectrometer

In order to provide an independent muon identification, robust trigger and accurate momentum and charge measurements, the muon spectrometer is placed outside the magnet and it consists of 4 stations of detectors integrated into the iron return yokes. The muon identification is guaranteed by the amount of material in front of the chambers and in the return yoke of the magnet which shields the spectrometer from charged particles other than muons. The robustness and redundancy of the spectrometer is guaranteed by the presence of three types of gaseous detector: Drift Tubes (DT) in the barrel region, Cathode Strip Chambers (CSC) in the endcap and Resistive Plate Chambers (RPC) in both barrel and endcap regions.

A schematic view of the CMS Muon spectrometer is reported in Figure 3.3. The barrel region is divided into five wheels (Wheel 0, Wheel $\pm$ 1, Wheel $\pm$ 2). The muon chambers are installed on the outer and inner sides of the yokes, in the pockets between layers, arranged in four stations at different radius. Each station consists of

12 chambers, one per sector, except for the fourth one where 14 chambers are present. The two endcaps are made of 3 iron disks and 4 stations, divided in 2 or 3 rings. The rings are formed by 18 or 36 trapezoidal chambers that overlap in ϕ giving geometrical coverage close to 100%.

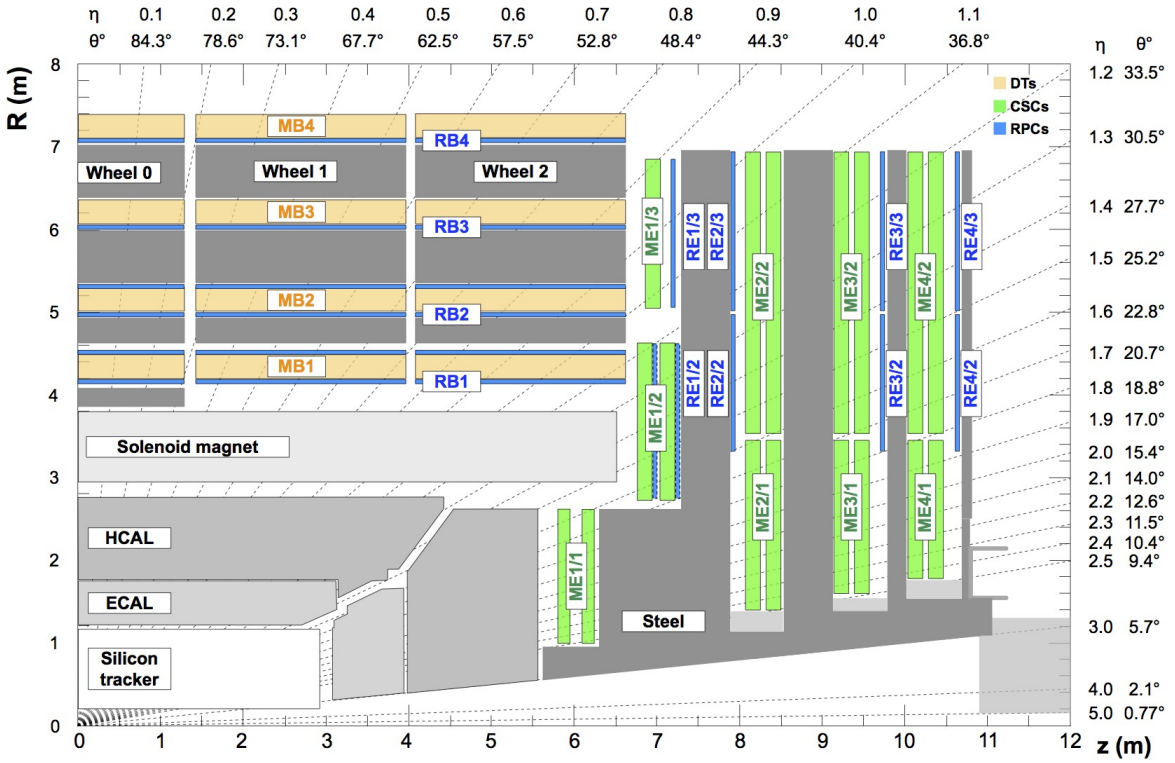

Figure 3.3: Schematic view of the CMS Muon spectrometer. The interaction point is at the lower left corner. The locations of the various muon stations are shown in color (MB = DT = Drift Tubes, ME = CSC = Cathode Strip Chambers, RB and RE = RPC = Resistive Plate Chambers). M denotes Muon, B stands for Barrel and E for Endcap. The magnet yoke is represented by the dark gray areas.

3.1.4.1 Drift Tubes

In the barrel the muon detector does not operate in particularly demanding conditions since the background rate in this region is low and the magnetic field is well contained in the iron plates of the magnet return yokes [21]. For this reason, the DT were chosen to cover the pseudorapidity region up to $|\eta| < 1.2$ [27]. The basic detector unit is a drift cell: a gas-filled tube with rectangular cross-section showed in Figure 3.4 (left). The two shorter sides of the rectangle form the cathodes, while an anode wire is strung through the middle. A charged particle passing through the detector volume ionizes the gas, producing a cloud of electrons that drift toward the wire. The

drift time is measured and converted to distance using the knowledge of drift velocity. A single drift cell has a cross-section of 42 × 13 mm^2 and wire length of 2-3 m. It is filled with a 85%/15% mixture of Ar/CO_2, giving a 350 ns maximum drift time. Single wire measurement resolution is of the order of 200 μm. The drift tubes in a chamber are grouped into SuperLayers (SL) consisting of four layers of tubes, staggered by half a tube. In each chamber there are two SLs with wires parallel to the beam direction, measuring muon position in the bending plane of the magnetic field. These are separated by a 128 mm thick aluminium honeycomb spacer, providing good angular resolution within one chamber. Additional SL measuring the η coordinate of the muon is present in the three inner stations. The SLs configuration is shown in Figure 3.4 (right).

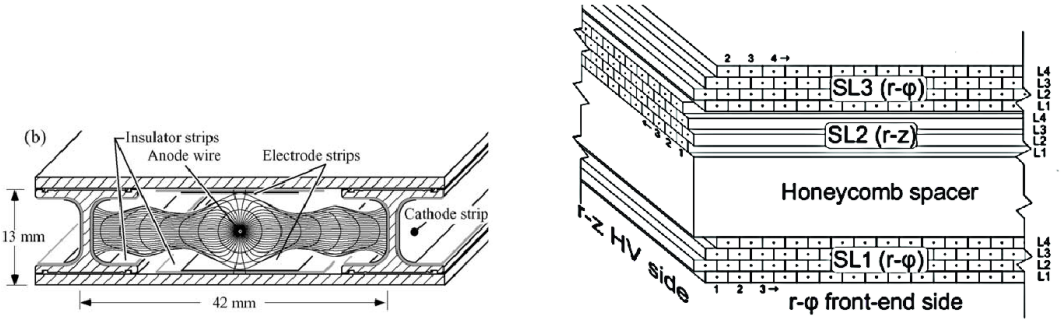

Figure 3.4: Illustration of the Drift Tube Chamber: drift cell unit (left), SuperLayers configuration (right).

3.1.4.2 Cathode Strip Chambers

The CSC cover the endcap muon region. This type of detector has been chosen because of its capability to provide precise time and position measurement in the presence of high and inhomogeneous magnetic field, and high particle rate [28].

The CSC detector is a multi-wire proportional chamber with one of the cathode planes being segmented in strips running orthogonally to the wires. The principle of operation is shown in Figure 3.5 (right): a muon crossing the chamber produces an avalanche in the gas (40%/50%/10% mixture of $Ar/CO_2/CF_4$) that is collected by the wire. This induces an electrical charge on several adjacent cathode strips. The measured distribution of charge picked up by the strips gives an estimate of the position of the muon along the wire.

The CSC geometry is reported in Figure 3.5 (left). Each individual chamber has a trapezoidal shape and is made of seven cathode panels stacked together, forming six gas-gaps, each containing an array of anode wires. The gaps are 9.5 mm thick and one of the two cathode planes for each gap is segmented into radial strips orthogonal to the wires. The strips cover a constant area in ϕ (2.33-4.65 $mrad$, depending on the disk). The orthogonal coordinate (R) is measured by the wires, which, to reduce the number of channels, are read out in groups of 5 to 16.

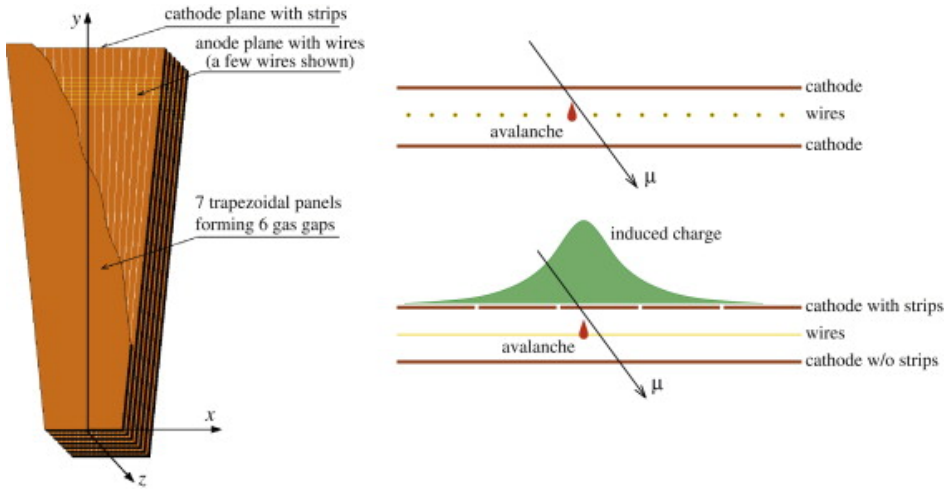

Figure 3.5: Cathode Strip Chambers geometry (left), and the principle of operation of a CSC, with cross-section across the wires (right-top) and across the strips (right-bottom).

3.1.4.3 Resistive Plate Chambers

The RPC are gaseous detectors developed early 1980s [29, 30]. Like other gaseous detectors, the RPC working principle is based on ionization process, that result in the production of electron-ion pairs within the gas volume. An external electric field is applied to accelerate the electrons, which trigger further ionizations in the gas, hence leading to the formation of an avalanche of electrons in the gaseous medium. The drift of the charge in the gas gap towards the anode induces on the pick-up strips the "fast charge signal", which represents the useful signal of the RPC.

The CMS RPC consists of two parallel High Pressure Laminate (HPL) plates, having 2 mm thickness and resistivity 1-6$\times 10^{10}$ Ωcm, separated by a 2 mm gas gap. A grid made of polycarbonate spacers ensures the rigidity and the thickness of the gap. The whole structure is made gas tight. The inner HPL surfaces are coated with linseed oil, while the outer surfaces are coated with 200 μm conductive graphite paint to

form the high voltage and ground electrodes. The read-out is performed via capacitive coupling of copper strips, separated from the graphite coating by an insulating PET film. The CMS RPC chambers are made of two gaps, to form the so called double-gap geometry, with common pick-up strips in the middle. A simplified layout of the double-gap design is shown in Figure 3.6 (left). In this configuration, the total induced signal is the sum of the two single-gap signals. This makes possible to operate single-gaps at lower gas gain (lower high voltage) with effective detector efficiency that is the OR of the single-gap efficiencies. The efficiency curves comparison between single gap and double gap configurations are reported in Figure 3.6 (right).

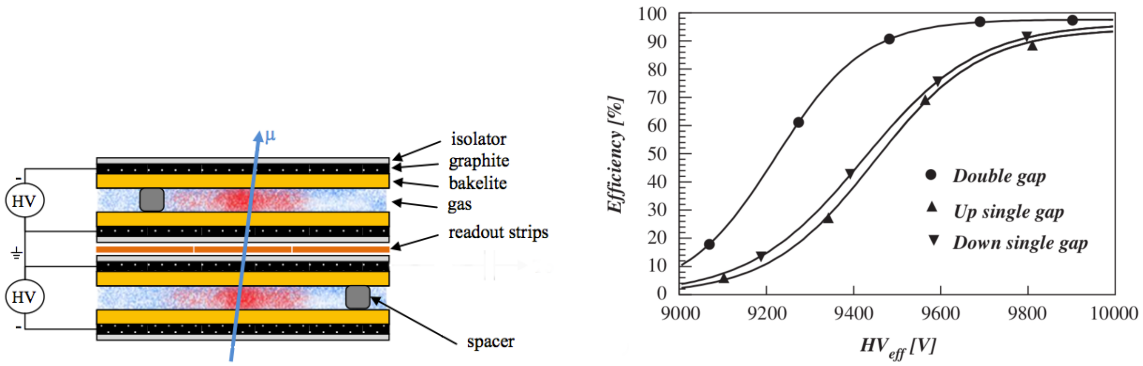

Figure 3.6: Left: Double gap RPC layout. Right: Comparison of efficiency curves of CMS RPC double and single-gap, measured with cosmic muons.

The CMS RPC operate with a humidified gas mixture composed by [21, 30, 31]: 95.2% $C_2H_2F_4$ (Freon-R134a), 4.5% iC_4H_{10} (isobutane) and 0.3% SF_6 (Sulphur Hexafluoride). The electrons drift velocity in $C_2H_2F_4$ promotes the excellent timing properties of RPCs. Polyatomic molecules, like iC_4H_{10}, are used as quencher since they limit the avalanche development by absorbing the UV photons. In fact, hard UV photons are produced during the avalanche multiplication process as a result of electron-atom collisions, in the ion-electron recombination in the gas or on the cathode surface. Quencher gas are able to absorb photons in a wide energy range since they have a large number of non-radiative excited states (rotational and vibrational). SF_6 is used in very little quantities for its high electro-negativity. Any excess of electrons is absorbed by the compound, and streamers are suppressed [32,33]. Nevertheless, a fraction of SF_6 higher than 1% would not bring any extra benefice in terms of streamer reduction power but would lead to higher operating voltage.

In the Table 3.1 the main CMS RPC parameters are summarized.

HPL thickness	2 mm
HPL resistivity	1-6 $\times 10^{20}$ Ωcm
Graphite resistivity	100 $k\Omega/\square$
# Gaps	2
Gas gap thickness	2 mm
Gas mixture	95.2% $C_2H_2F_4$, 4.5% iC_4H_{10}, 0.3% SF_6

Table 3.1: Main CMS RPC parameters

.

The CMS RPC detector parameters have been optimize to fulfil the CMS requirements and to guarantee 10 years of operation at the nominal LHC conditions [21,34,35]. The RPC performance are summarized in Table 3.2.

Rate capability	300 Hz/cm^2
Efficiency	$> 95\%$
Time resolution	1.5 ns
Intrinsic noise	< 5 Hz/cm^2
Cluster size	≈ 2 $strips$
Spatial resolution	10 mm

Table 3.2: Main CMS RPC parameters

.

The CMS RPC system consists of 1056 RPCs, organized in 4 stations covering a pseudorapidity range of $|\eta| < 1.2$ in the Barrel region, and 4 stations for each Endcap covering $0.9 < |\eta| < 1.9$ [21, 36]. It has more than 110000 electronic channels and covers a sensitive area of 3500 m^2.

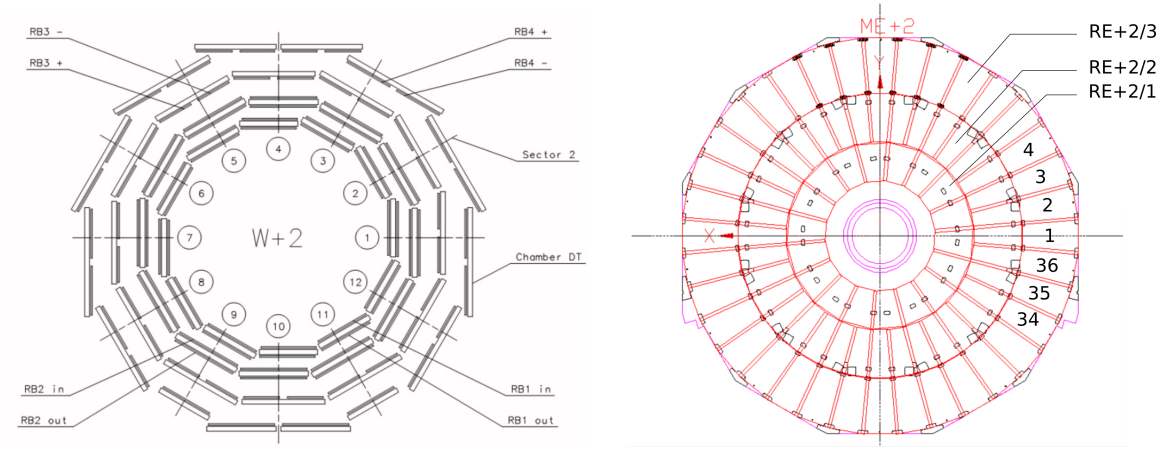

Figure 3.7: CMS RPC system layout in the Barrel (left) and in the endcap (right).

A total of 480 RPCs are installed in the barrel part of CMS muon system and divided equally among 5 wheels along the beam pipe, as represented in Figure 3.7 (left). Each wheel consists of 4 muon stations (RB1, RB2, RB3 and RB4) at increasing radius (R) and is divided in 12 sectors (S01-S12) in ϕ. The inner two stations consist of 2 layers of RPCs with a DT in the middle namely RB1in, RB1out, RB2in and RB2out, while the outer two station consist of a single layer in RB3 and RB4 and one layer of DTs. RPCs in RB3 and RB4 are divided in + and − along ϕ, for mechanical reasons, in all sectors apart from sectors S04, S09, S11 in RB4. RB4/S09 and RB4/S11 are in the feet of the barrel wheels and they consist of a single RPC chamber. RB4/S04 is divided in 4 chambers: ++, +, − and −−. For trigger requirements, RPC barrel chambers are divided along the beam axis into two $|\eta|$ partitions: forward and backward rolls,as shown in Figure 3.8 (left). Just two chambers are divided in 3 $|\eta|$ partitions (forward, middle and backward) i.e. RB2in in Wheels -1, 0, 1 and RB2out in Wheel -2, +2. The strip pitch of the barrel chambers is between 2.2 and 4.1 cm.

Endcap RPCs design is similar to the barrel RPCs except for the different shape and the fine segmentation which is essential for higher multiplicity forward regions [37]. A total of 576 RPCs are installed in the endcap and distributed along 8 disks (4 disks per each endcap, positive and negative) named RE±1, RE±2, RE±3 and RE±4 as given in Figure 3.7 (right). Run-I data have been taken with only 3 stations i.e. (RE±1-3), while the two disks for the fourth stations both positive and negative have been installed during the LS1 (2013-2014) [38]. Each disk is divided in 36 sectors along ϕ and has two concentric rings: ring 2 (R2) and ring 3 (R3). Each ring is made up of 36 trapezoidal chambers spanning 10° which are further split into three rolls, identified as A, B and C concerning increasing η. The strip pitch of the endcap chambers is between 1.8 and 3.8 cm. Due to the partitioning of the read-out strips into three rolls, the TOP layer gap is divided into two gaps: Top Narrow (TN) and Top Wide (TW), as shown in Figure 3.8 (right). The Bottom (BOT) layer instead consists in one gap.

Both endcap and barrel chambers are equipped with a Front End Board (FEB) which apply a threshold of 220 $mV \approx 150$ fC [39].

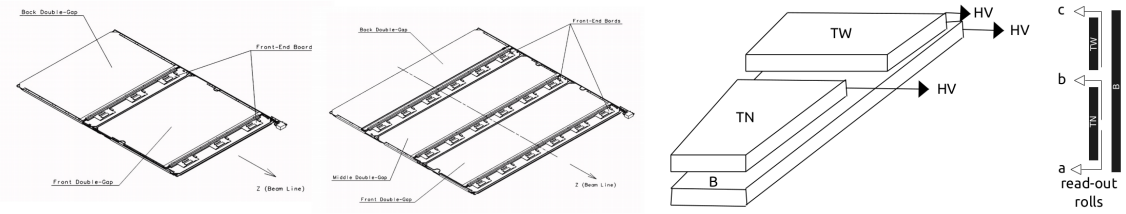

Figure 3.8: RPC geometry in barrel (left) and endcap (right). The barrel chambers are segmented in two or three rolls. In the endcpap chambers, the top gap layer is divided into two gaps: Top Narrow (TN) and Top Wide (TW), due to the partitioning of the read-out strips into three rolls. The bottom layer only consists in one gap (BOT).

3.1.5 The trigger

The data collected for each interaction, at nominal LHC condition, would require 40 TB of storage per second which is not feasible for CERN main computing farm, as its processing is limited by CPU performance and storage capacity. Most of the events, from soft interaction between the protons known as "minimum bias" events, are not interesting. The required reduction of the event rate, to save the interesting information, is achieved by the so-called trigger system [40]. The aim of the trigger is the selection of potentially interesting events and the reduction of the rate to a manageable value of a few hundred Hz. While most high energy physics experiments use three trigger levels, the CMS trigger system implements a two-stage, rate reduction which provides additional flexibility.

The first is the Level-1 (L1) trigger, largely based on Field Programmable Gate Arrays (FPGAs) and Application Specific Integrated Circuits (ASICs), that reduce the rate from 40 MHz to 100 kHz with the latency[1] of 3.2 μs [41, 42]. The L1 trigger uses the raw information from Calorimeters and Muon system, and it searches for key signatures of interesting events: leptons, photons, hadronic jets, and p_T^{miss}, known as trigger objects. The L1 trigger from muon and calorimeter are then combined in the L1 Global Trigger (GT) which decides whether to pass or reject the event. The data are temporarily stored in pipelines of processing elements while waiting for the decision. Figure 3.9 shows the schematics of L1 trigger system. The L1 muon trigger is described in more details in chapter 7.

The events which pass the L1-trigger requirements are selected and passed to the

[1]The latency is the time during which the raw data information must be stored awaiting for a Level-1 trigger decision

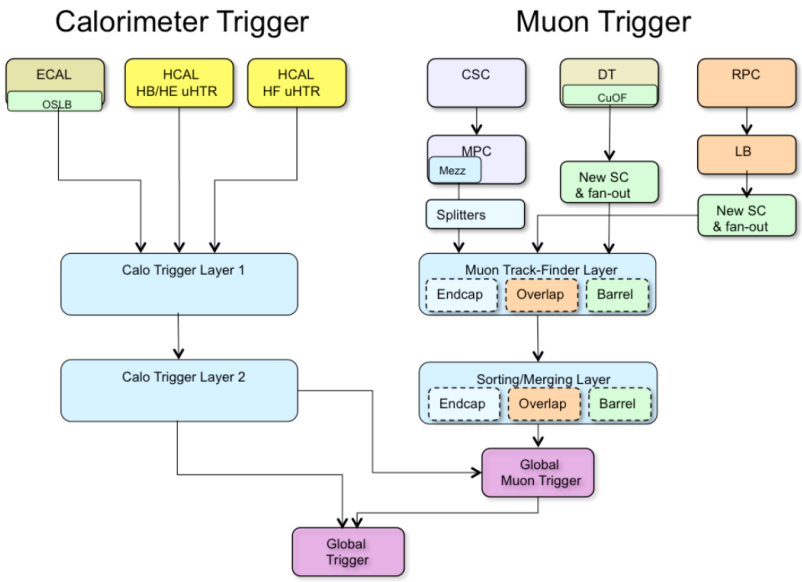

Figure 3.9: Architecture of the CMS Level 1 Trigger.

High-Level Trigger (HLT) [41, 43]. The HLT is a software-based system, implemented in computing facility with approximately 16000 CPU cores, that reduces the L1 trigger rate to a viable level for storage of about 100 Hz, with a processing delay time of about 100 ms. HLT can be used to reconstruct basic physics objects like jets, leptons and p_T^{miss} etc. To pass the HLT, an event needs to satisfy the requirements of at least one of its paths, which are in HLT menu. The events which passed the HLT are recorded permanently on the disk by the data acquisition (DAQ) system for further physics analysis and transferred to CERN Tier0 (T0) in one or more data streams.

3.2 The CMS upgrade project for HL-LHC

The increase in energy and in luminosity foreseen during HL-LHC has many implications on the CMS subdetectors, and it will be an hard challenge [44, 45]. The higher pileup, up to 140 to 200 interactions per bunch crossing, will leads to worse background conditions, higher trigger rates, more difficult event reconstruction, and accelerated aging of components.

To cope with the much higher collision rate, and to fully profit from it, the CMS experiment, including the muon detectors, need major upgrades. The basic goal of the CMS experiment upgrade is to maintain the excellent performance of the detector

subsystems in terms of efficiency, resolution, and optimize the reconstruction of the particles at higher luminosities. A brief description of the upgrade program for each subdetector is given in the following, with a detailed section for the muon system upgrade.

- **Tracker**: the CMS pixel will not be able to operate at the HL-LHC conditions. The pixel upgrade already started during the year technical stop of 2016/2017 with the replacement of the present pixel detector [38]. Nevertheless, because the entire tracker will suffer significant radiation damage, by LS3 the tracker must be completely replaced for Phase-II [46]. The granularity of both the outer tracker and the pixel systems will be increased by a factor four. Design improvements will lead to a much lighter outer tracker, improving, therefore, the p_T resolution and providing a lower rate of γ-conversions. Moreover, the module design will provide track-stub information to the L1 trigger at 40 MHz for tracks with $p_T >$ 2 GeV/c, ensuring meaningful power rejection at the earliest stage of the event selection. The pixel system will implement smaller pixels and thinner sensors for improved impact parameter resolution and better two-track separation. The system coverage will be extended to almost $|\eta| = 4$, thanks to the addition of up to 10 additional pixel disks in each of the forward regions.

- **Calorimeters**: for Phase-II the replacement of the electromagnetic and hadronic endcap calorimeters due to the possibility of the radiation damage has been planned by LS3 [47, 48]. The new calorimeter is called the High Granularity Calorimeter (HG-Cal). Its electromagnetic sensor consists of 28 tungsten plates interleaved with silicon sensors as the active material.

- **Trigger**: concerning the Level-1 trigger, the electronics for the calorimeter trigger, muon trigger, and the global trigger are planned to be improved [44, 45, 49]. For this aim, during the Phase-I the high bandwidth optical links for most of the data communication between trigger cards were installed, and modern, large FPGAs and large memory resources for the trigger logic were used. Using optical links allows changing the architecture very fast, while large FPGAs allow algorithms to evolve as needed. For Phase-II, the higher L1 accept rate is necessary to cope with the HL-LHC luminosity without raising the trigger thresholds [44].

The increase in latency from 3.6 to 12.5 μs is a direct consequence of the new Level-1 track trigger envisioned for the upgraded silicon tracker. Thus, the front-end electronics in some present sub-detectors must be upgraded.

3.2.1 The CMS Muon system upgrade

To maintain the excellent performance of the CMS muon system during HL-LHC will be a challenge, therefore several measures must be considered and undertaken [45].

- Background rate: the HL-LHC will produce well above 100 proton-proton interactions for every bunch crossing, taking place every 25 ns, yielding billions of secondary particles each second. The increase of the rate is a major challenge for the particle detectors, it had not been envisaged in the planning phase of the LHC in the 1990s. Thus, detectors and electronics have to be upgraded to handle the rate.

- Longevity: detector and electronics aging is strongly affected by the radiation. In general the performance of gaseous detectors deteriorates with an increase of the integrated charge released in the gas volume. All present gaseous detectors of the CMS muon system, and a large fraction of their electronics, are expected to stay also for HL-LHC, so their longevity must be validated.

- Redundancy and resolution: a major challenge at the HL-LHC is the reliable triggering on muons. Both the muon trigger and the offline muon identification and reconstruction can only work well if a sufficient number of detector hits is measured for each muon track. currently, the high η region is not fully equipped with all the muon chambers foreseen for Phase-I, and in addition the two endcap regions suffer from high muon and background rates and reduced magnetic bending. The number of hits measured per track must be increased to enhance the redundancy of the muon system and to obtain a robust track reconstruction. The Phase-II muon detector upgrade foreseen the installation of new forward muon detectors covering the pseudorapidity range up to 2.4. The first ring of the disks 1 and 2 will be equipped with Gas Electron Multiplier (GEM), GE1/1 and GE2/1. While, the first rings of the third and fourth disks will be equipped with improved

RPC (iRPC) detectors, RE3/1 and RE4/1. In addition to GE1/1 and GE2/1 station, the ME0 station will be also instrumented with GEM detectors, extending the acceptance of the muon system further to eta 2.8. The technologies of the new detectors have to handle the particle hit rates at maximum HL-LHC luminosity. The new detectors provide further high resolution measurement points and significantly increase the lever arm for track reconstruction. The schematic view of the upgraded CMS Muon spectrometer is reported in Figure 3.10.

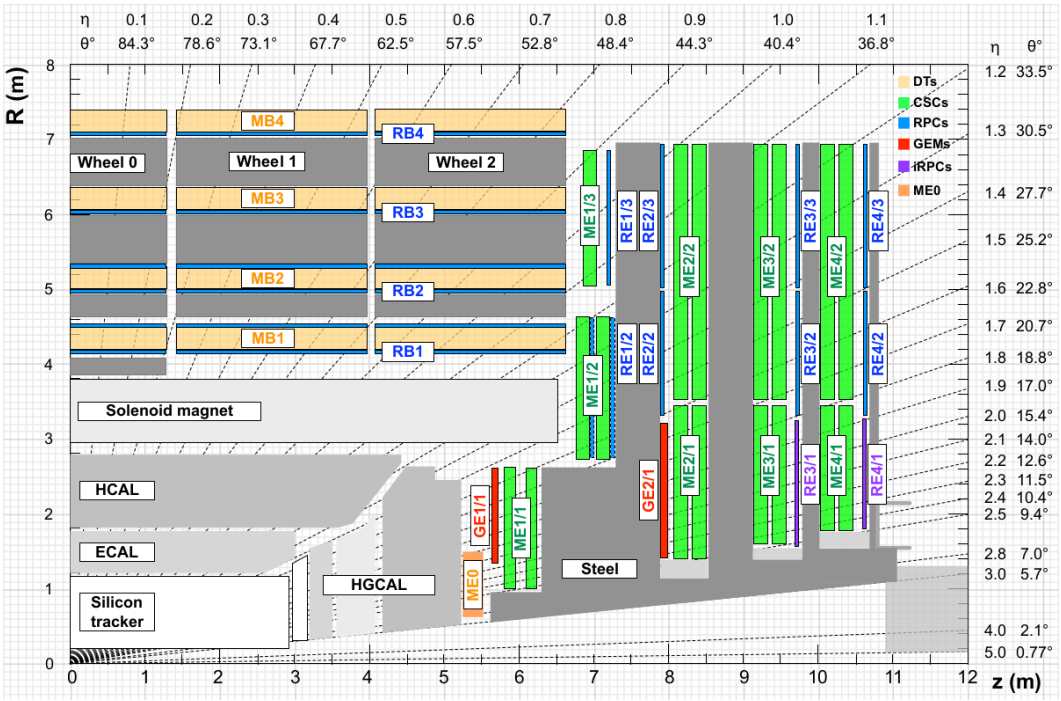

Figure 3.10: *R-z* cross section of a quadrant of the CMS detector, including the Phase-II upgrades (RE3/1, RE4/1, GE1/1, GE2/1, ME0).

- New ecogas mixture: recent European regulations demand the reduction of the greenhouse gases (GHG) emissions [50]. The EU regulation on fluorinated gases is aimed to limit the total amount of F-gases that can be sold in EU from 2015 onwards with a reduction to one-fifth from 2014 to 2030, banning the use of F-gases where less harmful alternatives are available. Despite GHGs would remain available for research applications, CERN is committed to follow the regulations, and so is the CMS Experiment. In order to comply with these constraints, the gas mixtures of some CMS muon subdetectors, such as CSC and RPC, must be adapted, or the release of greenhouse gases into the atmosphere must be substantially reduced.

The upgrade plans for each subdetector are briefly described below, and the following chapters will be dedicated to the RPC upgrade project.

Drift Tube upgrade: the expected hit rates in the DT chambers at the HL-LHC will be up to about 50 kHz per drift cell [45]. The highest rates are expected for the MB1 and for the MB4 chambers. The highest integrated charge in DTs per unit of wire length is estimated to be of the order of 20 mC/cm. Measurements performed on a spare detector show that the DT chambers can handle the hit rate expected during Phase-II. Longevity tests demonstrate that all MB2 and MB3 chambers, as well as the MB1 chambers of the three low-z wheels will maintain their current level of performance during Phase-II. Only in the MB1 stations in the outer wheels and in the MB4 detectors, a significant drop of the hit efficiency is predicted. The loss of efficiency is due to a decrease of the gas gain caused by deposits forming on the anode wires. The main culprit is believed to be outgassing of DT materials. Furthermore, possible mitigation measures of the aging effects are being actively studied. They include a decrease of the high voltage and the front-end electronic thresholds. For MB4 chambers, the background rates can be reduced by improving the neutron shielding of these detectors. The DT electronics will be replaced since the survival is not guaranteed, and it will not be able to cope with the increase of the Level 1 trigger acceptance rate beyond 500 kHz.

Cathode Strip Chambers upgrade: the charge corresponding to 10 years of HL-LHC running, is expected to be $\approx 0.2\ C/cm$ per unit of wire length for the CSCs closest to the beam line. Longevity tests of spare chambers demonstrate that any significant deterioration of chamber performance, such as gas gain, detection efficiency, spurious signal rates, strip-to-strip resistance, or dark currents has been observed after having integrated around twice the amount of charge expected. Thus, it is expected that the CSCs themselves can be used until the end of the HL-LHC operation. While the CSC modules are expected to provide satisfactory performance throughout the HL-LHC program, some CSC read-out electronic boards will need to be replaced in order to handle the more stringent trigger requirements. In general, the new boards will cope with higher L1 trigger rates and chamber occupancies by employing high-speed output optical links and faster processors. Similarly, the extended trigger latency requirement can be met with deeper (digital) buffers [45].

Gas Electron Multiplier: GEMs are gas detectors, characterized by a spacial resolution of order $\approx 100\ \mu m$, and time resolution of order $\approx 8\ ns$ at the efficiency plateau for Ar/CO_2 (70/30) as gas mixture [45]. By combining three foils to a triple-GEM chamber, the gas gain reaches a value of the order of 10^4. The gas gain is observed to be stable up to 150 kHz/cm^2, which is the maximum rate expected during HL-LHC. The GE1/1 and GE2/1 detectors are "super-chambers", each made of a double layer of trapezoidal triple-GEM detector. They will cover 10° in GE1/1 station and 20° in GE2/1 station, overlapping in ϕ just like the corresponding CSC detectors. Therefore, 36 super-chambers will be installed for the GE1/1 station and 18 for the GE2/1 station, in each muon endcap in order to ensure the full azimuthal coverage. The ME0 detector station comprises 36 module stacks (18 per endcap), each composed of six layers of triple-GEM detectors, compared to the two-layer design of GE1/1 and GE2/1, covering the region $2 < |\eta| < 2.8$, in order to allow proper rejection of neutron background, particularly intense in that region. The large η coverage foreseen would lead to an improvement of the acceptance, with a consequent boost in the signal over noise ratio in the signature with muons, especially with the multiple-muon final states, and better hermeticity for signature without muons.

4 Aging studies on CMS RPC

In the following chapter the longevity study for the RPC system during LHC period is reported. The results of the new longevity test ongoing at GIF++ to certify the RPC system for HL-LHC period will be described.

4.1 Aging studies of the CMS RPC system during LHC

The CMS RPC detector performance has been certified for 10 LHC years by extensive long-term irradiation test that were carried out irradiating full size and small RPCs prototype at several gamma and neutron facilities, up to an integrated charge of $\approx$ 50 and 400 mC/cm^2, respectively [51–53]. The detector performance and parameters have been measured and monitored during almost 7 years of operation and they are reported below.

4.1.1 Background radiation study

The background radiation plays a decisive role with respect to the detectors performance and aging. For these reasons, the background radiation in the CMS RPC system has been studied in detail [54].

The CMS RPC rate distributions as a function of pseudorapidity, measured during 2018 data taking, are shown in Figure 4.1. The rate are calculated at the instantaneous luminosity of $1.5 \times 10^{34}\ cm^{-2}s^{-1}$ and have been compared with the Monte Carlo

(MC) prediction. The results are reported per station, the top plots show the first (left) and second (right) barrel (RB1 and RB2) and endcap (RE1 and RE2) stations, while the bottom plots describe third and fourth barrel (RB3 and RB4) and endcap (RE3 and RE4) stations. For the barrel layers, the rate are averaged over ϕ for all the chambers installed at same radii, while in the endcap part the average values are taken for the chambers installed at same Z. The comparison between the MC and the experimentally measured values shows a good agreement in the barrel and small difference in the endcap of factor of 2. Nevertheless the distributions show coherent trends.

The background is not uniformly distributed, as it may be seen from the plots the background increases with absolute value of η, with the only exception in the first stations. The leak from the gap in the HCAL affects mainly the chambers from the first barrel station of the outermost wheels and less the chambers form the first endcap stations. The background affects mainly the top sectors and it is lower for the sectors near to the bottom of the cavern. The reason is the neutron gas in the cavern and the background leaks from the gaps of the rotating shielding. This particles rate distribution is because the main background rate sources are the particles coming from primary collisions and from their secondary interactions, and the neutron induced background in the cavern. Detector layers installed closer to the beam pipe and hence to the primary interactions are affected mainly by the prompt radiation component, while the outermost stations are affected mainly by the cavern background.

The dependence of the RPC hit rate with respect to the instantaneous luminosity was measured during different periods, and a linear correlation was found. The averaged hit rate values per barrel and endcap stations, measured in 2018 proton-proton collisions are shown on Figure 4.2. Stable runs with a number of colliding bunches larger than 600 and comparable run durations have been selected for the study. As it might be seen from the plot, highest rate are measured for the first barrel station (RB1), caused by the prompt particles, and for the outermost stations both in the central and endcap parts (RB4, RE+4, RE-4), where the forth endcap stations are the mostly affected ones.

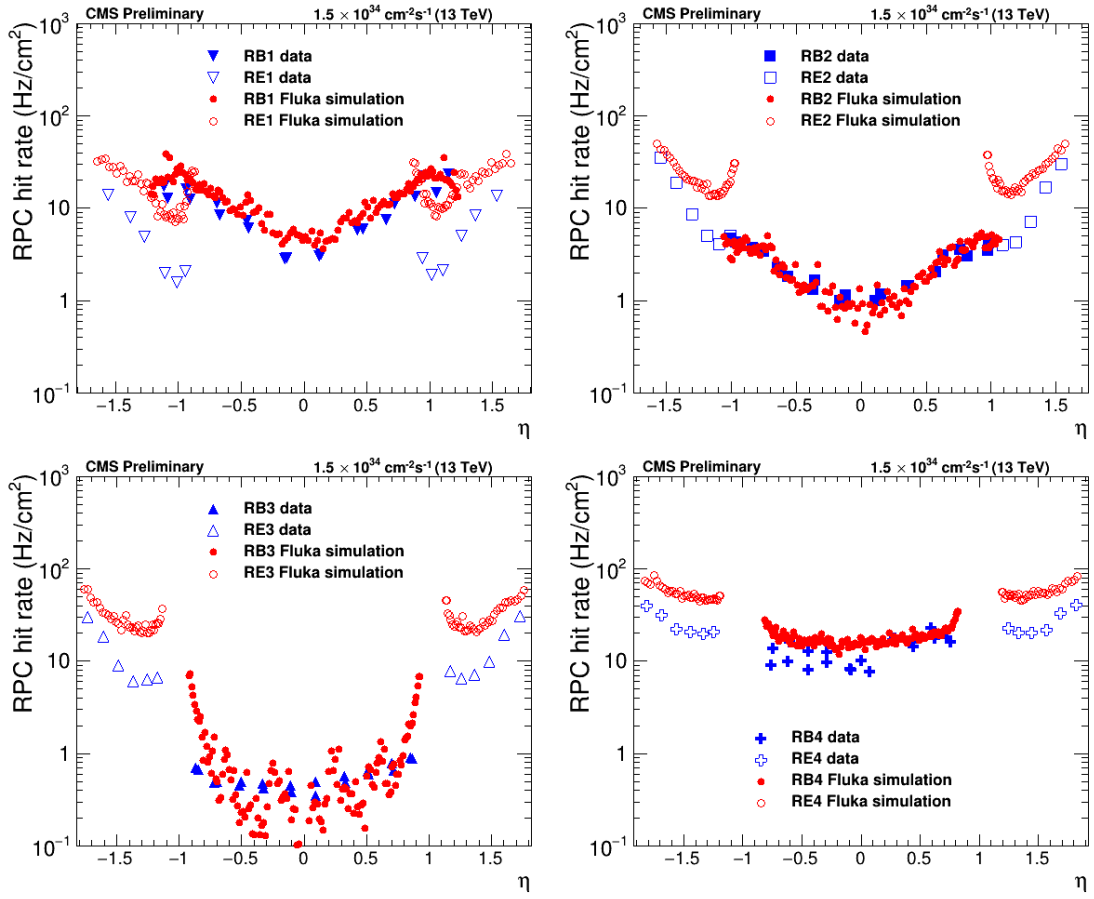

Figure 4.1: RPC hit rate as a function of pseudorapidity for the different RPC stations is shown (blue) with the results of FLUKA simulation superimposed (red). The full markers correspond to the barrel layers, while the empy ones to the endcap. The top plots show the first (left) and second (right) barrel (RB1 and RB2) and endcap (RE1 and RE2) stations, while the bottom plots describe third and forth barrel (RB3 and RB4) and endcap (RE3 and RE4) stations. Hit rate estimated values were evaluated at $1.5 \times 10^{34}\ cm^{-2}s^{-1}$ instantaneous luminosity and an average over ϕ was taken for each layer shown.

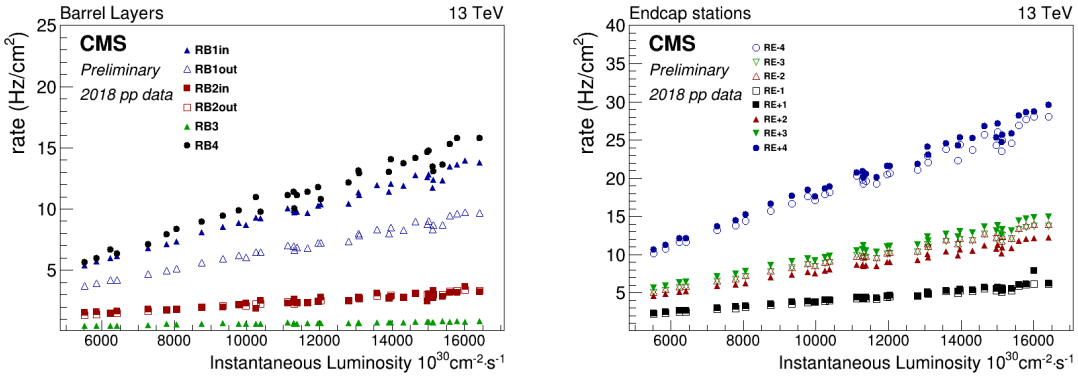

Figure 4.2: RPC average hit rate as a function of instantaneous luminosity for the Barrel (left) and Endcap (right) stations (right). The results have been obtained using 2018 proton-proton collision data, selecting runs with stable beam. The luminosity values are provided by the official CMS luminosity tool.

4.1.2 Performance study

During the first seven years of operation, the CMS RPC performance has been studied and monitored. Figure 4.3 shows the comparison between the overall efficiency measured during the 4 years of Run II data taking in the Barrel (left) and Endcap (right). The average efficiency is stable and greater than 95%, following the CMS requirements [54, 55].

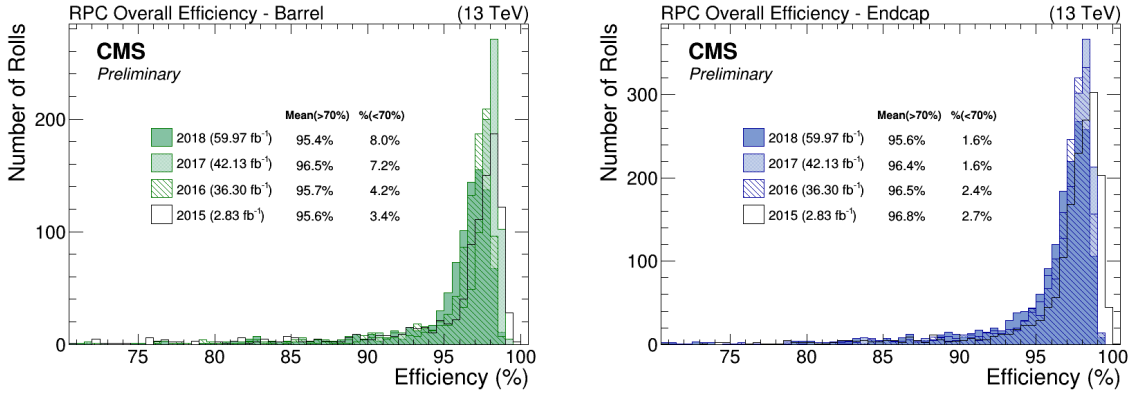

Figure 4.3: Overall efficiency distribution during the 4 years of Run II data taking, measured in the Barrel (left) and in the Endcap (right).

The RPC hit efficiency and the muon cluster size histories during Run II period are reported in Figure 4.4, for Barrel and Endcap. The results were obtained using the tag-and-probe method, where the charged particles tracks reconstructed in the inner silicon tracker are extrapolated to the RPC system [56]. Each point corresponds to the average efficiency per station in a given LHC fill. The RPC system performance remain stable and depends mainly on the hardware calibration and changes in the working gas mixture composition. In 2016, because of higher isobutane concentration (5.3%), efficiency was lower as the HV working points (WP) were not changed to compensate the wrong gas mixture. After the deployment of the new WP in September 2016, the efficiency increased slightly by 1% and cluster size increased sharply. Gas concentration was back at 4.5% in 2017 but the working point were not changed. The efficiency remained unchanged (running in the plateau of the sigmoid curve), however a new increase of the cluster size have been observed. New working point have been deployed by end of 2017, which led to a slight decrease of the efficiency but sensible reduction of the cluster size. The drop in the short period of 2018 data taking was caused by wrong working points setting.

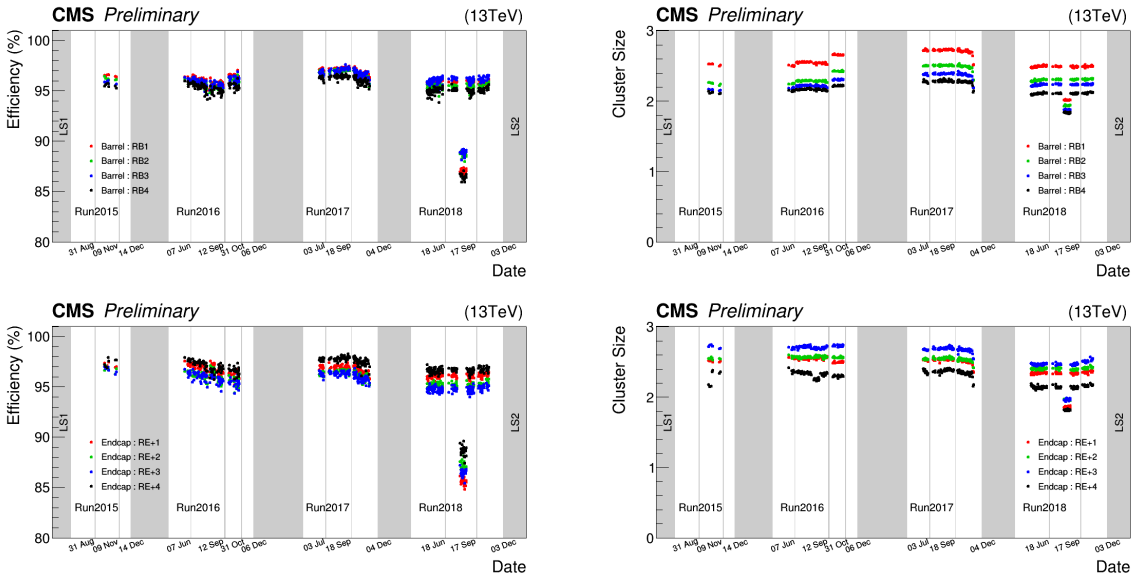

Figure 4.4: CMS RPC efficiency (left) and muon cluster size (right) monitored during Run II as a function of time. The plots on top represent the barrel stations, while the plots on bottom the stations in the positive endcap. Results for the negative disks are similar.

4.1.3 Current study

During 2018, when the LHC instantaneous luminosity increased reaching almost twice the nominal value, a general ohmic currents increase was observed [5]. The ohmic current is defined as the linear contribution at low applied voltages, at which the electric field across the gas is low and the multiplication processes in the gas are negligible. Under these conditions, the gas resistance is quite high, and the current measured across the two electrodes derives from the current flowing through the resistive plates and then through the spacers, the seal around the chamber, and/or, in general, any point of contact between the resistive anode and cathode. The ohmic current shows an approximately linear ohmic behaviour. Figure 4.5 shows the average ohmic currents measured in four representative RPC stations: W0 in the barrel and RE+1, RE+4, RE-4 in the endcap. The ohmic currents measurements were performed at 6.5 kV, during the periods with no collisions. The ohmic currents increase is more evident in the external detector stations, such as RE+4 and RE-4, while they are almost stable with a minimal increase in the inner detector stations, such as W0 and RE+1.

The background rate distribution in Figure 4.1 demonstrate the evident correlation with the ohmic currents increase. Indeed, the background rate in the external stations RE+4 and RE-4 is around 40 Hz/cm^2, while in the inner stations W0 and

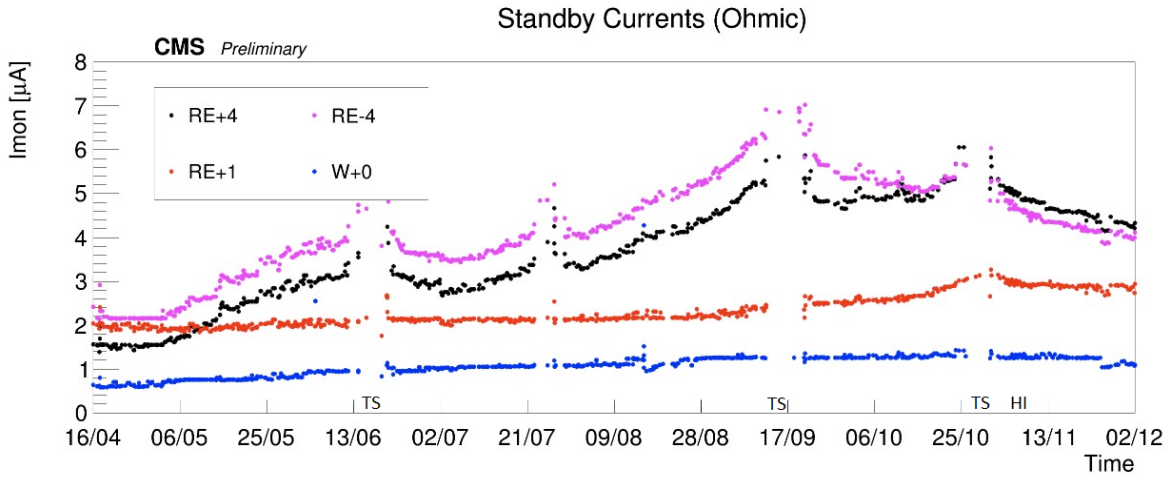

Figure 4.5: Ohmic currents measured as a function of time. The currents were measured during 2018 in four RPC stations: W0 in the barrel and RE+1, RE+4, RE-4 in the endcap.

RE+1 is less than 10 Hz/cm^2. Therefore, the ohmic current increase is directly proportional to the radiation: the higher the background rate, the higher the ohmic currents increase.

The ohmic currents were observed to decrease during the periods with no collisions, such as the technical stops (TS), or during the periods with very low instantaneous luminosity, such as the Heavy Ions (HI) collision periods. The ohmic currents, measured for around one month during the Heavy Ion period (November 2018), show a clear decreasing trend, which seems to follow an exponential decay, as reported in Figure 4.6. The current decrease is very evident in the high background stations RE+4 and RE-4, where indeed the increase was much more evident. While the current decrease is less evident in the low background regions W0 and RE+1, where the increase was less pronounced. The observed ohmic currents increase seems therefore to be not a permanent effect, but rather a partially recoverable effect.

Another parameter which plays an important role for the ohmic current stability is the gas flow. The exchange of the gas volume allows removing the pollutants created by the radiation in the detector gas gap, preventing the deposition on the inner surface and thus ensuring its integrity (more details in the section 4.2). The RE-4 and RE+4 stations operate in similar conditions: both are exposed to ≈ 40 Hz/cm^2 as background rate, and both operate with one gas volume exchanges per hour. Thus, the ohmic currents follow a similar trend. After the TS2, around the middle of September 2018,

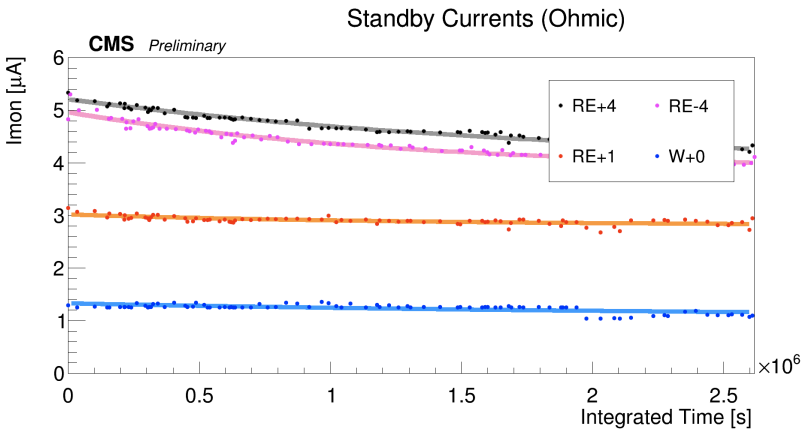

Figure 4.6: Ohmic currents as a function of time, measured at 6.5 kV in four RPC stations: W0 in the barrel and RE+1, RE+4, RE-4 in the endcap. The ohmic currents were measured during the Heavy Ion period at the end of 2018.

the gas flow has been doubled in RE-4 station, from one to two gas volume exchanges per hour, and a significant change in its ohmic current behaviour has been observed. The increase of the gas flow allowed to mitigate the ohmic currents increase, which is instead visible in the RE+4 station. The higher gas flow in RE-4 also allowed a faster ohmic current recovery during the heavy ion collisions period, up to the point that it drops below the RE+4 curve.

Figure 4.7 shows a roughly linear dependence of the ohmic current as a function of the integrated luminosity. The slopes of W0 and RE+1 stations are similar since the operating conditions, in terms of background rate and gas flow, are similar. The same is true for RE+4 and RE-4 stations. It is also possible to spot the change in the slope of the RE-4 station caused by the gas flow increase ($\approx 55\ fb^{-1}$). The linear dependence can be parameterized as:

$$i_{ohmic} = i_0 + k_i \times \mathcal{L}_{int} \tag{4.1}$$

$$k_i = \frac{\partial i_{ohmic}}{\partial \mathcal{L}_{int}} \tag{4.2}$$

Where i_{ohmic} is the ohmic current, i_0 is the offset and represents the intrinsic ohmic current of the detector, $\mathcal{L}_{int}$ is the integrated luminosity, and k_i is the slope representing the ohmic current variation with respect to the integrated luminosity

variation. The ohmic current variation depends on the instantaneous luminosity, and consequently on the background rate.

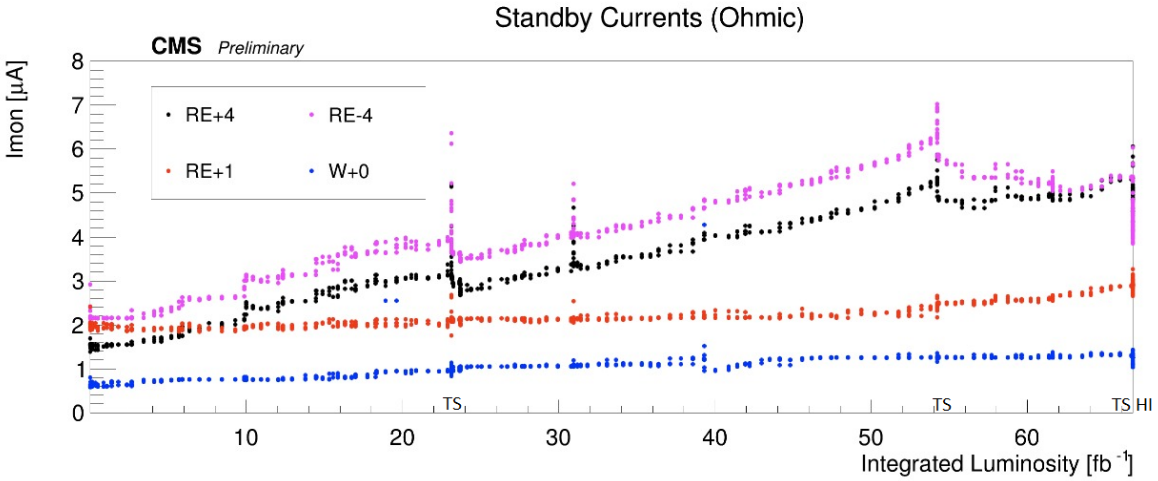

Figure 4.7: Ohmic currents measured at 6.5 kV as a function of the integrated luminosity. The currents were measured during 2018 in four RPC stations: W0 in the barrel and RE+1, RE+4, RE-4 in the endcap.

In conclusion, the background rate and the gas flow are the two main parameters that influence the stability of the ohmic current.

4.2 Hydrogen Fluoride (HF) study

The presence of pollutants in the gas gap may induce detector aging by damaging the HPL surface, and therefore affecting the performance. Many experiments that have used RPC detectors report a contamination of Hydrogen Fluoride (HF) acid in the exhaust gas [57–63]. However, the actual HF production mechanism is still not completely clear.

The RPC gas mixture is based on HydroFluorocarbon (HFC) components, and the decomposition of the $C_2H_2F_4$ molecules, induced by the relatively high-energy photons (i.e. UV) generated during the charge multiplication, produces a significant concentration of fluorine ions (F^-). The role of UV photons in the HF production is confirmed by the larger (a factor of 40 higher) fluoride concentration observed is some studies on RPC working in streamer mode [59]. Once fluorine radical is formed, it can react with H^+ ions, that comes from any Hydrogen sources present inside the gas mixture, such as water vapour or isobutane. The chemical reaction is reported in

Formula 4.3:

$$F^- + H^+ = HF \tag{4.3}$$

If the HF is not efficiently removed by the gas flow and it remains for a not negligible time inside the gas gap, it may represents a possible cause of the detector inner surface damaging due to its high chemical reactivity [60]. The HF can harm the HPL surface by damaging the polymerized oil layer, and the effect tends to increase with time since local damage produces a local higher F^- production. Furthermore, HF may form a thin conductive layer on the inner gap surface, decreasing the surface resistivity.

The effects induced by the HF, may lead to an increase of the dark current and the noise counting rate, which could affect the detector performance. For these reasons, the HF production has been studied both at GIF++ and in CMS, with particular regards to find a correlation with the ohmic current increase observed in CMS [64].

4.2.1 HF study at GIF++

The HF production mechanism has been studied to better understand and estimate the influence of the background rate and the gas flow. The HF measurements have been performed at the CERN Gamma Irradiation Facility (GIF++), a facility equipped with a 14 TBq Cs-137 gamma source where is possible to test real size detectors [65]. Additionally, a system of movable filters allows to test the detectors at different background conditions (ABsorption Factor ABS). The spectra of the gamma source depends on the filters configuration, and it is composed by primary 662 keV photons and lower energetic scattered photons. GIF++ provides a fairly realistic simulation of the LHC/HL-LHC conditions, since the main source of background hits in the muon detectors are neutron-induced photons with energies in the range 0.1-10 MeV.

The HF measurement technique is based on specific ion-selective electrode (ISE) [57,58,61,63]. The ISE is a transducer (or sensor) that converts the activity of a specific ion dissolved in a solution into an electrical potential. In general, ISEs are electrochemical semi-cells consisting of an ion-selective membrane (i.e a selective interphase for the ion in question), one solution and one reference electrode.

To measure the HF concentration, the RPC exhaust gas is bubbled inside a TISAB (Total Ionic Strength Adjustment Buffer) and distilled water solution, where

the fluorine is detectable by the ISE as F^- free ion. This is possible because the hydrolysis reaction occurs when HF is in touch with distilled water:

$$HF + H_2O \rightarrow H^+ + F^- \tag{4.4}$$

The TISAB neutralizes the effect of electrode interfering substances or metal traces that could bias the measurement, and it acts as a buffer keeping the solution at constant pH 5.5.

When the ISE sensing element is in contact with a solution containing fluoride ions, an electrode potential develops. The potential is measured with respect to a constant reference potential provided by the reference electrode. The measured potential corresponds to the level of the fluoride ions in solution and it is described by the Nernst equation [66]:

$$E = E_0 + SLog(A) \tag{4.5}$$

where E is the electrode potential, E_0 is the reference constant potential, S is the electrode slope and A is the fluoride ion activity level in solution. The level of fluoride ions, A, is the activity or effective concentration of free fluoride ions in solution. The fluoride ions activity is related to the concentration C_f by the activity coefficient, γ:

$$A = \gamma C_f \tag{4.6}$$

The conversion from the measured potential to the concentration is done using the electrodes calibration curve. The concentrations are then normalized with respect to the solution volume.

The set-up used at GIF++ is represented in Figure 4.8. The exhaust gas of an irradiated spare endcap chamber flows in the solution, where the ion-selective electrode[1] allows the F^- measurements. All the main parameters (environmental parameters, gamma background rate, detector HV, current and gas flows) were continuously monitored and controlled by the DCS and DAQ system. The measurements have been performed operating the detector at working point ($\approx 9.8\ kV$), and the gas flow fraction analysed was 0.5 l/h.

[1]For the measurements HANNA Instruments electrodes have been used.

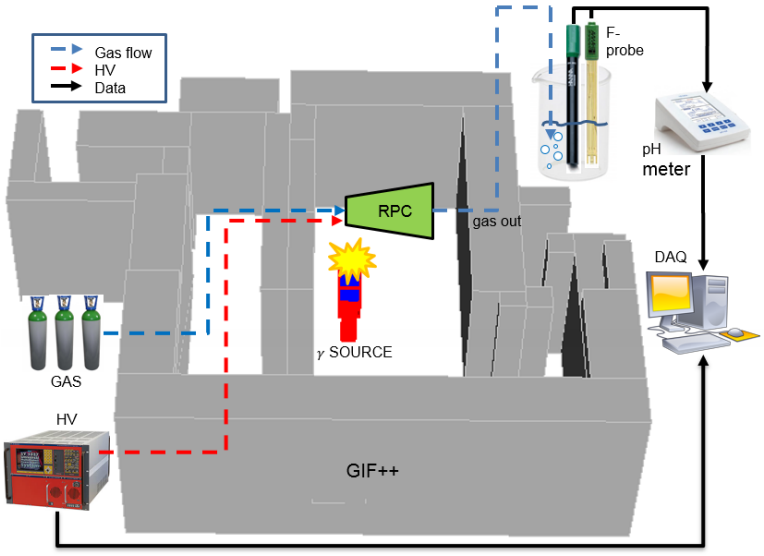

Figure 4.8: GIF++ experimental set-up for the HF measurements.

For the entire measurements, the ISE was immersed in the solution and the electrical potential measured was read and recorded through the DAQ system with a frequency of 2 Hz. After the ISE stabilization time, for 3 times the detector alternated 2 hours of HV on and then 2 hours of HV off. This measurements schema aims to study the HF production trend at the different detector stages. At the end of the measurements, when the detector was turned off, the HF concentration was measured for 8 more hours to very the possible presence of HF not quickly and efficiently removed, and therefore trapped inside the gap.

A view of the measurement is reported in Figure 4.9, that shows the typical measured HF curves. The plot on the left represents the HF accumulated operating the detector with fixed gas flow (1 gas volume exchange per hour) at different ABS.

For each background rate conditions, the measurements have been performed operating the detector with three different gas flows: 0.2, 1 and 3 gas volume exchanges per hour. An example is reported on the right plot, which shows the HF accumulated at fixed background rate ABS 46, measured with the three different gas flows.

The HF concentration linearly increases when the detector operates at stable conditions (background rate and gas flow), while it is stable when the detector is off.

The fit of the linear trend of each HF curve, normalized in time and volume, allows obtaining the HF production rate at different background rate with different gas flows.

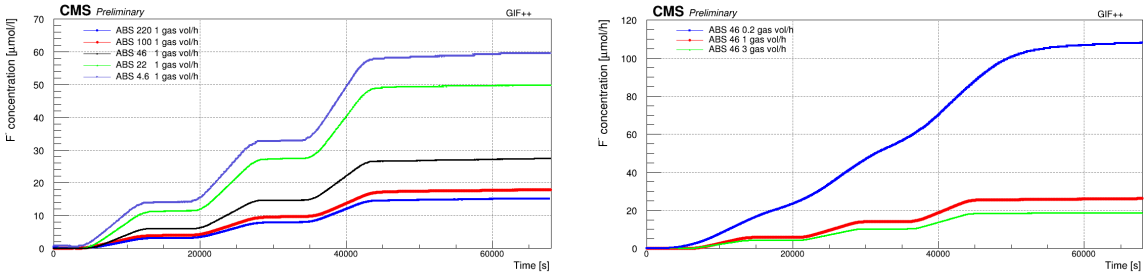

Figure 4.9: Left: F^- concentration as a function of time, at different background rate (ABS), operating with one gas volume exchange per hour. Right: F^- concentration as a function of time, operating with three different gas flow, at fixed background rate (ABS).

The results are reported in Figure 4.10 (left). The plot shows a linear dependence of the HF production rate on the background rate (and current). The HF concentration linearly increases with the background rate. The HF slope depends instead on the gas flow, higher is the gas flow and less is the HF concentration.

To quantify the gas flow effect, the ratio of the slope for each gas flow to the slope at a gas flow of 1 volume exchange per hour is shown in Figure 4.10 (right).

These results demonstrate the HF dependence on the background rate and on the gas flow.

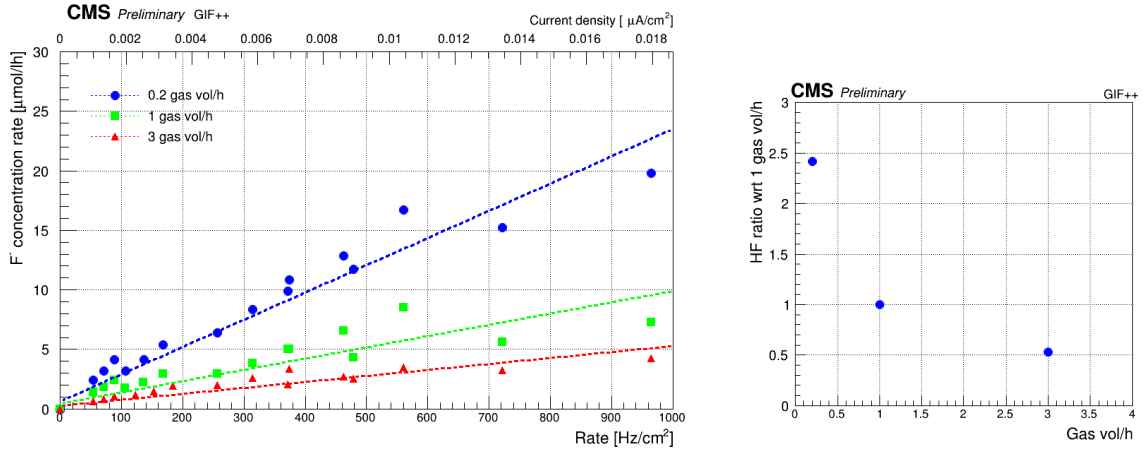

Figure 4.10: Left: F^- concentration rate as a function of the background rate (and its corresponding current on the top X-axis), measured with three different gas flow: 0.2, 1 and 3 gas volume exchanges per hour. Right: Ratio of the F^- concentration measured at different gas volume exchanges with respect to 1 gas volume exchange per hour.

Finally, Figure 4.11 shows the concentration of HF not efficiently removed by the gas flow and thus trapped inside the gas gap. The estimation was done considering the HF accumulated during the last 8 hours of measurements, just after the detector

switch off (see Figure 4.9). The results show that the concentration of the HF trapped inside the gas gap increases at high background rate, when the HF production is high. Above all, the concentration of the HF trapped depends on the gas flow: higher is the gas flow and less is the HF trapped.

The gas flow effect was also evident in Figure 4.9, which shows that the HF is efficiently removed with high gas volume exchanges, indeed when the detector is turned off the HF curves reach almost immediately the plateau and no more HF is accumulated. On the contrary, a significant fraction of HF remains trapped inside the gas gap with low gas volume exchanges, indeed when the detector is switched off the HF accumulated continues to increase for a not negligible time before reaching the plateau.

The probability that HF deposits on top of the inner gap surface, with consequent damage, obviously increase with the HF concentration and with the increase of time that remains inside the gas gap.

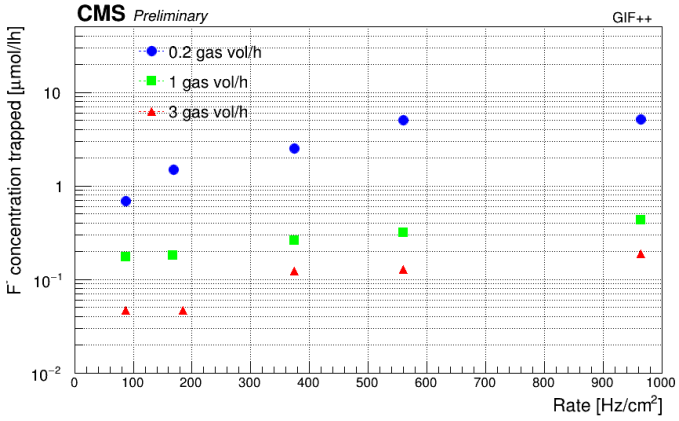

Figure 4.11: F^- concentration trapped inside the gas gap and not efficiently removed. The concentration was measured at different background rate, and with three different gas flow. The estimation was done considering the F^- accumulated during the last 8 hours of measurements, just after the detector switching off.

The HF measured at the exhaust gas represents the quantity extracted, more or less efficiently, from the gas gap by the gas flow. If the HF is a cause of detector aging then a fraction of the HF produced must be absorbed by the inner gap surfaces.

To check the HF absorption hypothesis, the detector was turned off after the last measurement, when it was not possible to extract more HF, and it was simply flushed for 20 days with the standard gas mixture. After 20 days, the chamber was flushed

with pure argon gas, and a voltage of 2.4 kV producing a total current of about 200 μA, was applied. A residual HF signal was still measured, and the HF accumulated reached the plateau at ≈ 14 μmol after ≈ 30 hours.

Since neither $C_2H_2F_4$ nor SF_6, but only argon was used, the HF could not be produced but could only be extracted from the inner gap surface. The current circulating in the argon forced the further extraction of the HF, which was bound to the inner detector surface. The argon plasma is associated with UV photons having energy around 15 eV, which are suitable for breaking F-C covalent bounds (around 5 eV) [61].

In conclusion, the HF measurements at GIF++ demonstrate that the HF production rate depends on the background rate and on the concentration depends on the gas flow. It has also been demonstrated that the HF can be trapped inside the gas gap if the gas flow is not sufficient with respect to the HF production rate, and it is possible to remove it (or partially remove it) operating the detector with argon.

4.2.2 HF study in CMS

HF measurements have been also performed in CMS during Run II (July - October 2018), in order to confirm the GIF++ results and to better investigate the observed ohmic current increase described in section 4.1.3.

The HF measurement method was the same as used at GIF++, and performed at the exhaust gas of three stations:

- Endcap RE+4, which operate with 1 gas volume exchange per hour, and where the background rate is ≈ 40 Hz/cm^2;
- Endcap RE+1, which operate with 0.6 gas volume exchanges per hour, and where the background rate is less than 10 Hz/cm^2;
- Barrel W0, which operate with 0.6 gas volume exchanges per hour, and where the background rate is less than 10 Hz/cm^2.

The fraction of exhaust gas flowing in the solution was kept constant at 0.5 l/h. The accumulated HF concentrations were periodically measured and are reported in Figure 4.12 (left) as a function of time.

All the three curves follow the same trend in time, driven by the LHC operation. The periods when the HF concentrations are constant and do not increase correspond to the Technical Stops periods, during which the detectors were off and therefore there was no HF production.

Stations RE+1 and W0 accumulated a similar amount of HF, indeed the operating conditions in terms of gas flow and background are similar. In RE+4 station the amount of HF accumulated is around 2.5 times higher than W0 and RE+1 stations, but in this case the background rate is around 4 times more, and the gas flow around two times greater.

The HF concentration follows a linear trend with respect to the integrated luminosity, shown in Figure 4.12 (right), in a similar way as it was observed for the ohmic current (see Figure 4.7). The linear dependence can be parametrized as:

$$HF = HF_0 + k_{HF} \times \mathcal{L}_{int} \tag{4.7}$$

$$k_{HF} = \frac{\partial HF}{\partial \mathcal{L}_{int}} \tag{4.8}$$

Where k_{HF} is the slope representing the HF variation with respect to the integrated luminosity variation. Since the differential of the integrated luminosity corresponds to the instantaneous luminosity, the HF production rate depends on the background rate. In agreement with the ohmic current analysis, the HF slope of RE+4 station is greater than the slopes of W0 and RE+1 stations, which are similar since the operating conditions. The results are in agreement with the GIF++ measurements, proving the HF dependence on the background rate and gas flow. Finally, Figure 4.13 shows the linear dependence between the ohmic currents and the HF concentration. The slope (k) represents the ohmic current variation with respect to the HF concentration rate:

$$k = \frac{\partial i_{ohmic}}{\partial HF} = \frac{k_i}{k_{HF}} \tag{4.9}$$

The RE+1 and W0 slopes are similar and small, with a low background rate. Consequently, the HF production is low, and the current stability shows that the gas flow is enough to efficiently remove the HF produced. On the other hand, the RE+4 slope

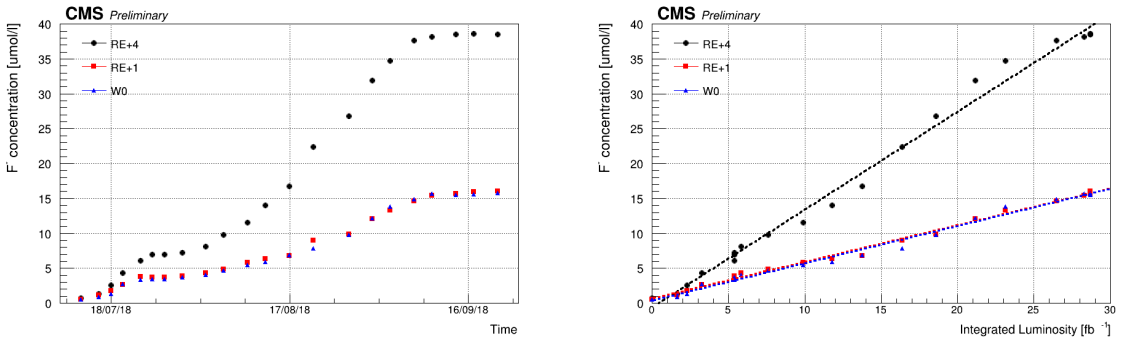

Figure 4.12: F^- concentration as a function of time (left) and as a function of the integrated luminosity (right). The measurements have been performed at the gas exhaust of 3 regions: W0 in the barrel and RE+1, RE+4 in the endcap.

is larger, the background rate is higher, the HF production is consequently higher, and the results show that the gas flow is not sufficient to efficiently remove the HF produced. Hence the HF likely to be trapped inside the gas gap damaging the inner surface and creating a thin conductive layer causing the observed ohmic current increase. From these results it is clear that the gas flow must be adjusted as a function

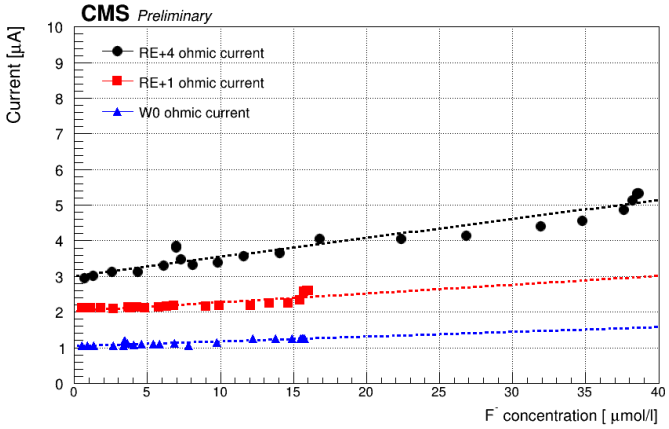

Figure 4.13: Ohmic current as a function of the F^- concentration.

of the background rate. A new parameter (G_r), that represents the gas volume exchanges per unit of background rate, is proposed to estimate the optimal gas flow to set as a function of the background.

$$G_r = \frac{gas\ volume\ exchanges\ per\ hour}{background\ rate} = \frac{l/h}{Hz/cm^2} \tag{4.10}$$

It was shown that W0 and RE+1 stations have almost stable ohmic current, therefore their G_r can be considered as an optimal value to use and to keep constant. For W0

and RE+1 it results $G_{rW0,RE+1} = 0.6/10 = 0.06\frac{vol/h}{Hz/cm^2}$, while for RE+4 $G_{rRE+4} = 1/40 = 0.025\frac{voll/h}{Hz/cm^2}$.

The G_r values of RE+4 is ≈ 2.5 times smaller than the W0 and RE+1, therefore the RE+4 gas should be increased by a factor ≈ 2.5.

The results are very important and have to be taken into account in view of the next LHC and HL-LHC runs, when the luminosity will increase.

In conclusion, for good detector operations it is necessary to fine tune the gas flow as a function of the background rate so that the HF is efficiently removed.

4.3 Long-term aging studies on CMS RPC for HL-LHC

The expected conditions during HL-LHC, in terms of background, pile-up and the probable aging of the present detectors, will make the muon identification and correct p_T assignment a challenge. The estimation of the expected operating conditions, and therefore the validation of the detectors, is crucial to maintain the excellent performance also during the HL-LHC period. Run I and Run II data have shown a linear dependence of the background rate and currents as a function of the instantaneous luminosity, as reported in Figure 4.2. Assuming this linear relation up to the maximum instantaneous luminosity foreseen during HL-LHC, the expected rates are shown in Figure 4.14 (left). A maximum rate per unit area of about $\approx 200\ Hz/cm^2$ was estimated. Including a safety factor of three, the RPC performance have to be evaluated up to a rate of 600 Hz/cm^2.

The maximum expected RPC integrated charge can be evaluated on the basis of the expected integrated luminosity at the HL-LHC, defining an upper limit up to which the RPC system needs to be tested for aging and radiation effects. The maximum expected integrated charge, by the end of HL-LHC, will be 280 mC/cm^2, as shown in Figure 4.14 (bottom). Including a safety factor of three, the detectors have to be certified up to 840 mC/cm^2.

HL-LHC will therefore be a challenge for the CMS RPC system, since the ex-

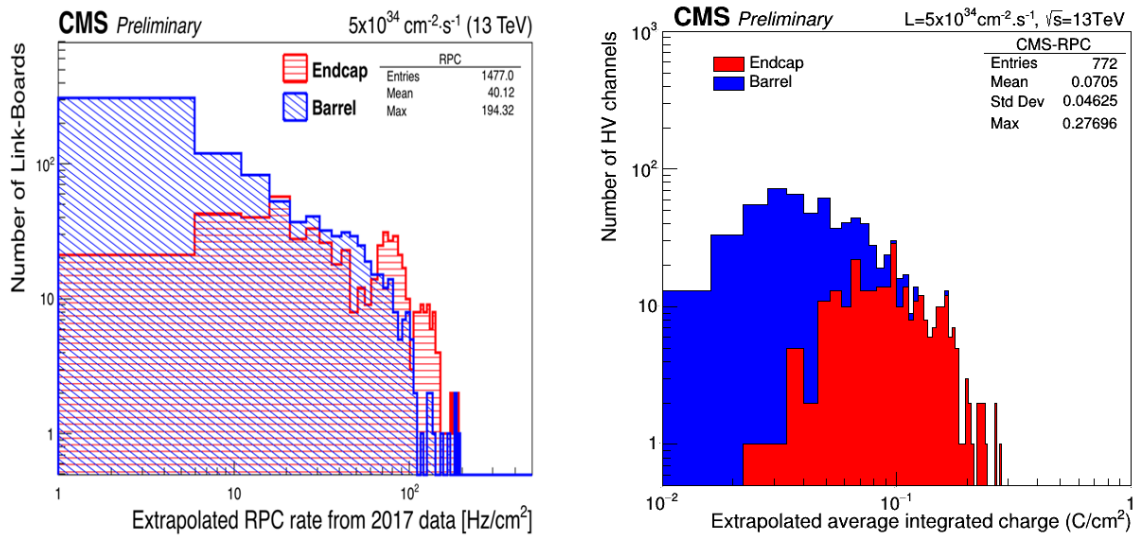

Figure 4.14: Linear extrapolation of the average background rate (left) and average integrated charge (right) expected during HL-LHC period at $5 \times 10^{34}\ cm^{-2}s^{-1}$ and 3000 fb^{-1}.

pected operating conditions are much harder with respect to those for which the detectors have been designed (described in chapter 3.1.4.3), and could induce non-recoverable aging effects that can alter the detector properties and performance. A new longevity test is therefore needed in order to evaluate the potential impact of the HL-LHC conditions [67,68]. The irradiation test aims to accumulate the equivalent charge expected at the end of HL-LHC, and to study the detector parameters and performance as a function of the integrated charge to spot any possible aging effect in order to confirm that the RPC system will survive to the expected HL-LHC conditions. Since 2016, a dedicated longevity study is ongoing at GIF++. The GIF++ layout is reported in Figure 4.15. The intense GIF++ gamma field background allows simulating the high background rate conditions that detectors will suffer during the HL-LHC operation.

Since the background rate distribution showed that the maximum background rate is in the endcap region, on July 2016 the irradiation test was started at GIF++ using four endcap chambers (from the spare production): two RE2/2 and two RE4/2. Two different types of chambers have been used for this test because the endcap RPC production has been performed in two periods: in 2005 for all RPCs in the endcap system, except the RE4/2 and RE4/3 chambers, which were made in 2012-2013. In order to study the longevity of the detectors, two chambers out of four (one RE2/2 and one RE4/2), are continuously operated under gamma irradiation, while the remaining

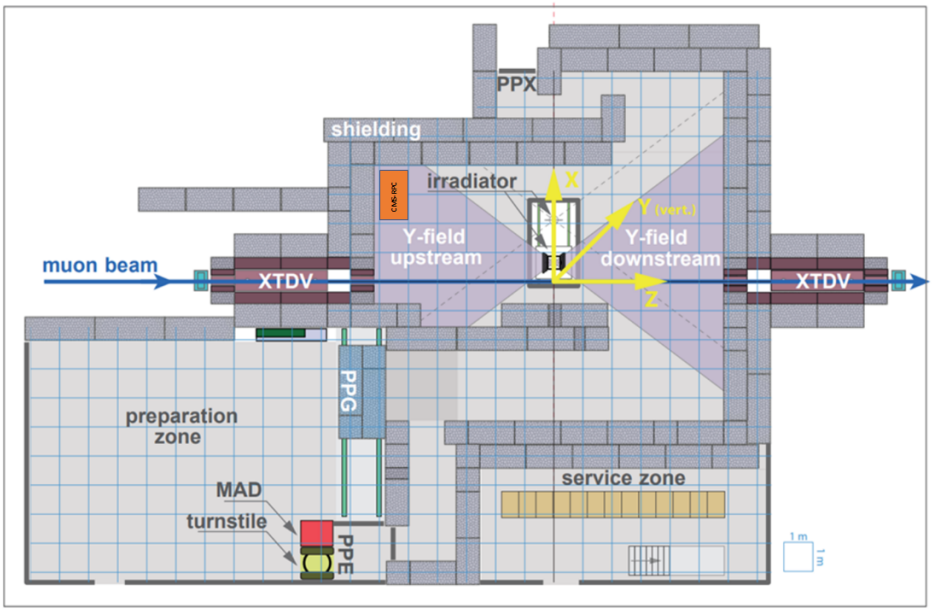

Figure 4.15: CERN Gamma Irradiation Facility (GIF++) layout.

two chambers are turned on only time to time and used as reference.

A trolley, hosting the four chambers, is placed at $\approx 5\ m$ far from the gamma source, as shown in Figure 4.16 (left). Figure 4.16 (right) represents a sketch of the chambers' position with respect to the source. The chambers operated with the stan-

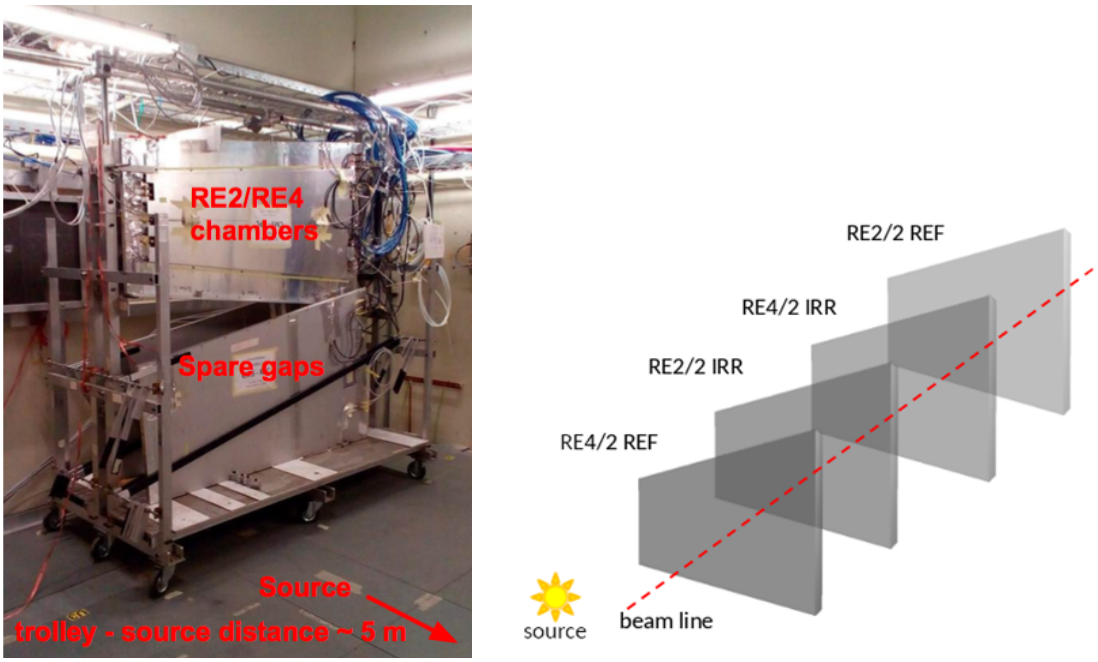

Figure 4.16: CMS RPC set-up at GIF++ for the longevity studies (left), and relative position of the chambers with respect to the source.

dard gas mixture and are irradiated at $\approx 600\ Hz/cm^2$ at the working point voltage

($\approx 9.8\ kV$). The small variations of GIF++ environmental temperature and/or pressure are compensated by correcting the electric field applied to the detectors accordingly, using Formula 4.11 [69, 70]. The high voltage applied (HV_{app}) to the detector is calculated normalizing the effective high voltage (HV_{eff}) wanted in the gas volume at the standard temperature and pressure. The reference values are $T_0 = 293.15\ K$, and $P_0 = 990\ mbar$, and the coefficients $\alpha = 0.8$.

$$HV_{app} = HV_{eff}\left(1 - \alpha + \alpha\frac{P_0}{P}\right)\frac{T}{T_0} \tag{4.11}$$

At present, about 600 mC/cm^2 and 328 mC/cm^2 have been integrated for RE2/2 and RE4/2 irradiated detectors, which correspond approximately to 71% and 39% of the expected HL-LHC integrated charge. Considering that the detector validation includes a safety factor of three, it means that the present accumulated charge in RE4/2 and RE2/2 already corresponds to the maximum expected integrated charge, and twice the maximum expected integrated charge at HL-LHC, respectively. The accumulated charge versus time is shown in Figure 4.17, for both RE2/2 and RE4/2 irradiated chambers.

Since the gamma flux is uniformly distributed over the detector surface, the integrated charge (Q_{int}) is calculated using Formula 4.12, as the average density current (J_{mon}) accumulated in time in the three gaps that constitute the detectors.

$$\begin{aligned} J_{mon} &= \frac{I_{mon}^{TW} + I_{mon}^{TN} + I_{mon}^{BOT}}{A_{TW} + A_{TN} + A_{BOT}} \\ Q_{int} &= \int_{t_i}^{t_f} J_{mon} dt \end{aligned} \tag{4.12}$$

The main detector parameters are monitored and periodically compared with those of the reference chambers. Moreover, when the muon beam is available, the detector performance is studied at different irradiation fluxes. The detectors parameters and performance monitoring results reported below refer to the RE2/2 chambers since the higher accumulated charge, but the results and conclusions are equivalent for the RE4/2 chambers as well.

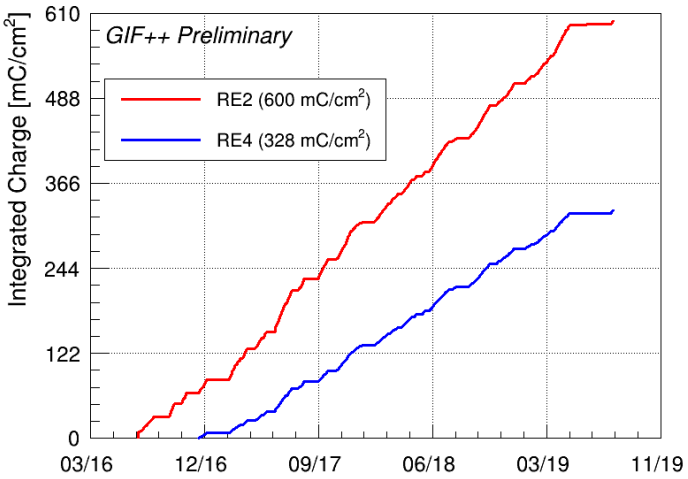

Figure 4.17: Integrated charge versus time, accumulated during the longevity test at GIF++ for RE2/2 (red) and RE4/2 (blue) irradiated chambers. The RE4/2 chamber has been turned on a few months later because of the total gas flow limitations. Different slopes account for different irradiation conditions during data taking.

4.3.1 Detectors parameters monitoring

The HPL bulk resistivity is periodically measured and monitored at GIF++, since it is a crucial parameter that influence the RPC performance. The long-term operation and the radiation-induced avalanche charge could cause a gradual change in the chemical composition of the HPL plates. As a result, an increase in the resistivity of the HPL plates is the consequence, which could result in a degradation of the rate capability of the RPCs [71]. In addition, the HPL resistivity is also strongly influenced by external conditions, like environmental humidity and temperature, which can affect the water content, and therefore its resistivity [72].

The bulk resistivity of the HPL plates in the RPC can be estimated by running the detector filled with pure Argon in a self-sustaining streamer regime [71]. Argon is characterized by a sufficiently high Townsend coefficient even when the applied electric field is relatively low ($\approx$ 2 kV for a 2 mm gap). Under these conditions, the gas conductivity is no longer negligible, a discharge appears and a kind of short circuit is created between the resistive anode and cathode, bypassing the spacers and the seal contribution to the total resistance. Indeed, if the gas quenching components (such as the isobutane) are removed, the UV photons are no longer absorbed and can ionize the gas far away from the point where the primary ionization occurred, thus propagating the streamers all over the detector area. This regime does not develop any spark

because the HPL plates resistivity limits the current.

Therefore, by measuring the current as a function of the applied high voltage, is possible to measure the resistance of the HPL plates, and from that their resistivity.

Figure 4.18 shows the characteristic current curve of the RE2/2 irradiated chamber operated with pure argon. At the "HV onset"[2] the transition of the detector to the self-sustaining streamer regime is evident. The slope of the current curve represents the reciprocal of the HPL bulk resistance for the operating current passing through the two resistive plates.

From the resistance is then possible to retrieve the HPL bulk resistivity as:

$$\rho = \frac{R \times S}{L} \tag{4.13}$$

Where R is the resistance measured, S corresponds to the HPL surface, and L is the cross sectional area corresponding to the HPL thickness 4 mm.

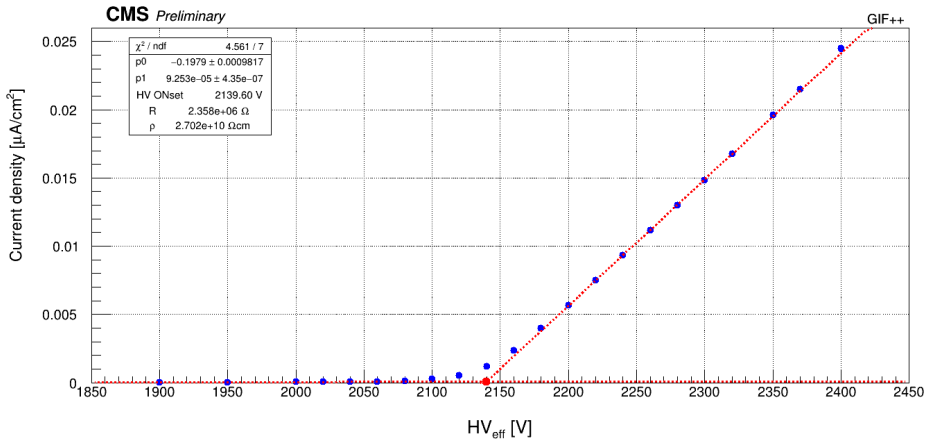

Figure 4.18: Characteristic current curve for the RE2/2 irradiated chamber operating with pure argon. In the statistics box, the fit parameters values, the resistance, the resistivity and the HV onset values are reported.

The argon method not only allows to measure the bakelite resistivity for the aging monitoring, but the test is sensitive to possible localized surface defects, which manifest as early discharge or current spikes.

Figure 4.19 (left) shows the resistivity monitoring as a function of time for both

[2]The "HV onset" represents the high voltage at which the transition of the detector to the self-sustaining streamer regime happens. The "HV onset", corresponds to the intercept of the current linear fit.

RE2/2 irradiated and reference chambers at GIF++. The resistivity value for each chamber is reported as the average with respect to the three gaps which made up a chamber.

Due to the temperature dependence, the measured resistivity values are normalized at $20^{\circ}C$ using Formula 4.14 [73,74], where $\alpha = 0.12/^{\circ}C$ represents the temperature-dependent coefficient, ρ and ρ_{20} is the resistivity measured and normalized at $20^{\circ}C$, and T is the environmental temperature during the resistivity measurement.

$$\rho_{20} = \rho \times e^{\alpha(T-20)} \tag{4.14}$$

The normalization allows monitoring and comparing measurements performed at different time. The monitoring results show almost stable resistivity values, and within the nominal range. Both irradiated and reference chambers follow the same trend due to the GIF++ environmental temperature and humidity variations. Nevertheless, the variations are more accentuated in the irradiated chambers.

Figure 4.19 (right) shows the resistivity ratio (blue), and the current ratio (red), between irradiated and reference chamber, to cancel out the dependence on the environmental conditions. A small but constant resistivity increase induced by the radiation in the irradiated chamber was observed in the first irradiation period, up to $\approx 300\ mC/cm^2$, when the detectors operated in similar conditions as in CMS: one gas volume exchange per hour and $\approx$ 35-45% of relative gas humidity. These operating conditions were optimized for CMS, but they are not optimal with respect to the high gamma background rate ($\approx 600\ Hz/cm^2$) at GIF++. Therefore, these conditions lead to a drying up of the HPL plates with the consequent resistivity increase, which is also confirmed by the currents.

At $\approx 300\ mC/cm^2$, the relative gas humidity was increased and maintained at $\approx 60\%$, and the gas flow was increased in the irradiated chambers at three gas volume exchanges per hour. The combinations of these effects allowed to reduce the HPL resistivity and mitigate the variations, proving that the resistivity increase depends on the operating conditions and it is a recoverable effect. In order to spot possible degradations of inner gap surface induced by the radiation, the detector noise rate and dark current are periodically measured when the GIF++ source is off, for both irradiated

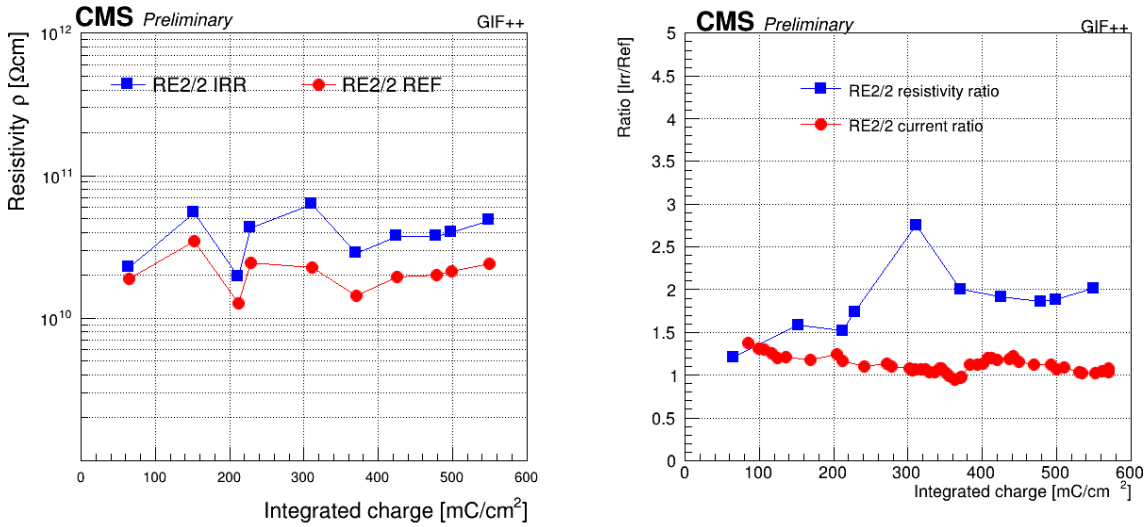

Figure 4.19: Left: average resistivity for both the irradiated chamber (blue) and the reference chamber (red), monitored as a function of the RE2/2 irradiated integrated charge. The resistivity value for each chamber is the average with respect to the three gaps which made up a chamber. The resistivity values are corrected for the temperature variation and normalized at $20^{\circ}C$. Right: resistivity ratio (blue) and current ratio (red) between irradiated and reference chamber.

and non-irradiated reference chambers. Figure 4.20 (top) shows the RE2/2 dark currents curves measured at different integrated charge values. Figures 4.20 (bottom left) and (bottom right) show instead the dark currents monitoring of both RE2/2 irradiated and reference chambers, as a function of the integrated charge. The dark currents were measured at 6.5 kV (left), which represent the ohmic contribution, and at 9.6 kV (right), which also includes the gas amplification. The dark current is almost stable in time, a part from negligible small variations that follow the environmental temperature and humidity. No significant dark current variations have been observed so far, and the values remain low as measured during the chamber production certification. In particular, no ohmic current increase was observed as for the detectors installed in CMS (see section 4.1.3), but the different detector operating mode[3] at GIF++, and the different background conditions, in terms of rate, kind of particles and energy spectrum, could induce slightly different phenomena. Figure 4.21 (left) shows the average noise rate at 9.6 kV, monitored as a function of the integrated charge for both the RE2/2 irradiated and reference chambers. The mean noise rate is calculated as the average among all 96 strips distributed over the three detector η partitions. The electronics threshold is

[3]The RPCs installed in CMS follow the LHC beam cycle, they operate at working voltage for around 8-12 hours during the "physics beam", and then in standby during the interfill. At GIF++ instead there is not a defined source cycle but the irradiation conditions follow the users requests.

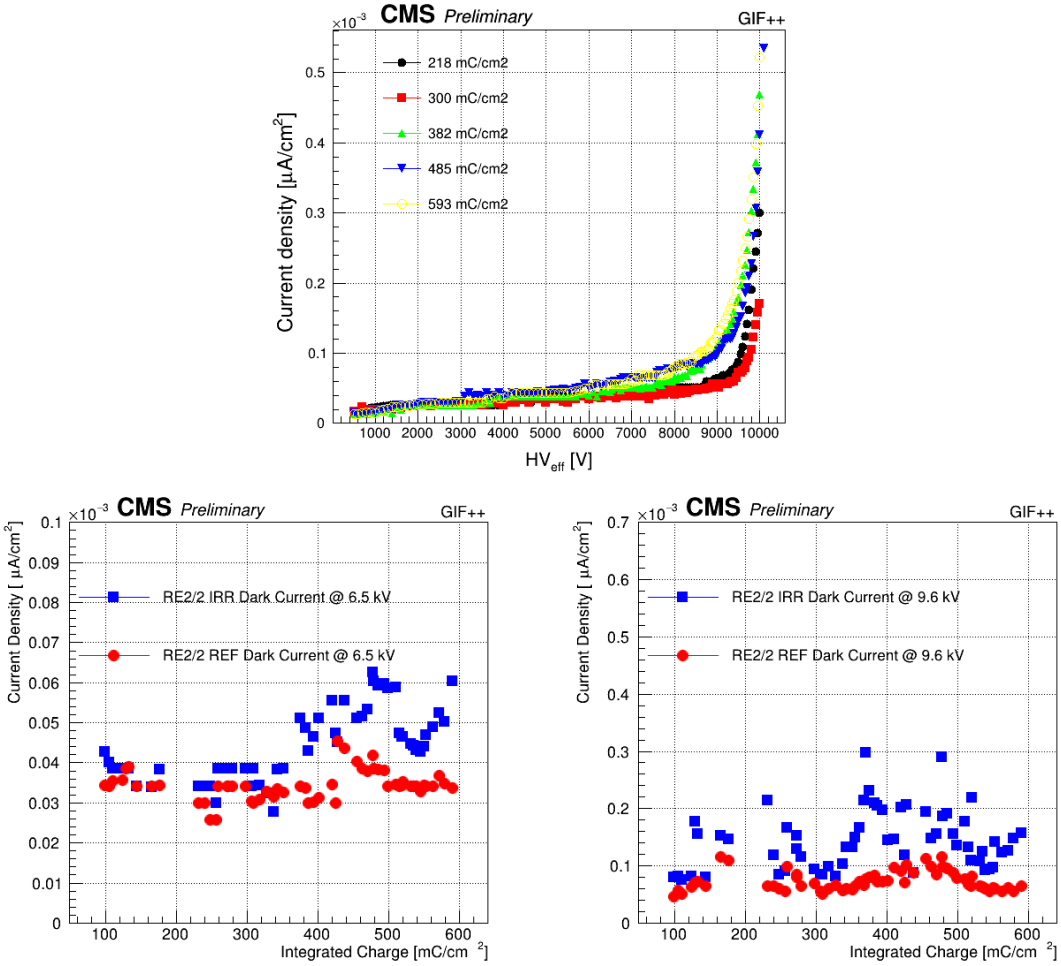

Figure 4.20: Top: RE2/2 irradiated chamber currents curves at different integrated charge values. Bottom left and Right: RE2/2 irradiated (blue) and reference (red) chamber currents monitoring versus the integrated charge, at 6.5 kV (left), and at 9.6 kV (right).

set at 220 $mV \approx 150\ fC$, as for the detectors installed in CMS. Figure 4.21 (right) represents the noise rate strip profile of the RE2/2 irradiated chamber, measured after having collected different amount of integrated charge. The noise rate is stable in time and lower than 1 Hz/cm^2.

The low and stable dark current and noise rate indicate a good state and quality of the inner gaps surface, excluding any possible aging damage so far.

4.3.2 Detectors performance monitoring

During the test beam (TB) periods, the detectors performance is tested at different background conditions, and it is monitored to spot possible aging effects induced by the radiation.

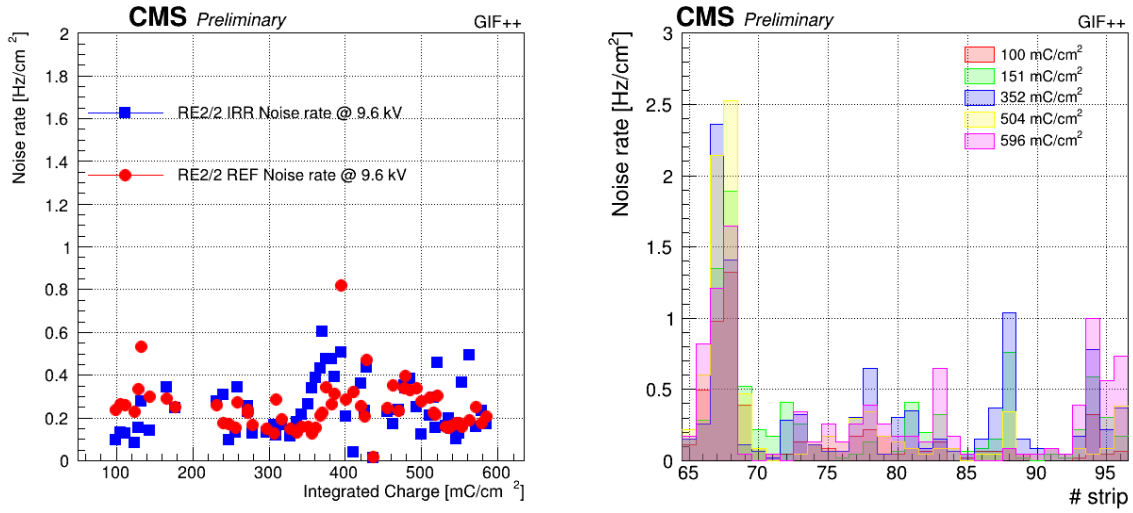

Figure 4.21: Left: average noise rate versus the integrated charge, for RE2/2 irradiated (blues) and reference (red) chamber, at 9.6 kV. The electronics threshold is set at 220 $mV \approx 150$ fC. Right: RE2/2 noise rate strip profile at different integrated charge values, at the working point voltage.

For the performance test, the beam trigger system is composed of three scintillators, as reported in Figure 4.22. Two are placed outside on each side of the GIF++ bunker (S_{up} & S_{down}), in order to be shielded from the gammas background and to avoid fake coincidences, and the third scintillator (S_n) is placed near to the tested chambers. A minimum of 5000 muon triggers, provided by the coincidence of the three scintillators, was required in order to accumulate enough statistics for reliable computation of the detectors performance.

In addition, in order to discriminate noise or gammas from muons, as muons are the only particles that pass through the full set-up, two RPCs prototypes are placed near the tested chambers and they are used as offline tracking system, to reconstruct muon tracks and to correlate them with the hits recorded in the tested chambers. The two RPCs prototypes are 2 mm double gap detectors with HPL plates, and were kept at fixed working point voltage (≈ 9.8 kV).

The tracking system allows to obtain higher accuracy and more reliable measurements, since the analysis algorithm is based not only on the scintillators coincidence, but a geometrical and time selection is applied [75, 76]. The offline analysis algorithm is briefly summarized below. First of all, the fired strips of each detector are clustered, the center of gravity and the cluster size are computed for each cluster. The cluster is constructed out of adjacent strips giving a signal at the same time (hits within a time

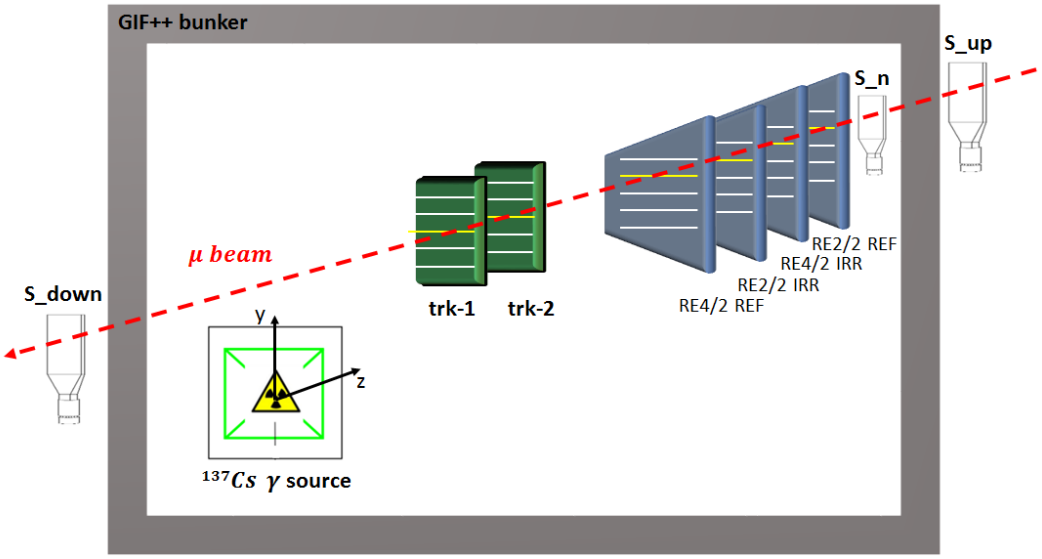

Figure 4.22: GIF++ beam trigger, composed by threes scintillators: two placed outside on each side of the GIF++ bunker (S_{up} & S_{down}), in order to be shielded from the gamma background and to avoid fake coincidences, and the third scintillator (S_n) is placed in near to the tested chambers. Two additional RPCs (trk-1 & trk-2), represented in green, are used as tracking system.

window of 10 ns).

A first events selection, in order to eliminate the spurious signal generated by the detector noise or by the gamma background, is done considering only hits within the Gaussian distribution of the time profile. Figure 4.23 (left) shows a typical time profile of the RE2/2 irradiated chamber, which represents the time distribution at which the hits are recorded within the trigger time window. In the case reported as example, the hits are picked at ≈ 330 ns in the trigger time window, with a standard deviation of ≈ 17 ns.

A geometrical events selection is applied as well. Only the hits within the muon strip profile are considered. The 2D plot, reported in Figure 4.23 (right), shows the typical time profile (Y-axis) and strip profile (X-axis) of the RE2/2 irradiated chamber. It is possible to clearly distinguish the beam profile, which corresponds to the hits centred at the strip 81 ± 5 strips, and recorded at $\approx 330 \pm 17$ ns in the trigger time window. It is also possible to distinguish the beam halo, which corresponds to the hits recorder in-time within the Gaussian time distribution, but spread far from the center strip 81. Finally, the remaining hits, out-time the Gaussian time distribution and far from the center strip 81, represent the detector noise or gamma background hits. After

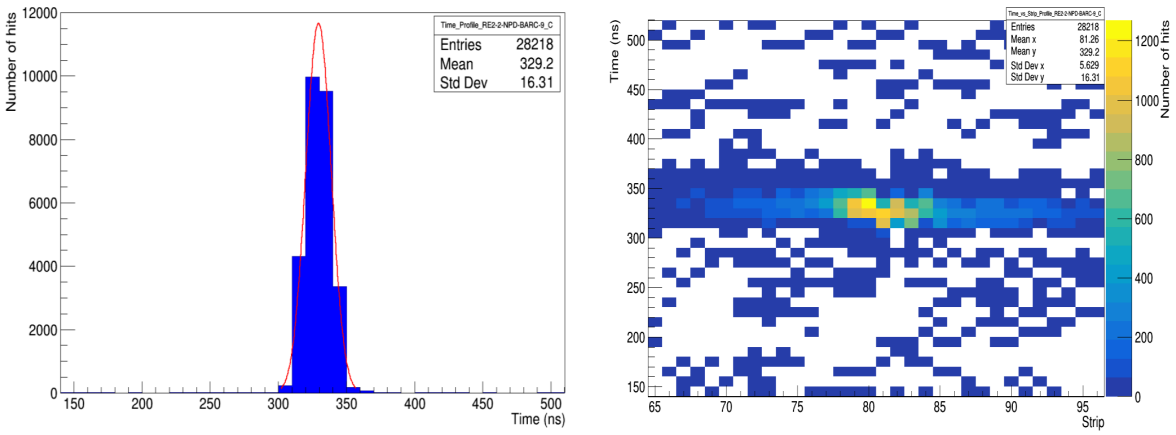

Figure 4.23: Time profile (left): typical Gaussian distribution of RE2/2 irradiated chamber hits recorded within the trigger time window. Right: 2D plot shows on the Y-axis the RE2/2 irradiated chamber time profile distribution, and on the X-axis the beam strip profile.

the first events selections, a more accurate analysis is done using the tracking system. For the tracking chambers, due to the fact that only two detectors are used for the tracks reconstruction, only "clean" events having one cluster are considered. If a cluster is found in both tracking chambers, with less than two strips difference, the event is considered generated by a muon.

After the reconstruction, the muon track is projected from the tracking chambers to the chamber under test. Since the tracking chambers can be not perfectly aligned with the tested chambers, and they have different strip size and pitch, calibration test without background radiation are performed to obtain the linear function, that associate the tracking chambers hits to the tested chamber hits. An example of the calibration test, that associate the tracking chambers hits to the tested RE2/2 irradiated chamber hits, is reported in Figure 4.24 (left).

A typical distribution of the difference between the projected cluster in the chambers under test and the fired cluster center, is plotted on Figure 4.24 (right). The root mean square of the distribution represents the spatial resolution of the chamber, and is due to the strip width. The chamber is considered efficient if a reconstructed muon trajectory goes through a fired strip or its neighbours (± 2 strips). The efficiency (ϵ) is therefore evaluated using Formula 4.15, as the ratio between the number of muon tracks detected by chamber under test (N_e) and the number of reconstructed muon

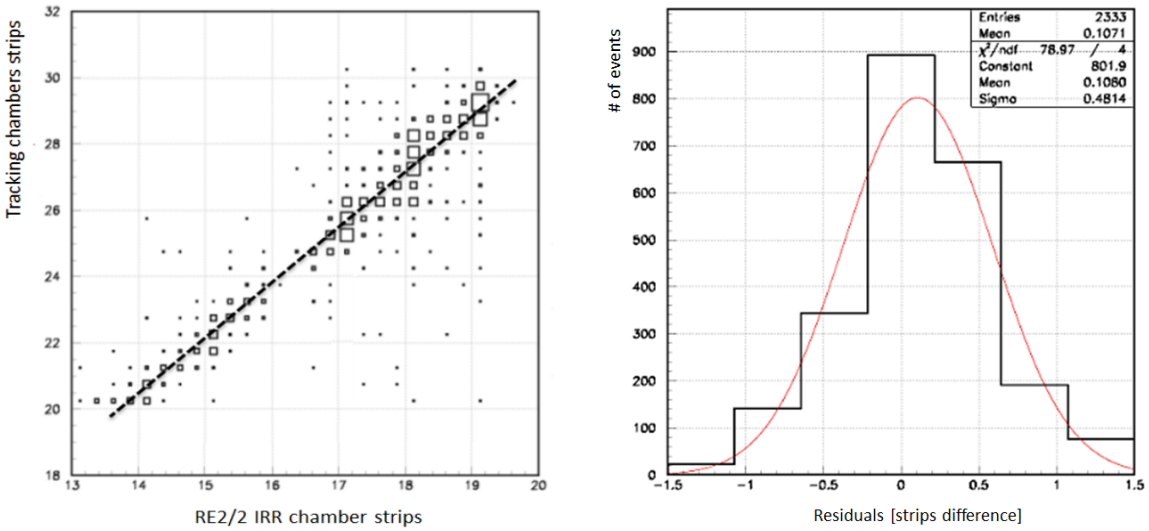

Figure 4.24: Left: result of the calibration test to obtain the linear function, that associate the tracking chambers hits to the tested RE2/2 irradiated chamber hits. Right: typical Gaussian fit of the residual distribution of RE2/2 irradiated chambers. The residuals are calculated as the difference between the expected fired strip, found from the projected muon track, and the fired cluster center.

tracks (N_{trk}).

$$\epsilon = \frac{N_e}{N_{trk}} \tag{4.15}$$

Figure 4.25 shows the typical RE2/2 irradiated chamber efficiencies curves as a function of the effective high voltage, measured with muon beam at different background radiation.

The data are fitted with a sigmoid function described in Formula 4.16, where ϵ_{max} is the maximal efficiency of the detector, λ is proportional to the slope at half maximum and HV_{50} is the voltage value at which the efficiency reaches half of the maximum.

$$\epsilon(HV_{eff}) = \frac{\epsilon_{max}}{1 + e^{-\lambda(HV_{eff} - HV_{50})}} \tag{4.16}$$

The sigmoid function allows to define two important parameters: the "knee", defined as the voltage at 95% of the maximum efficiency, and the "working point" defined as the $HV_{knee} + 100V$ for the barrel and $HV_{knee} + 150V$ for the endcap.

As shown by the plot, the efficiency decrease when the background rate increase, if the voltage is not increased as well. At very high rate, the flow of total current through the plates becomes important and produces a drop of voltage across them. A lower voltage is therefore applied to the gas gap, resulting in a lower gas amplification. The

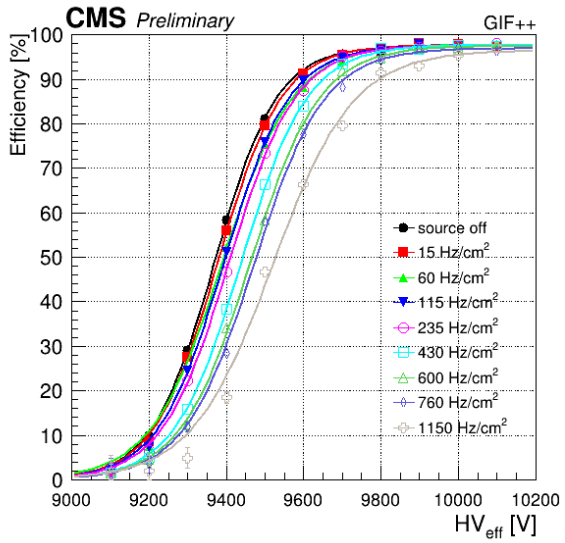

Figure 4.25: Typical RE2/2 irradiated chamber efficiencies as a function of the effective high voltage, measured with muon beam at different background radiation. The Front End Board (FEB) is the standard CMS RPC electronics, and the applied threshold is 220 $mV \approx 150\ fC$, as applied in CMS [39].

detector performance has been tested before starting the longevity test and repeated after different irradiation periods. Figure 4.26 shows the RE2/2 irradiated chamber efficiency as a function of the effective high voltage, without irradiation (left), and with $\approx$ 600 Hz/cm^2 of gamma background rate (right). The performance without background is stable in time, while with the background rate the efficiency remains stable at working point, however a $\approx 100V$ shift was observed, after having accumulated $\approx$ 378 mC/cm^2. The working point shift is related to the HPL resistivity increase described in section 4.3.1. Indeed, the voltage applied (HV) is reduced by the voltage drop (dV) across the electrodes, which is proportional to the HPL resistance (R) and to the current (I) produced by the ionizing particles (the dark current (I_0) is subtracted). The effective voltage applied to the gas (HV_{gas}) is therefore defined as:

$$HV_{gas} = HV - dV = HV - [R \times (I - I_0)] \tag{4.17}$$

The detector operation regime is invariant with respect to HV_{gas}. The use of HV_{gas} in place of HV allows describing the system independently from the voltage drop due to the background current and HPL resistance [71, 77–79].

The efficiency scaling behaviour is verified in Figure 4.27 (left), which represents the RE2/2 irradiated chamber efficiency curves measured at different background ra-

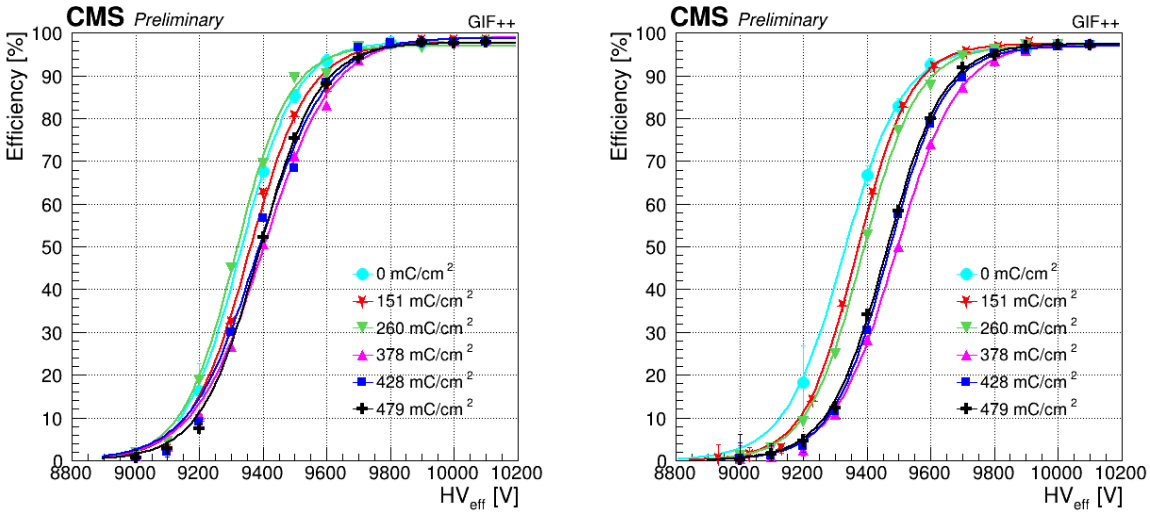

Figure 4.26: RE2/2 irradiated chamber efficiency as a function of the effective high voltage, taken without background (left) and under gamma background rate of about 600 Hz/cm^2 (right). The efficiency is measured during different TB corresponding to different fractions of the target charge to integrate.

diation (up to $\approx$ 600 Hz/cm^2) and at different integrated charge. All the efficiency curves overlap, and no working point shift is observed anymore since the increase of the HPL resistivity effect has been removed.

The resistance value, used in the Formula 4.17, is found by minimizing the spread of the high voltage (HV) and the current (I), measured at different background, with respect to the high voltage (HV_0) and current (I_0) measured without background, assuming that the high voltage applied without background corresponds to the voltage applied to the gas. The R value, derived from the Formula 4.17, is then given by:

$$R = \frac{\Delta V}{\Delta I} = \frac{HV - HV_{gas}}{I - I_0} = \frac{HV - HV_0}{I - I_0} \tag{4.18}$$

This procedure was repeated for different sets of data, and the obtained resistance values are shown in Figure 4.27 (right) as a function of the accumulated charge. The plot shows the resistivity values estimated using the HV rescale correction and the values measured with argon. The resulting resistivity values are consistent and almost the same for both methods, and additionally the good scaling of the efficiency curves versus HV_{gas} proves the reliability of the R estimation. The detectors performance has been measured at different background radiation conditions. Figure 4.28 shows the RE2/2 irradiated chamber efficiency at the working point as a function of the

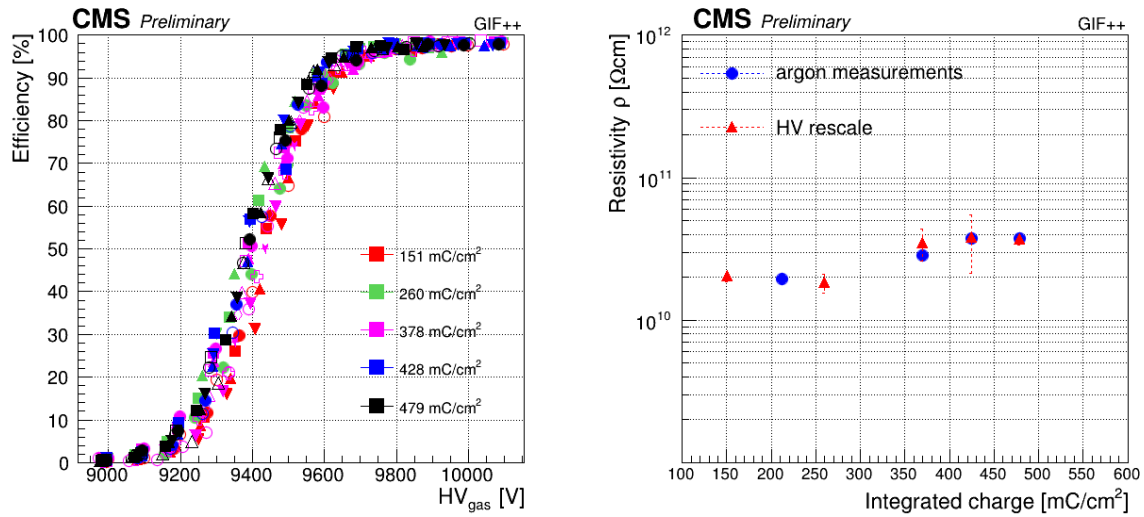

Figure 4.27: Left: RE2/2 irradiated chamber efficiency as a function of the HV gas, at different background irradiations and at different integrated charge values. Right: monitoring of the RE2/2 irradiated chamber resistivity, measured with argon and estimated with the HV rescale method.

background rate, measured at different accumulated charge. The efficiency is stable in time, with a 2% decrease at the highest expected background rate, 600 Hz/cm^2. This result proves the detectors efficiency stability, and overall that the detectors are able to work efficiently at the maximum expected rate during HL-LHC. Figure 4.29 and Figure

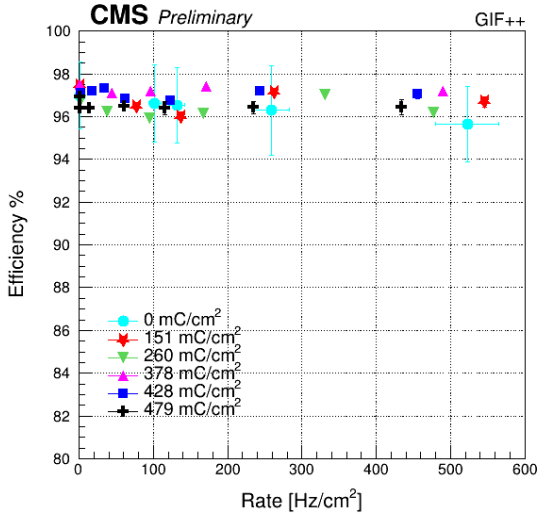

Figure 4.28: RE2/2 irradiated chamber efficiency at working point as a function of the background rate, measured at different integrated charge values.

4.30, show the monitoring results of current, deposited charge, gamma cluster size and muon cluster size at working point, measured for the RE2/2 irradiated chambers during different TB, corresponding to different fractions of the target charge to integrate.

The deposited charge represents the average charge produced per avalanche, and it is estimated using Formula 4.19, as the ratio between the current (J_{mon}) and the cluster rate (r_c), where the cluster rate is defined as the ratio between the hit rate and the cluster size.

$$\langle q \rangle = \frac{J_{mon}}{r_c} \tag{4.19}$$

All the results of the longevity test at GIF++ show stable detectors parameters and performance, after having collected a significant amount of integrated charge, $\approx 600\ mC/cm^2$, which correspond to ≈ 2.5 the expected integrated charge at HL-LH without considering the safety factor. Moreover, unlike in CMS, no significant dark current increase has been observed. Definitely, no evidence of aging effects have been observed so far.

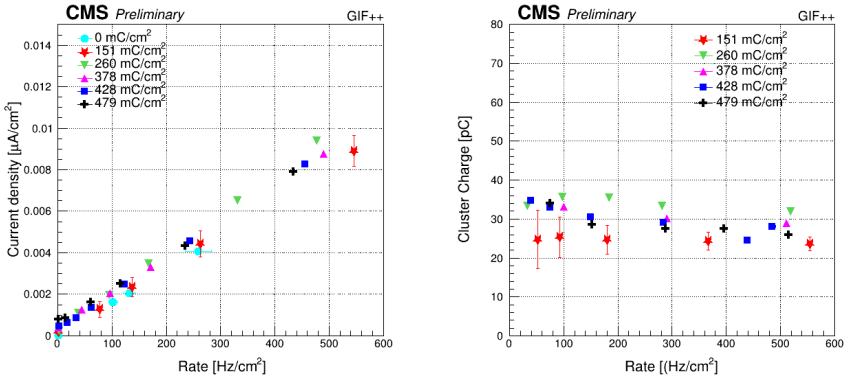

Figure 4.29: RE2/2 irradiated chamber density current (left) and deposited charge (right), measured at the working point as a function of the background rate, at different integrated charge values.

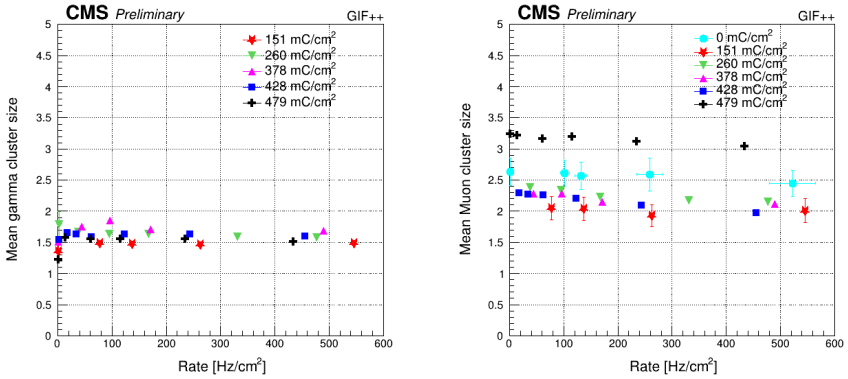

Figure 4.30: RE2/2 irradiated chamber gamma cluster size (left) and muon cluster size (right), measured at the working point as a function of the background rate, at different integrated charge values.

5

Extension of the CMS RPC system to the very forward region

In view of HL-LHC, the muon upgrade program will enhance the muon system robustness by installing additional detectors in the high $|\eta|$ region, complementing the already existing CSC chambers there. The third and fourth stations (RE3/1 and RE4/1), in the pseudorapidity region $1.8 < |\eta| < 2.4$, will be equipped with new iRPC detectors: 18 new chambers per muon disk, 72 chambers in total, will be added.

The main reasons for the RPC system extension at the high eta region are:

- The RE3/1 and RE4/1 chambers complement the CSC stations ME3/1 and ME4/1 and enhance the local muon measurement by adding track hits and by increasing the lever arm. Additionally they will help in resolving ambiguities in the endcap trigger for multiple tracks.

- The intrinsic time resolution is improved when the measurements of RE3/1 and RE4/1 are combined with those of the existing CSC chambers. This improves background hit rejection and identification and reconstruction of slowly moving Heavy Stable Charged Particles (HSCP) [80].

- The new RE3/1 and RE4/1 station will increase the redundancy in the difficult endcap region.

The simulated overall impact of the inclusion of RPC hits into the L1 single muon trigger can be seen in Figure 5.1 (right), showing the efficiencies with and without the use of the RPC information. A clear improvement at the level of 15% can be seen with

the iRPC contribution. In case of any CSC trigger problems in ME3/1 and ME4/1, additional improvement would be expected.

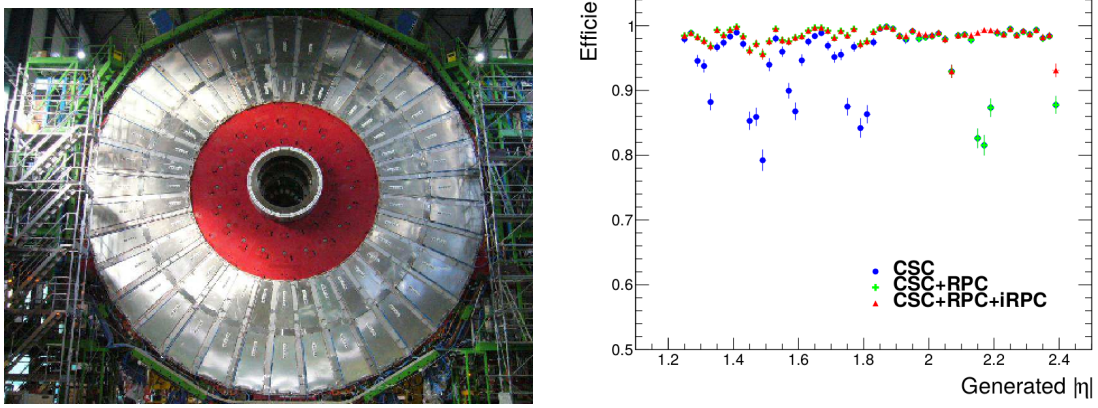

Figure 5.1: Left: View of CMS disk 3 positive, instrumented with RPC in the rings 2 and 3, while the first ring is empty (in red). Right: Simulated comparison between the L1 single muon trigger efficiencies with and without the RPC information, as a function of $|\eta|$. The contribution of iRPC starts above $|\eta| = 1.8$

The basic requirement for the new detectors to be installed in the RPC stations RE3/1 and RE4/1 are the following [45]:

- Time resolution: order of 1.5 ns.
- Spatial resolution: a slightly finer ϕ segmentation of 0.2° is motivated by the lower bending power of the magnetic field in this region. This corresponds to strips with an average pitch of 1 cm, about a factor of two smaller than the average strip pitch of the chambers in the present endcap RPC.
- Rate capability: the expected average background rate will be $\approx$ 2 kHz/cm^2, including a safety factor three [45].

5.1 iRPC technology

To fulfil the requirements, an improved version of the RPCs has been developed [81,82]. During the last years several prototypes have been built, based on the RPC technology, but having different geometry configurations (gas gap and plates thickness) and plates materials. To improve the rate capability it is necessary to short the recovery time of

the electrodes and to reduce the total charge produced in a discharge. Figure 5.2 shows the average charge per avalanche drawn in double-gap RPCs having different gas gap thicknesses, ranging between 1.0 and 2.0 mm, as a function of the electric field strength. The standard CMS RPC gas mixture was used for the measurements. The thinner gap thicknesses more effectively retard the fast growth of the ionization avalanches charge. This implies that the use of the thinner gaps will effectively preserve the size of the operational plateau when the digitization threshold is lowered to enhance the detection sensitivity. The reduction of the operational high voltage, as result of decreased gap thickness and of the digitization threshold, will reduce the risk of detector aging, and it will also improve the robustness of the high voltage system.

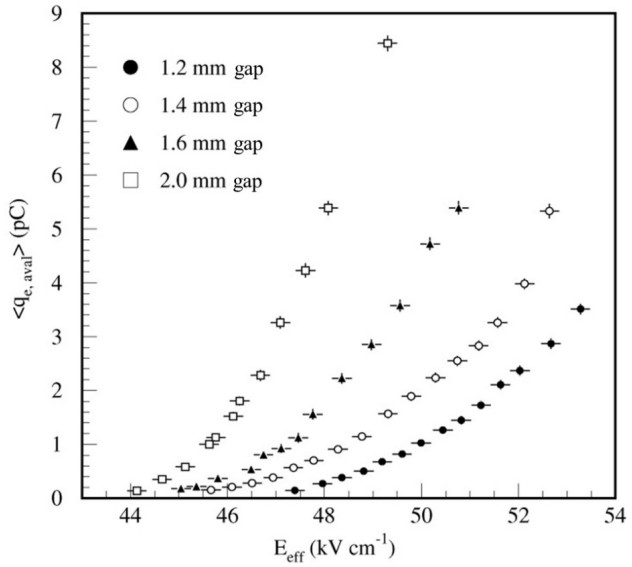

Figure 5.2: Average charge per avalanche measured on 1.2 mm (full circles), 1.4 mm (open circles), 1.6 mm (triangles), and 2.0 mm (squares) double-gap RPCs, as a function of the electric field strength [81]. Test performed at the KOrean DEtector Laboratory (KODEL).

The iRPCs will use thinner HPL plates and a narrower gas gap, both reduced from a thickness of 2 mm to 1.4 mm. Thinner gas gaps would be more sensitive to non-uniformities in the distance between the plates, and the value of 1.4 mm is a safe compromise. The HPL resistivity has been specified to be in the range from 0.9 to 3×10^{10} Ωcm, which is about of a factor of two less than in the present RPC system. The resulting loss in gas gain will be compensated by the higher signal amplification in the new improved front-end electronics (see chapter 5.1.2). The iRPC will maintain the double-gap configuration with the signal pick-up strips in the middle.

5.1.1 iRPC performance at GIF++

Extensive test performed at GIF++ with a muon beam allowed to validate the iRPC performance under different background conditions. A large size trapezoidal iRPC prototype-1 ($height$ = 1613 mm , $long\ side$ = 866.3 mm, $short\ side$ = 584.1 mm), having 2 cm wide strips, and equipped with a voltage-sensitive-mode FEB that apply 300 μV $\approx$ 50 fC threshold, was tested [83]. In Figure 5.3 the efficiency and the average muon cluster size are plotted as a function of the effective high voltage, in absence of background (left) and with a gamma background rate of $\approx$ 2 kHz/cm^2 (right). The algorithm used for the efficiency measurements is the same described in chapter 4.3.2.

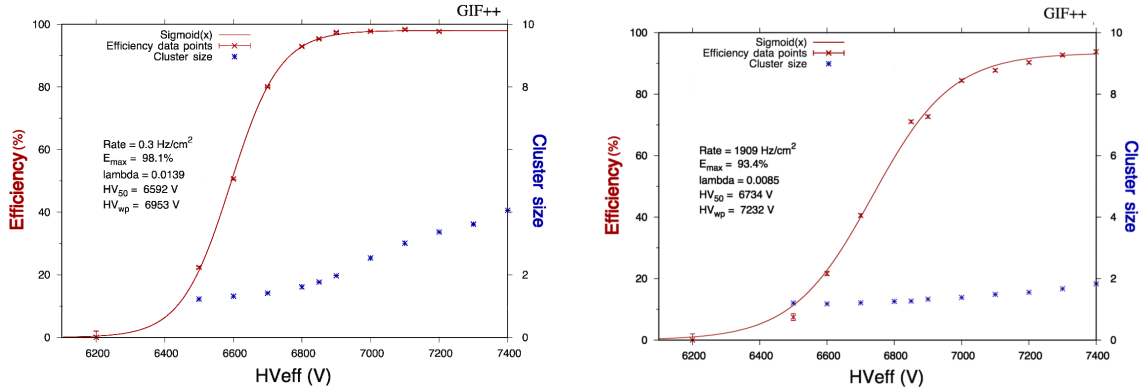

Figure 5.3: Efficiency and average cluster size of a 1.4 mm double-gap iRPC (prototype-1) as a function of the effective high voltage, tested without gamma background (left) and under a gamma background rate of $\approx$ 2 kHz/cm^2 (right). The measurements were performed applying a 300 μV $\approx$ 50 fC threshold.

Figure 5.4 (left) confirms that in absence of background the efficiency at working point is around 98%, and it decreases of around 5% under the expected background rate at HL-LHC. The shift in the working voltage is less than 300 V as reported in the center plot, while the right plot shows the almost stable average muon cluster size at working point as a function of the background rate.

In spite of the lower front-end electronics threshold, in absence of background the intrinsic noise rate has been measured to be on average about 0.2 Hz/cm^2.

Finally, the iRPC average charge per avalanche was quantified and compared with the standard RPC. Figure 5.5 shows the average charge measured at working point for the standard RPC (black) $\approx$ 27 pC, and for the iRPC (red) $\approx$ 9 pC. The lowered FEB threshold and the narrow gas gap thickness of the iRPC, allowed to obtain an average

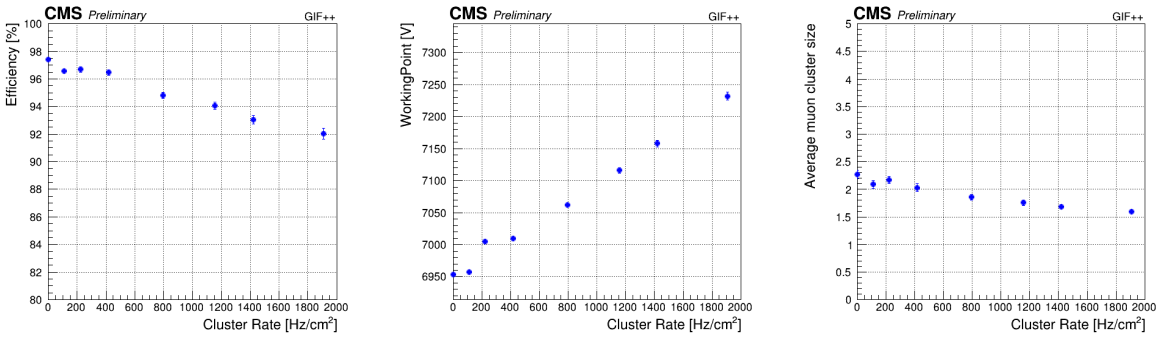

Figure 5.4: iRPC efficiency at working point (left), working point (center) and average muon cluster size at working point (right), as a function of the gamma background cluster rate. The measurements were performed applying a 300 μV $\approx$ 50 fC threshold.

charge $\approx$ 3 times smaller with respect to the standard RPC.

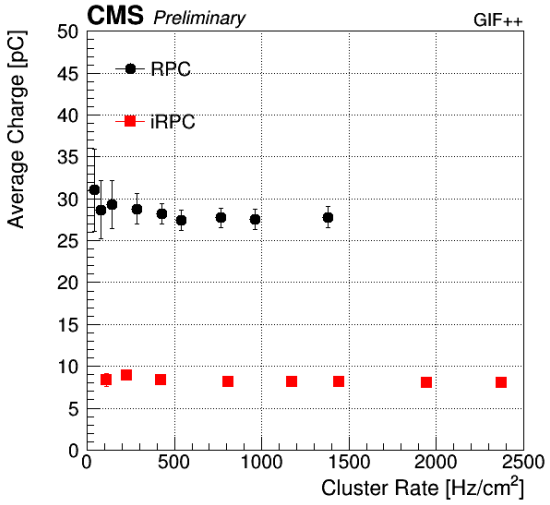

Figure 5.5: Average avalanche charge at working point, as a function of the cluster rate, measured for the standard RPC (black) and iRPC (red).

5.1.2 The new iRPC front-end electronics

A new board equipped with low noise front-end electronics, has to be able to detect smaller signal, has to be fast and reliable, and it must sustain the high irradiation environment that will prevail in RE3/1 and RE4/1 during the HL-LHC phase [45, 84]. The new FEB design, presented in Figure 5.6, uses the ASIC PETIROC, based on SiGe technology, it includes a fast preamplifier with an overall bandwidth of 1 GHz and a gain of 25, for each of the 32 channels [85]. The ASIC is controlled with a Cyclone V Altera Field Programmable Gate Array (FPGA) that includes a Time Digital Converter

(TDC) to measure the signal arrival time. The strips are read out from both ends, and the arrival time difference of the two signals is used to determine the particle position along the strip (η position). A real size iRPC prototype, equipped with the new FEB

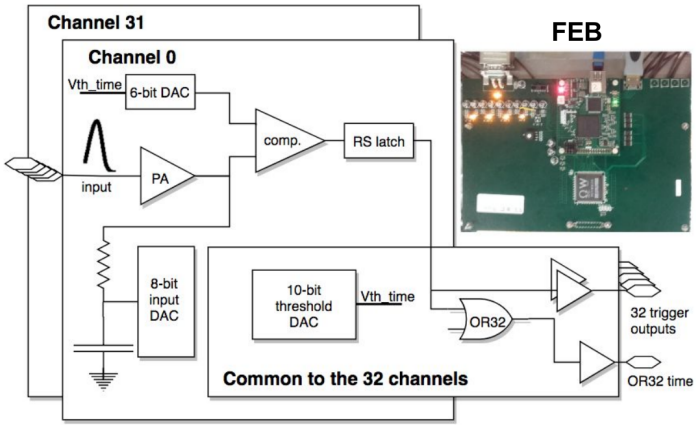

Figure 5.6: Front Electronics Board that hosts one PETIROC ASIC and the FPGA that includes the TDC (top right) and the schematics of the PETIROC ASIC (left).

and a readout PCB having average strips pitch of 0.75 cm, was tested at GIF++ with muon beam at different gamma background rate [84]. The muon trigger system was made of 4 scintillators: 2 externals to the GIF++ bunker, and two placed near the chamber. Figure 5.7 (left) represents the efficiency as a function of the effective high voltage measured at different particle rate. The results show that efficiencies higher than 95% are reached at the expected HL-LHC background rate of $\approx$ 2 kHz/cm^2. Figure 5.7 (right) shows the evolution of the efficiency at working point as a function of the background cluster rate. The muon efficiency was calculated as:

$$\epsilon = \frac{\frac{N}{N_{trg}} - \frac{N_{bkg}}{N_{trg}}}{1 - \frac{N_{bkg}}{N_{trg}}} \tag{5.1}$$

where ϵ is the measured muon efficiency, N is the number of muon events detected by the chamber from both ends of the strips, N_{trg} is the number of the muon triggers, and N_{bkg} is the number of the gamma background hits expected in the time interval. The average noise rate measured at a threshold of 81 fC does not exceed 5 Hz/cm^2.

The measurements of the time characteristics of the chamber were carried out using the muon beam provided by the CERN SPS H2 beamline. The chamber was mounted on a 100 micron-precision movable table that allows changing the positions

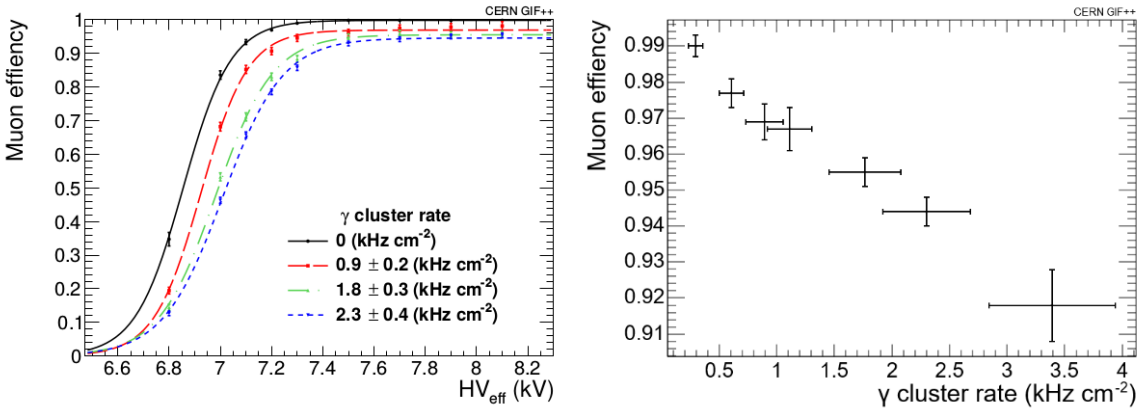

Figure 5.7: Left: efficiencies as a function of the effective high voltage measured at different background rate. Right: evolution of the efficiency at working point at different background cluster rate. The measurements were performed with 81 fC threshold.

of the detector with respect to the beam. The scintillators schema was similar to that used at GIF++.

A scan along the detector was performed and the hits' position was determined by using the time information from both ends of the strip, according to the Formula 5.2:

$$Y = L/2 - v \times (T_{HR} - T_{LR})/2 \tag{5.2}$$

Here T_{HR} and T_{LR} are the arrival times from the strip ends, v is the signal propagation velocity and L is the total strip length.

Figure 5.8 (left) shows the difference of the signal arrival time of each of the two fired strip ends as a function of the moving table position. The linear behaviour allows a fit of v. The propagation velocity was found to be 18 cm/ns, in good agreement with the expected theoretical value.

Figure 5.8 (right) shows the distribution of the difference between the arrival time from the strips ends. A time resolution of 177 ps was observed at the center of the detector. This excellent resolution allows the determination of the position along the strips with a spatial resolution of ≈ 1.7 cm, calculated using the Formula 5.3:

$$\sigma(Y) = v \times \sigma(T_{HR} - T_{LR})/2 \tag{5.3}$$

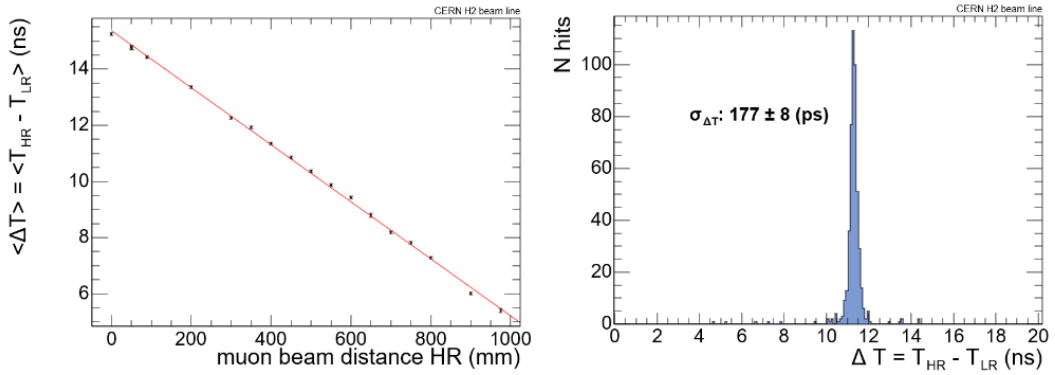

Figure 5.8: Left: measured time difference of the signal arrival time of each of the two fired strip ends $T_{HR} - T_{LR}$ as a function of the position of the muon beam with respect to the RPC. Right: time resolution at the center of the detector.

To estimate the detector absolute time resolution, two identical iRPC chambers, equipped with the same kind of FEB, were used. The arrival time difference of the signals coming from the two chambers, crossed by the same muon, was measured and reported in Figure 5.9. The detector absolute time resolution was deduced by dividing the estimated resolution of time difference by $\sqrt{2}$, with the assumption that both electronics are identical and uncorrelated. The detector absolute time resolution was found to be 368 ps.

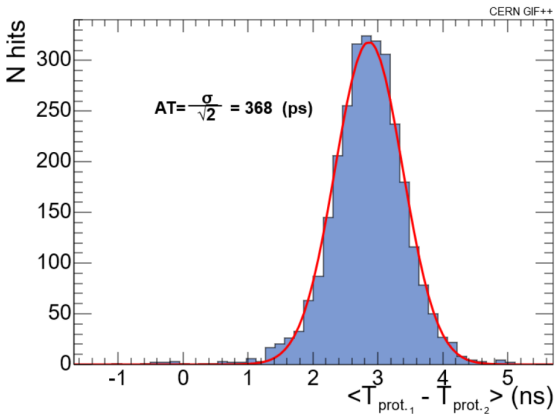

Figure 5.9: Distribution of the time differences of two iRPC detectors. The mean value divided by square of 2 represents the absolute time resolution.

5.2 iRPC sensitivity study and background rate estimation at HL-LHC

The estimation of the expected radiation level during HL-LHC is important to determine the detector performance and longevity. To estimate the expected background rate, the iRPC sensitivity has been studied using Monte Carlo simulation methods. The sensitivity (S) represents the detector response to the background particles, and is defined as the probability for an incident particle (ϕ) at a given energy, reaching the detector surface, to produce a signal (r):

$$S(E) = \frac{r}{\phi}(E) \tag{5.4}$$

The sensitivity is dependent on the detector geometry, and it is a function of the type of the incoming particles and their energy, indeed for different particles with different energies, different processes are responsible for the production of secondary particles.

The iRPC sensitivity has been studied first of all with respect to the gamma background at GIF++, comparing the simulation and the experimental results in order to validate the simulation. Finally, the iRPC sensitivity has been studied with respect to the different particles that constitute the background in CMS, at the energy spectrum expected at HL-LHC, allowing the estimation of the expected background rate [86].

5.2.1 iRPC sensitivity study at GIF++

GEANT toolkit has been used to describe and simulate the iRPC geometry, and then to study the detector sensitivity [87–90]. GEANT is a platform for the simulation of the passage of particles through matter using Monte Carlo methods. For this study "Geant4.9.6" version has been used. The "FTFP-BERT-HP" physics list package has been used to describe the physics processes, since it includes all the standard electromagnetic processes and it is the most accurate neutron model, especially at low energies.

The detector geometry described in the GEANT simulation corresponds to a large size trapezoidal iRPC prototype ($height$ = 1613 mm , $long\ side$ = 866.3 mm,

Table 5.1: iRPC geometry implemented in GEANT simulation. Each detector material layer, with its corresponding density and thickness, is reported up to the strip panel placed between the two gaps, then the geometry is repeated for the second gap.

Detector component	Material	Density $[g/cm^3]$	Thickness $[mm]$
Honeycomb panel	Aluminium	2.69	0.5
Honeycomb panel	Aluminium core	0.5	5
Honeycomb panel	Aluminium	2.69	0.5
Isolation material	Polyethylene	1.37	0.188
Isolation material	Cellulose	0.3	1
Faraday cage	Copper	8.96	0.38
Isolation material	Polyethylene	1.37	0.376
Isolation material	Ethylene-vinyl acetate	0.934	0.15
Gap I	Graphite	1.7	0.001
Gap I	HPL	1.4	1,350
Gap I	Gas gap	3,569	1,400
Gap I	HPL	1.4	1,350
Gap I	Graphite	1.7	0.001
Isolation material	Ethylene-vinyl acetate	0.934	0.15
Isolation material	Polyethylene	1.37	0.376
Strip panel	Copper	8.96	0.17

short side = 584.1 mm) that has been tested at GIF++. In order to properly include the secondary radiation produced by high energy particles, all the materials layers composing the detector were implemented in the simulation code. The detailed iRPC geometry is described in Table 5.1. Each material layer, with its corresponding density and thickness, is reported up to the strip panel placed between the two gaps, then the geometry is repeated for the second gap. The simulated iRPC geometry has been implemented in the simulated GIF++ geometry, at the same position where the iRPC prototype has been tested [91]. All others setup present inside the GIF++ bunker have also been included in the simulation, in order to reproduce as best as possible the background rate from scattering events.

The sensitivity calculation was done using Formula 5.4, where the ϕ represents the number of incident gammas on the detector surface, while r represents the simulated detector rate. If a charged particle reaches the gas gap is assumed to generate a signal. If more than one charged particle per event reaches the gas gap, only the first one is considered. To obtain a statistical uncertainty less than 10^{-3}, and according to the CPU computing time, a large numbers of events (8×10^8 for each ASB value) have been simulated. The number of simulated events have been normalized at the GIF++ source activity (14 TBq) for the comparison.

To validate the iRPC geometry simulation, the detector cluster rate has been experimentally measured at GIF++ at different ABS. The experimental cluster rate is used for the comparison with the simulated rate since the avalanche multiplication in the gas is not simulated. In Figure 5.10 (left), the detector cluster rate at working point experimentally measured (red curve) at GIF++ at different ABS is compared with the simulated rate (black curve). A factor ≈ 2 difference between the two curves is observed. An energy threshold was applied to the simulated primary and secondary charged particles which produce the signal in the gas gaps, in order to simulate the threshold used for the experimental measurements (300 $\mu V \approx 50\ fC$, see chapter 5.1.1). The energy thresholds of 100 and 200 keV (green and blue curves), applied to the charged particles, are the one that better match the experimental data, as shown in the plot. The 100 keV threshold guarantees a good agreement between experimental and simulated results, with a maximum discrepancy of $\approx 30\%$ in the worst case, and it has been chosen in order to not underestimate the rate.

Likewise, Figure 5.10 (right) shows the detector gamma sensitivity comparison between experimental data and simulated data, including the curves with the applied charged particles energy thresholds. For the experimental sensitivity calculation, the measured cluster rate at the numerator is used, while the simulated incident gamma rate as denominator is used. The good agreement between simulated and experimental

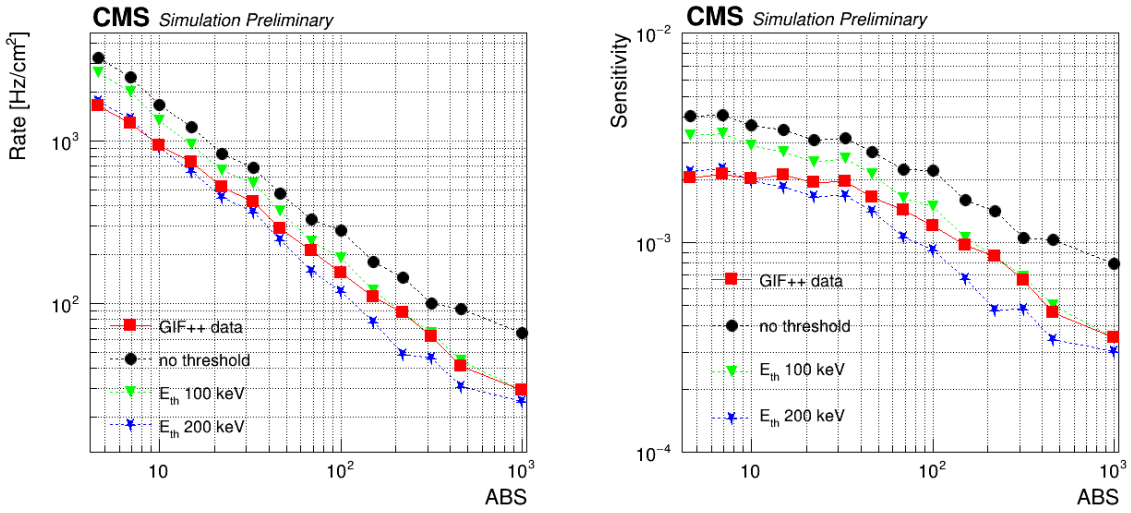

Figure 5.10: Rate (right) and sensitivity (left) measurements at different background conditions (ABS). The plots show the comparison between experimental data from GIF++ (red squares) and simulated data: without charged particles energy threshold (black) and with charged particles energy thresholds of 100 keV (green) and 200 keV (blue).

results allowed to validate the simulated iRPC geometry, and use it for the iRPC background rate estimation at HL-LHC.

Additionally, the simulation also allowed to determine the position where the primary electrons interact ionizing in the gas gaps, and the position where they have been produced. Figure 5.11 (left) represents the distribution of the position along the detector thickness (Z direction), for both gas gaps, where the primary electrons are produced after the interaction of the incident gammas with the detector materials (HPL gap-1 = red and HPL gap-2 = blue), and where the electrons ionize in the gas gap (gas gap-1 = green and gas gap-2 = yellow). For both gaps, most of the primary electrons are generated in the right HPL plate because the gamma flux direction, indeed the detector was located in front of the source. The other few remaining electrons are generated by photons coming from the back of the detector, produced by backscattering with the walls. More than 75% of the primary electrons are produced in the last $\approx 400\ \mu m$ of the 1.4 mm HPL plate. Electrons produced far from the gas gap are absorbed by the material layers. The gamma sensitivity of the two single gaps is the same, indeed the total number of electrons detected by the two gas gap is approximately the same.

Finally, the simulation of the full GIF++ geometry also allowed to characterize the gamma flux. The expected uniform incident gammas distribution over the detector surface, provided by the source collimator and lens, was confirmed. The photons kinetic energy distribution of the gammas was measured, and reported in Figure 5.11 (right). The distributions correspond to different source ABS. The nominal kinetic energy of the photons, produced by the Cs-137 source decay, is 662 keV, but back-scattered photons produce by the interactions with the materials present in the GIF++ bunker, mainly lead (irradiator, filters), steel (filters, floor), aluminium (filters) and concrete (surrounding bunker enclosure), generate a low energy component of degraded photons. For the available photons' energies of 662 keV or below, the main processes involved are Compton scattering and photoelectric effect. From the plot is evident that at high absorption factors the photons energy degradation is larger and the number of photons having the nominal energy values decrease.

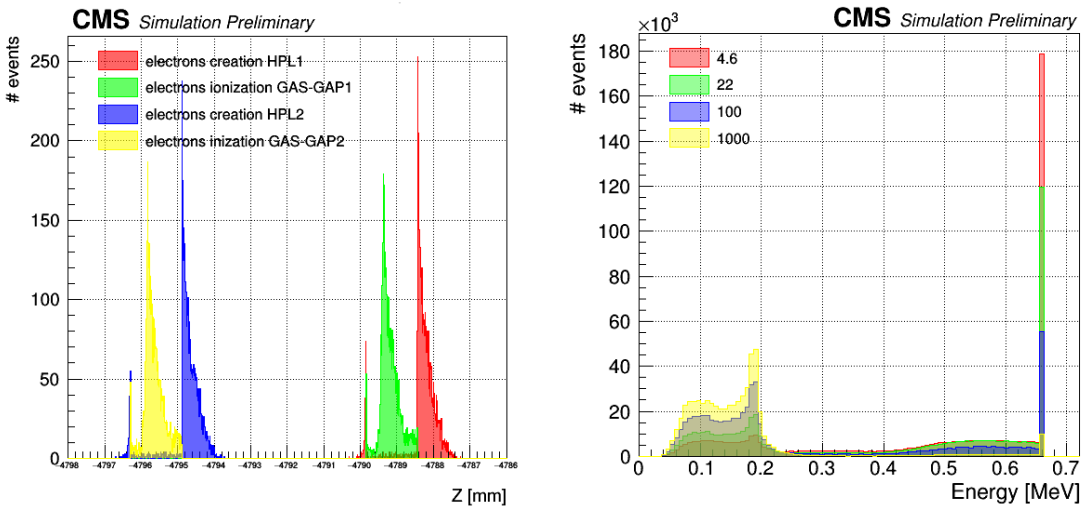

Figure 5.11: Left: distribution of the position along the detector thickness (Z direction), for both gas gaps, where the primary electrons are produced after the interaction of the incident gammas with the detector materials (HPL gap-1 = red and HPL gap-2 = blue), and where the electrons ionize in the gas gap (gas gap-1 = green and gas gap-2 = yellow). Right: GIF++ gamma energy distribution applying different source filters (ABS). The number of events for each ABS has been normalized.

5.2.2 Background rate study for the iRPC at HL-LHC

After the validation of the iRPC simulation at GIF++, the detector sensitivity was studied with respect to the different particles that compose the CMS background at the expected HL-LHC spectra. The main sources of background in the CMS muon system are:

- Neutrons produced in the wake of hadronic showers.
- Photons produced in de-excitation of nuclei. The nuclei excitation is produced via capture of low energy neutrons.
- Photons interactions may produce Compton electrons and electrons/positrons via pair production.

Figure 5.12 shows the particles rate fluxes, for neutrons, gammas and charged particles, as a function of the energy of the incoming particles, expected during HL-LHC in the endcap RE3/1 (left) and RE4/1 (right) stations. The incident background fluxes were estimated starting from "PYTHIA", used to simulate the proton-proton collisions [92]. The nominal HL-LHC conditions have been assumed as: energy of 14 TeV,

instantaneous luminosity of $5 \times 10^{34}\ cm^{-2}s^{-1}$, and pile up 200. The incident fluxes for the different background particles have been estimated with FLUKA, used to describe the upgraded CMS geometry (CMS Fluka study version v.3.7.7.0) and to propagate particles through the detector and surrounding material, cavern, etc [45, 93–95].

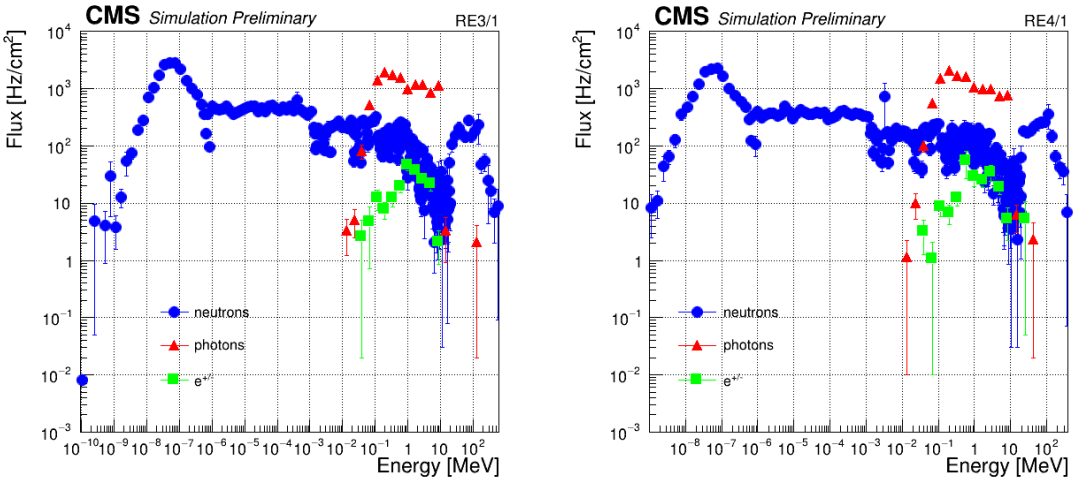

Figure 5.12: FLUKA Monte Carlo simulation of the particles rate flux (neutrons, gammas and charged particles) as a function of the energy of the incoming particles, expected during HL-LHC (14 TeV and $5 \times 10^{34}\ cm^{-2}s^{-1}$) in the endcap RE3/1 (left) and RE4/1 (right) stations.

Afterwards, the iRPC sensitivity has been estimated with respect to the different background particles (neutrons, gammas, electrons and positrons)using GEANT, and the following assumptions have been applied [86, 96]:

- The particle source is isotropic and particles randomly strike the detector.
- An energy threshold of 100 keV has been applied to the primary and secondary charged particles that produce signal in the gas gaps, to simulate the detector electronics threshold. The realistic threshold value of 100 keV was empirically obtained from the iRPC geometry validation study, comparing the measured gamma rate at GIF++ and the simulated rate (see section 5.2.1).
- If more than one charged particles reach the gas gap, only the first one is assumed to generate a signal.

In order to obtain a statistical uncertainty less than 10^{-4}, a large numbers of events (3×10^6 for each particle energy value) have been simulated. The estimation of the sensitivity variance is given by the binomial distribution.

The results are shown in Figure 5.2.2 (left), where the iRPC sensitivity is reported as a function of the energy of the incoming particles.

The gamma sensitivity values rise at the high energy region. Indeed, at low gammas energy, the produced secondary charged particles have not enough energy to reach the gas volume. The contribution from different processes to the gamma sensitivity has been studied and the result is reported in Figure 5.13 (right). As expected the dominant contribution is due to the Compton effect up to energies of few MeV, while at higher energies (greater than $10MeV$) the dominant process is the pair production. Photoelectric contribution is relevant only at very low energies.

The neutron sensitivity values rise at the low energy region ($E_n < 10^{-5}\ MeV$), which is mostly due to gammas coming from the (n, γ) capture reaction, whose cross section increases with decreasing in neutron energy as $\sigma \propto 1/\sqrt{E_n}$. At higher energies ($E_n > 1\ MeV$), the neutron sensitivity rises rapidly as a consequence of protons produced by elastic scattering on Hydrogen and by (n, p) reactions with Carbon, Oxygen and Aluminium.

For the neutron sensitivity is observed the main impact of the applied 100 keV energy threshold ($\approx 17\%$ lower), especially at the energy region $10^{-4} < E < 1\ MeV$. For the gammas particles the difference is $\approx 4\%$, and for electrons and positrons $\approx 6\%$. In total the applied threshold decreases the average detector sensitivity of $\approx 10\%$. Figure 5.14 (left) shows the expected background rate (r) in RE3/1 station as a function of the incident particles energy, estimated from the convolution of the incident particles fluxes (ϕ) and the sensitivities (S), using Formula 5.5.

$$r = \phi \times S \tag{5.5}$$

Figure 5.14 (right) shows the contribution of the different particles to the total background rate in the RE3/1 station as a function of the distance from the centre of the CMS beam pipe. Finally, the average background rate has been estimated using the average sensitivity values, [n (0.4%), γ (2.4%), $e^{-/+}$ (6.8%)]. The average background rate of $\approx 600\ Hz/cm^2$ defines the requirement of a minimum rate capability of $\approx 2\ kHz/cm^2$ for the iRPCs, when considering a safety factor of three. The same estimation was done for the RE4/1 station, where the particles flux is slightly lower,

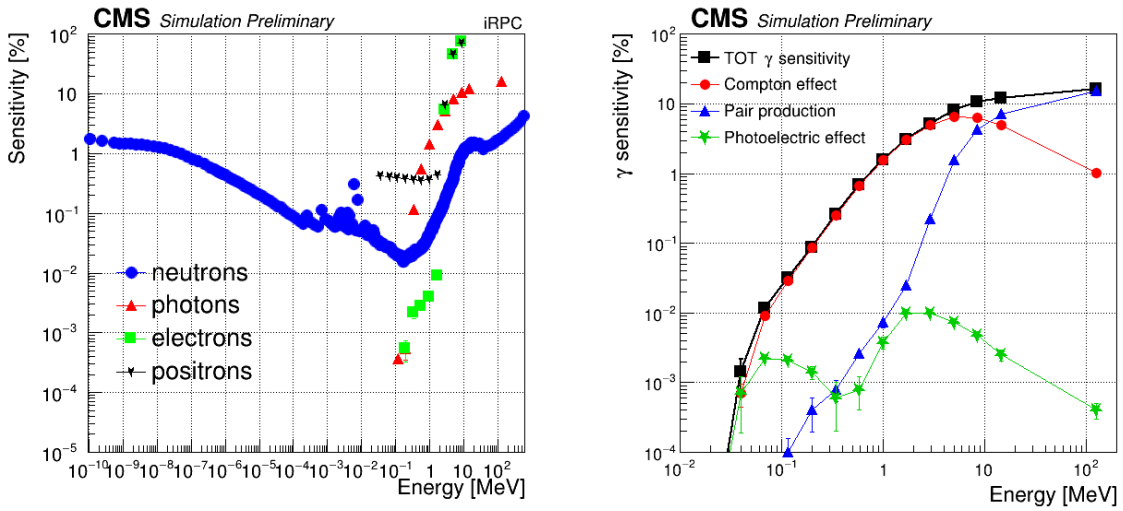

Figure 5.13: Left: Monte Carlo estimation of the iRPC sensitivity with respect to the different background particles (neutrons, photons, electrons and positrons) as a function of the kinetic energy of the incident particles. Right: contribution from the different processes to the detector gamma sensitivity (black) as a function of the gammas kinetic energy: Compton (red), pair production (blue) and photoelectric (green).

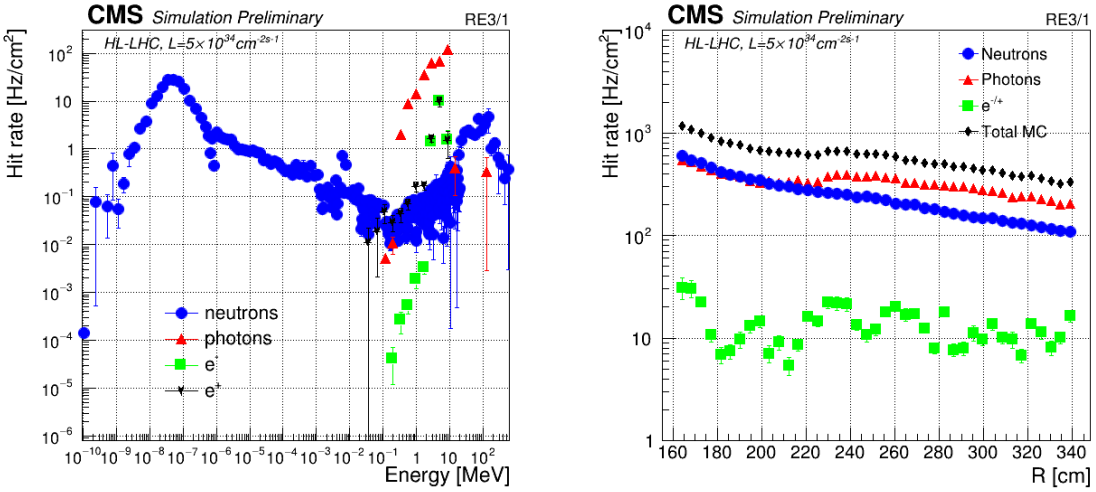

Figure 5.14: Monte Carlo simulation of the background rate expected in the endcap RE3/1 station during HL-LHC, as a function of the incoming particles energy (left) and as a function of the distance (R) from the centre of the CMS beam pipe (right). The contribution of the different particles is reported.

and the estimated background rate is $\approx 1.5\ kHz/cm^2$.

5.3 iRPC longevity studies

Possible aging effects of the iRPC system must be taken into account, as for the present system, and the detector longevity has to be validated for the entire HL-LHC program.

Unlike the present system, for the iRPC was not possible to extrapolate the expected integrated charge (Q_{iRPC}) at the end of HL-LHC, therefore it was calculated using Formula 5.6:

$$Q_{iRPC} = \langle q \rangle \times r \times T_{eff} \tag{5.6}$$

Where $\langle q \rangle = 9\ pC$ is the average charge per avalanche, $r = 2\ kHz/cm^2$ is the expected background rate, and $T_{eff} = 6 \times 10^7\ s$ is the effective operation time at the nominal instantaneous luminosity during the 10 years of HL-LHC. The result from Formula 5.6 is $\approx 1\ C/cm^2$, for which the iRPC must be certified. As expected, the iRPC estimated integrated charge is very similar to that estimated for the present system, indeed the iRPC expected background rate is $\approx$ 3 times greater then that RPC (2 kHz/cm^2 instead of 600 Hz/cm^2), but the average charge per avalanche is $\approx$ 3 times smaller (9 pC instead of 27 pC).

The longevity test procedure adopted for the iRPC is the same followed also for the present system (see chapter 4.3). The iRPC longevity test campaign is performed at GIF++, where a large size chamber (iRPC prototype-1) has been tested up to $\approx 90\ mC/cm^2$, and a second chamber (iRPC prototype-2) is still under irradiation, and currently has accumulated $\approx 100\ mC/cm^2$. The parameters and performance monitoring are reported in the following sections.

5.3.1 Detector parameters and performance monitoring

The iRPC prototype-1, that was used to test and validate the iRPC technology (section 5.1.1), has been then irradiated for the longevity study. The chamber operated at $\approx 2\ kHz/cm^2$ at working point $\approx 7.2\ kV$, up to having collected $\approx 90\ mC/cm^2$.

Figure 5.15 shows the detector dark current monitored during the periods when the GIF++ source was off. The top plot shows the full dark current curves measured at different integrated charge stages. The bottom plots show the dark current and noise rate monitoring versus the integrated charge, measured at 5 kV (left), and at working point voltage $\approx 7\ kV$ (right).

From the results is evident the dark current increase, observed already just after

the beginning of the irradiation. The ohmic current increases almost linearly, as it is very clear in the top plot. The contribution to the dark current rise came mostly from the Bottom gap layer, which was connected in series to the Top gap layer.

In order to try to mitigate the dark current increase, the gas connections were swapped between Top and Bottom layers, and at $\approx$ 70 mC/cm^2 the gas flow was increased from 1.5 to 5 gas volume exchanges per hour, but without any improvement. It was even tried to stop the irradiation for $\approx$ 2 months and just flushing the detector, but when the detector was turned on the current level was almost the same. The dark current constantly increased, up to reach values of 70 μA.

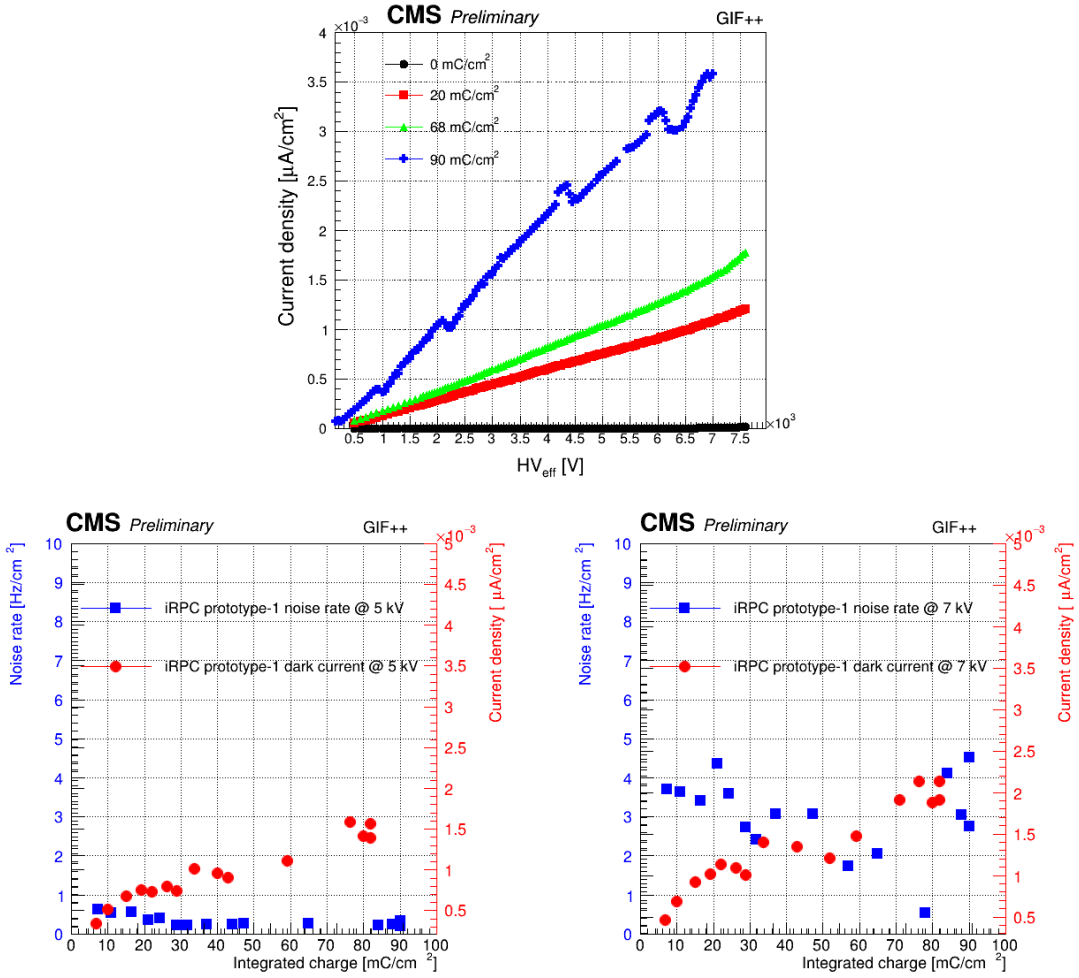

Figure 5.15: Top: iRPC prototype-1 dark currents curves at different integrated charge values. Bottom: iRPC prototype-1 dark currents (red) and noise rate (blue) monitoring versus integrated charge, at 5 kV (left), and at 7 kV (right).

The detector performance has been tested after having collected $\approx$ 90 mC/cm^2 and compared with that measured before the irradiation test. The dark current effects

caused a significant decrease of the rate capability (left plot), and a working point increase (right plot), as reported in Figure 5.16.

Due to the impossibility to run the detector with a so high dark current and unstable conditions, it was decided to stop the irradiation test and to open the gas gaps to investigate the problem. The results of the inner gap surface analysis are reported in section 5.3.2.

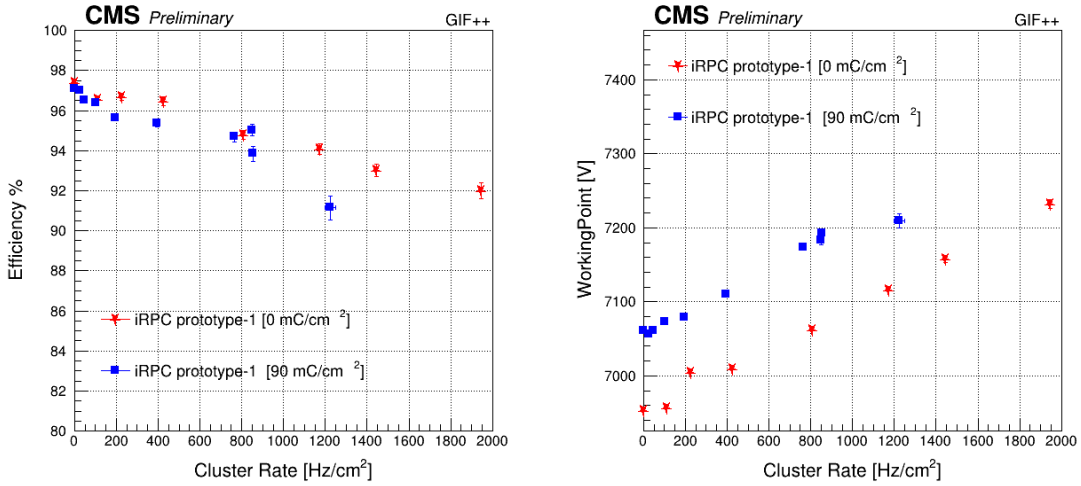

Figure 5.16: iRPC prototype-1 efficiency (left) and working point (right) as a function of the gamma background cluster rate. The measurements have been performed before the longevity test, and after having collected $\approx 90\ mC/cm^2$.

A second large size chamber, iRPC prototype-2, is under irradiation at GIF++, at $\approx 2\ kHz/cm^2$ at working point 7.2 kV, operating with ≈ 3 gas volume exchanges per hour, and following the same irradiation procedure as for iRPC prototype-1. Currently the integrated charge accumulated is $\approx 100\ mC/cm^2$.

Figure 5.17 shows the iRPC prototype-2 dark current. The left plot shows the full dark current curves measured at different integrated charge stages. The right plot shows the dark current monitoring versus the integrated charge, measured at 5 kV (blue), and at 7 kV (red).

The dark current remained almost stable and at low values at the beginning of the irradiation period. After 70 mC/cm^2 the dark current significantly increased, it was therefore decided to pause the irradiation and to lower the high voltage at 5 kV for around 1 month. This action allowed to reduce the dark current at similar values as before the increase. After the current decrease the chamber was irradiated for 1 month following a new procedure: operating at working point for 12 hours per day,

and at 5 kV for the rest 12 hours. During this period the dark current was stable in time, it was therefore decided to restart the standard irradiation procedure, but the dark current immediately increased almost linearly. Because of the high dark current value, it was decided to again irradiate the chamber for half day, and as before the dark current started to decrease.

The dark current evolution is under monitoring and the gas flow will be increased to try to mitigate the irradiation effect.

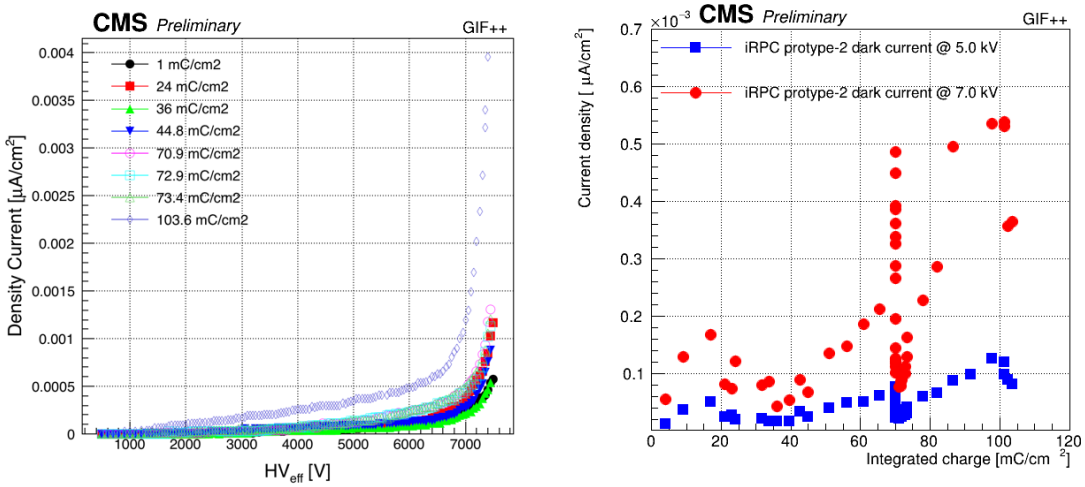

Figure 5.17: Left: dark current curves of iRPC prototype-2, at different integrated charge values. Right: dark current of iRPC prototype-2, monitored versus the integrated charge, at 5 kV (blue) and at the working point voltage ≈ 7 kV (red).

5.3.2 HPL surface analysis

As reported in the previous paragraphs, the irradiation of the iRPC prototype-1 was forced to be stopped due to the detector instability and very high dark current, after having collected only ≈ 90 mC/cm^2. In order to investigate the origin of the problem, the detector gaps have been opened and several analysis have been performed.

At the visual inspection the inner gaps surface presents sticky white matt spots nearby the spacers and the edges, as shown by Figure 5.18 (left). The spots seem to be drops of liquid, probably linseed oil not well polymerized, and they follow a preferential direction given by gravity. Both anode and cathode present the same configuration without any significant differences.

The comparison between the two images reported in Figure 5.18, makes evident

the different inner surface between the problematic irradiated iRPC prototype-1 (left) and the typical CMS RPC (right), which on contrary is uniform and does not present any evident defects.

A not irradiated iRPC gap, produced in the same bunch, was opened and the inner surface shown the same structure as the irradiated one, with the only difference that the drops of liquid presented a brightness color instead of being white. Therefore, the surface defects are due to a production problems, and the effect is made more visible by the irradiation.

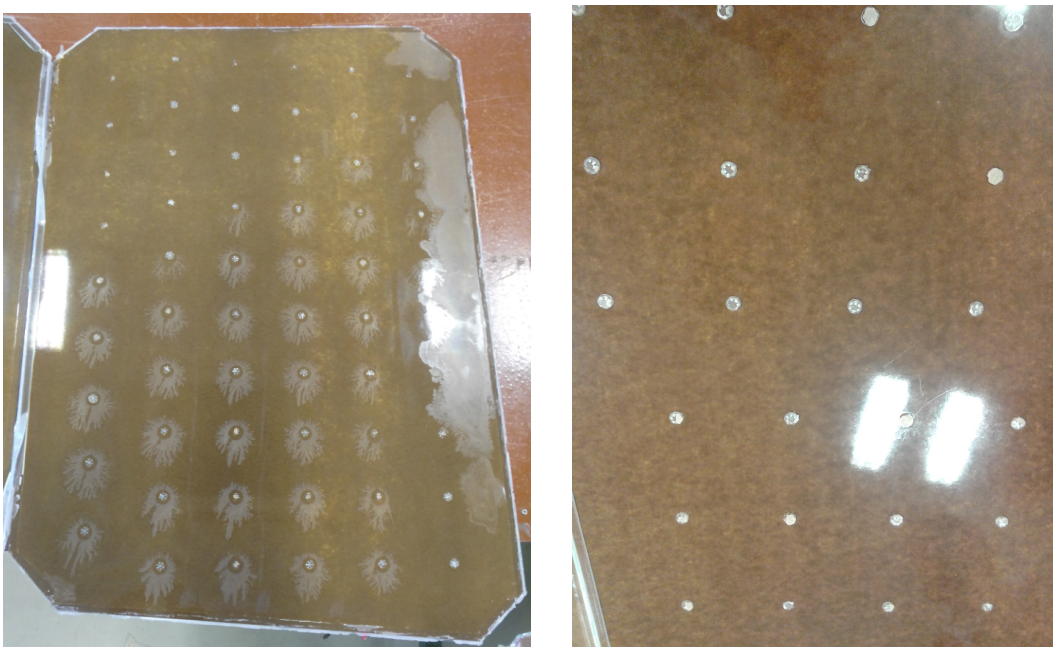

Figure 5.18: Pictures of the iRPC prototype-1 inner surface after the irradiation (left), and the typical inner surface of a standard CMS RPC chamber (right).

A more accurate inspections were done using the Scanning Electron Microscope (SEM) technique[1] at CERN Mechanical and Engineering department [97]. The SEM better shows the white matt spot nearby the spacer, which appears darker in Figure 5.19 (left) due to the surface variation effect. The SEM also underline a ring-shaped area, $\approx 5\ mm$ just around the spacer.

The surface characteristics at the non-affected area, far from the spacers, and at the white matt area, was compared by SEM imaging, presenting the first one a smooth

[1]The Scanning Electron Microscope (SEM) produces images by scanning the sample with a high-energy electrons beam. As the electrons interact with the sample, they produce secondary electrons, backscattered electrons, and characteristic X-rays. These signals are collected by one or more detectors to form images which are then displayed.

aspect while the second one shows a rough and not uniform topography, as shown by Figure 5.19 (right).

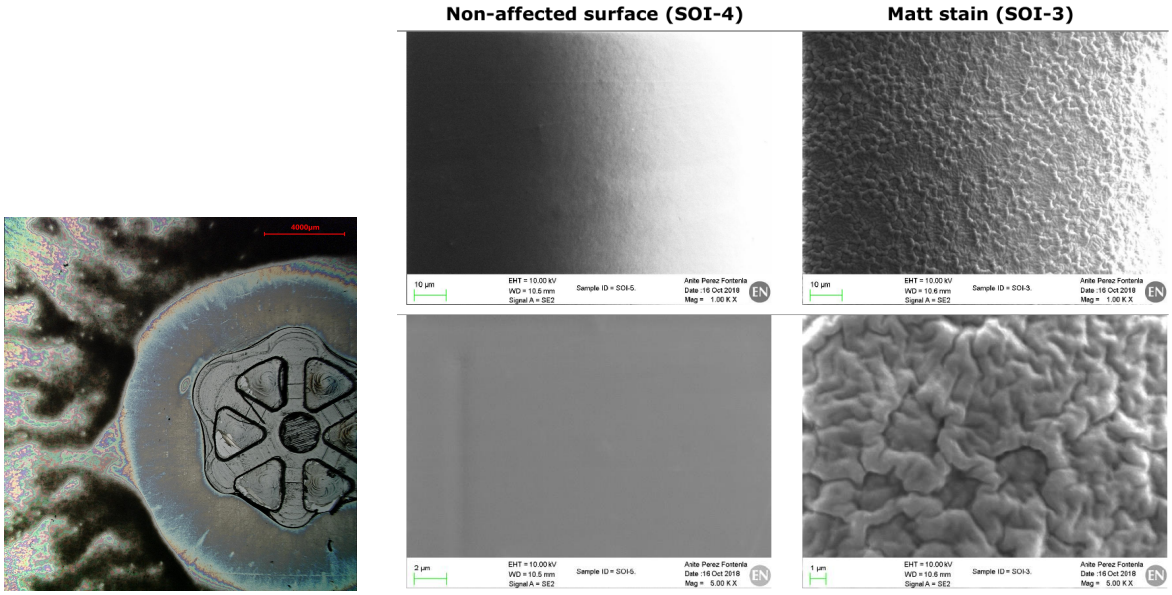

Figure 5.19: Left: SEM image of the iRPC prototype-1 area around a spacer. Right: SEM images of the iRPC prototype-1 surface at the non-affected area (left), and the matt stain area (right), at magnification 1 kx (top) and 5 kx (bottom).

The inner gap surface profile was measured using the Vertical Scanning Interferometry (VSI) technique[2] [98]. Many samples have been analysed in different areas, and a representative result is reported in Figure 5.20 (left). The analysed area is within the black marker drawn on the sample, around $1.5 \times 5.5\ mm$. The profile topography of the sample is reported in the center plot. The measurements represent the relative surface height with respect to an arbitrary reference point, chosen in the not-affected area.

The left region (in yellow/green, for $\approx$ 12 mm in length), represents the not affected area far from the spacer, which results uniform confirming the SEM measurements. This area was used as a reference point for the measurements, and it is at $\approx 0\ \mu m$ level. Next (in blue, for $\approx$ 15 mm in length), there is a lower height region , $\approx -4\ \mu m$, that gradually increase up to reach the highest region $\approx 10\ \mu m$ (in red, for $\approx$ 20 mm in length). The higher height region, in turn gradually decrease, reaching again a low height area $\approx -4\ \mu m$, near to the spacer (in blue, for $\approx 5\ mm$ in length).

[2]Vertical Scanning Interferometry (VSI) technique uses the basic interferometric principles: light reflected from a reference mirror combines with light reflected from a sample to produce interference fringes, where the best-contrast fringe occurs at best focus [98].

The profile evolution, along the sample length, is reported in the right plot. It is possible to spot the difference in height between the different areas, proving the not-uniform surface.

These results confirm the hypothesis of the not polymerized linseed oil accumulation in the corresponding white matt stain. Additionally, they spotted areas with lack of oil.

The same kind of analysis was performed on not-irradiated iRPC samples, showing the same results, confirming the production problem.

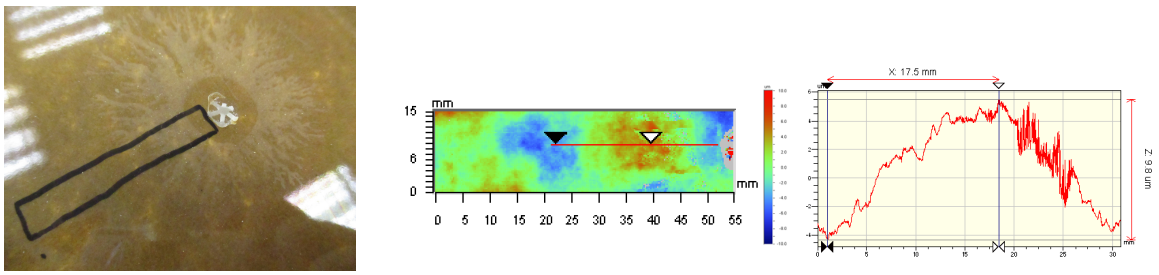

Figure 5.20: Left: picture of the iRPC prototype-1 gap sample used for the Vertical Scanning Interferometry (VSI) analysis. Center: VSI topography of the analysed sample. Right: VSI profile along the red line drawn in the 2-D map.

The chemical composition of the surface was studied using the Energy Dispersive X-ray Spectrometer (EDS/X-ray)[3], in order to exclude possible chemical contaminations [99].

The analysis was performed in 4 sites of interest (SOI) of the irradiated iRPC prototype-1 sample, as reported in Figure 5.21 (top): the spacer/glue area, the ring-shaped area, the white matt stain around the spacer, and the not-affected area far from the spacer. The chemical analysis results are reported in Figure 5.21 (bottom-left).

The EDS analysis in the HPL areas, showed that the composition is rich in Carbon (C), Oxygen (O), and Nitrogen (N). The presence of C and O is well aligned with the composition of the linseed oil and the internal HPL layers made of phenolic resin, while C, O, and N are characteristics of the external HPL layer made of melamine resin [100].

[3]Energy Dispersive X-ray Spectrometer (EDS/X-ray) is a technique that enables to analyse the elemental composition of a sample. The operating principle is based on the capacity of high energy electromagnetic radiation (X-rays) to eject "core" electrons from an atom. Removing these electrons from the system will leave behind a hole that a higher energy electron can fill in, and it will release energy as it relaxes. The energy released during this relaxation process is unique to each element, and as such bombarding a sample with X-rays can be used to identify what elements are present, as well as what proportion they are present in. This principle is known as Moseley's Law.

The results are in agreement with the expected chemical elements, indeed the cross check analysis was performed on the single materials. The liquid linseed oil analysis reported the detection of only C and O, while the analysis of a not-oiled HPL sample reported the C, O, and N presence. The glue composition was determined analysing the pure material and that one in SOI-1, since the remaining volume was thick enough to avoid any influence of the layers below. In both cases only C and O were detected [101].

Additionally, few samples of not-irradiated detectors were analysed, and the same elements were detected, a part the Fluorine (F). Fluorine presence was detected in a small quantity in all SOI of the irradiated sample, proving the formation under the irradiation conditions. Nevertheless, the small detected quantity exclude the Fluorine deposit as the reason of the gaps problems, moreover a similar quantity was detected in samples of irradiated RPC that did not present any operational problem.

With EDS/X-ray technique, the presence of some characteristic elements of the samples (like hydrogen) cannot be detected, and the quantification is less precise for low amount of elements with atomic number between 4 and 11, that includes some of the key elements present in the HPL and linseed oil, like C, N and O. Nevertheless, the measurements have been repeated in many samples, considering both anode and cathode sides, and all of them were in agreement to confirm the reported results.

The EDS/X-ray measurements have not detected any evidence of contaminations, however, an interesting distribution of the Nitrogen was observed. The external HPL layers are made of melamine resin, which is the only gap material that contains Nitrogen. In SOI-1 the thick glue layer does not allows the N detection, since the penetration depth of the EDS at 20 keV was estimated in approximately 1.5 $\mu\ m$ for a bulk carbon sample. The Nitrogen presence is not detected in SOI-3 as well, that could indicate, as supposed, a thicker oil layer that does not allows the X-ray to reach the melamine layer. Finally, N is instead detected in SOI-2 and SOI-4, that could indicate a thinner oil layer.

Figure 5.21 (bottom-right) shows the Nitrogen detected in SOI-2 and SOI-3 regions, measured in three different samples. The iRCP sample shows a very high N presence in the ring-shaped area SOI-2, comparable with the not-oiled sample, indicating a lack of oil. Assuming as a reference the standard RPCs, the comparison confirms

the hypothesis, indeed the N detected in that is less, indicating a much thicker oil layer.

Additionally, the comparison between the iRPC not affected area SOI-4 with any RPC area, indicate that the overall iRPC oil layer is thinner.

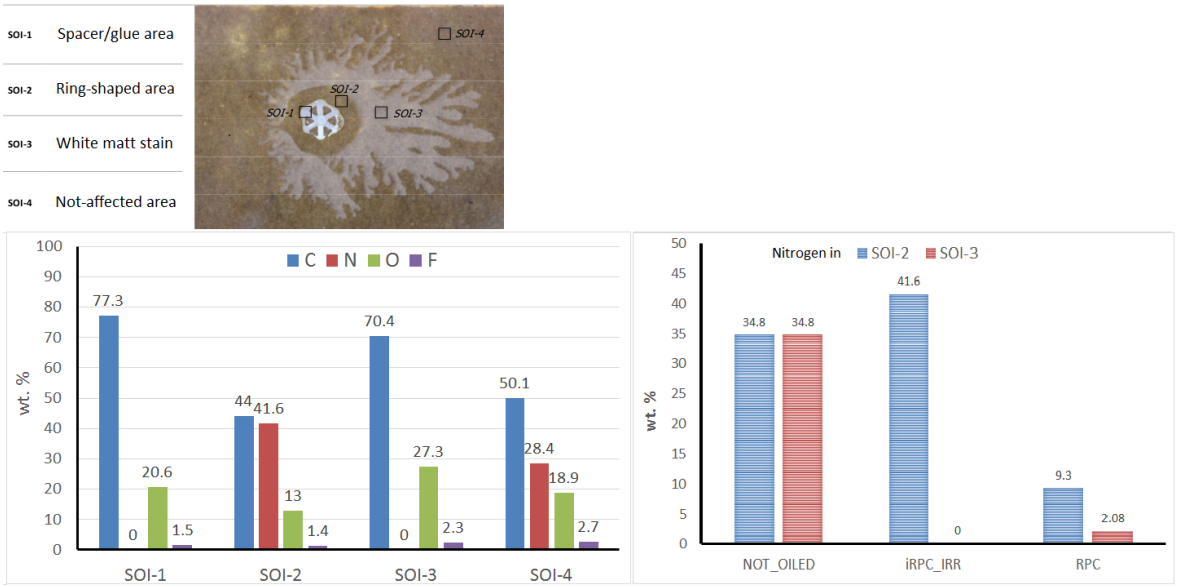

Figure 5.21: Left: Energy Dispersive X-ray Spectrometer (EDS/X-ray) of the iRPC prototype-1. The EDS analysis was performed in four sites of interest (SOI), and the chemical components in mass fraction are reported in the bottom left plot. The reported values correspond to the normalized weight percentage (wt.%) of the detected elements. Right: Nitrogen presence in the areas SOI-2 and SOI-3, measured with EDS technique in three different samples: not oiled iRPC, standard RPC, and iRPC prototype-1.

The hypothesis based on the EDS/X-ray results is in agreement with the measurements performed with VSI.

The surface analysis highlighted a production problem in the gaps oiling procedure, demonstrating the not uniform surface. The critical regions, where the oil layer is particularly inhomogeneous, have been identified: the area nearby the spacers and the edges present an accumulation of not polymerized linseed oil, while the ring-shaped area around the spacers presents a lack of oil.

To investigate the source of the oiling problem, all gap production aspects have been taken into account.

- HPL is produced by a different company with respect to the first RPC production (2005), but the same as for the second RPC production (2010 for the RE4 disks) for the Phase-I upgrade.

- HPL cleaning is done manually using Isopropyl alcohol instead to be mechanically brushed as for the previous productions.
- Spacers are made of the same material (polycarbonate) as the previous productions, same cylindrical shape including the thin external "lips", same diameter, but they have obviously different thickness, and also slightly bigger and different bounding area geometry [37].

The roughness of not-oiled iRPC HPL plate was measured with a tip probe, and compared with the standard RPC. An example of the roughness profile is reported in Figure 5.22 (left).

Roughness measurements of different HPL samples, cleaned with different methods, have been performed, both in longitudinal and transversal directions. The results reported in Figure 5.22 (right) show that the cleaning method does not affect the surface roughness. It is also evident that the iRPC HPL surface is improved with respect to that the standard RPC, since the average roughness value (R_a) is around a factor 2 smaller. On the other hand, it should be considered that the material wettability is enhanced by the roughness [102, 103].

The surface tension of the same samples was measured as well, and for all of them it was measured around $44.7 \pm 1.9\ mN/m$, without any significant difference between different HPL productions or different cleaning methods.

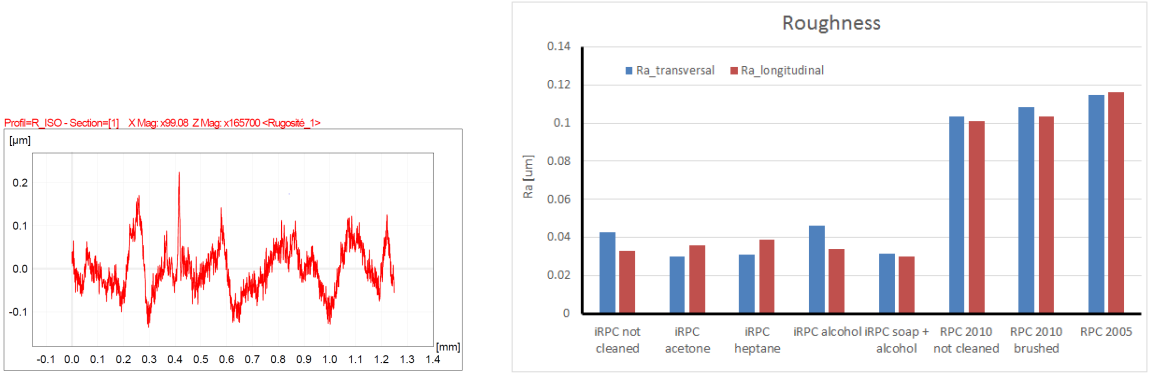

Figure 5.22: Left: roughness profile of a not oiled and not cleaned iRPC HPL sample, measured using a probe tip. Right: average roughness (R_a), measured in longitudinal and transversal directions, for different not oiled HPL samples, cleaned with different methods.

The oiling procedure has been reproduced immersing HPL plates with the glued spacers inside the linseed oil, in order to be able to observe the dynamics of the oil

distribution over the HPL plate and in particular near to the spacers and the edges.

The problem was successfully reproduced, and what was observed is that the oil is pushed away from the spacers, probably due to their low surface tension and helped by the improved HPL roughness. The effect seems to be amplified by the new spacers geometry and by the capillary effect. The oil is pushed away from the spacers creating the ring-shaped areas having a very thin oil layer, while it is accumulated around 5 mm far from the pacers. Additionally, some linseed oil remains trapped in the new bigger bonding area and in the pockets created under the spacers lips. In that positions, the airflow flushing during the dry procedure to polymerize the oil is less, therefore the oil slowly comes out creating drops traces on the surface.

In conclusion, the not-uniformity of the inner gaps surface are a production issue, and they are the cause of the observed dark current increase. In particular, the most critical problem is the not polymerized oil that can results in gas gap thickness variations and even electrical bridges between the HPL plates.

5.3.3 Oiling improvement test

The quality of the gap surface is crucial in reducing spontaneous discharges which might affect the rate capability of the chamber. The HPL surfaces facing the gas have, unavoidably, local non-uniformities at the microscopic level. Any small protruding point in the plates surface would provoke a much more intense local field, increasing the probability of local discharges. A better smoothness of the surface was achieved by coating the inner surfaces with a paint made of linseed oil (40%) diluted in heptane (60%). The treatment of the internal HPL surface is done by filling the entire gas volume of a fully assembled RPC with a mixture of linseed oil and heptane that is slowly taken away. A dry air flow blown for several hours ($\approx$ 96 h) through the emptied gas volume, at room temperature, ensures the polymerization of the oil. The resulting effect is the deposition of a thin layer ($\mathcal{O}$ (μ)) of polymerized oil on both the HPL surfaces facing the gas volume. This procedure assures a significant reduction in the noise rate. Additionally, the linseed oil layer protects the HPL surface against the possible deposition of pollutants created in the gas volume.

To enhance the gap oiling process, the procedure has been improved by increasing

the oil dry time up to 120 hours. Different oil coating methods are also under study. Few small iRPC prototypes (70×70 cm) have been build to test two different oiling procedure:

- Standard Single Oil coating (SO), using 40% linseed oil and 60% heptane mix.
- Double Oil coating (DO), using 35% linseed oil and 65% heptane mix. In between the 2 coatings, and at the end, the air is flushed for 60 hours in the gas gap to speed up the oil dry.

Many gaps, built with both procedures, have been opened and analysed. The inspection of the single oil gaps confirmed the results of the previous prototypes built and tested with the same procedure. The double oil coating showed an evident thicker oil layer, but the surface was even more irregular and not uniform, with more evident oil drop trace around the spacers and on the whole surface.

Three prototypes, 2 single oil (SO-1 and SO-2) and one double oil (DO-1), have been irradiated at GIF++ for short time, up to accumulate ≈ 45 mC/cm^2. The dark current monitoring at around the working point (≈ 7 kV) is reported in Figure 5.23 (left). The SO-1 prototype shown stable and low dark current for all the irradiation period. The dark current of the SO-2 prototype increased linearly already at the beginning of the irradiation, up to reach a very high level, $\approx 50\mu A$, and become very unstable generating continuously discharges. The DO-2 prototype shown an almost stable dark current at the beginning of the irradiation, up to when suddenly quickly increased, and it was not possible anymore to operate the detector due to the continuously discharges.

Figure 5.23 (right) shows the gap inner surface of the DO-2 prototype, after the irradiation.

The iRPC oiling test results were not satisfactory, they proved the problem with the standard coating procedure, and they showed that the double oil coating does not improves the surface quality.

Test to fine tune the oil parameters and the oiling procedure are ongoing. Encouraging preliminary results have been obtained with a more dense and viscose oil mix, 50-50% of linseed oil and heptane, and applying a “fast” double oiling, which foresee 2 coatings, but without dry time in between. Additionally, the spacers diameter has

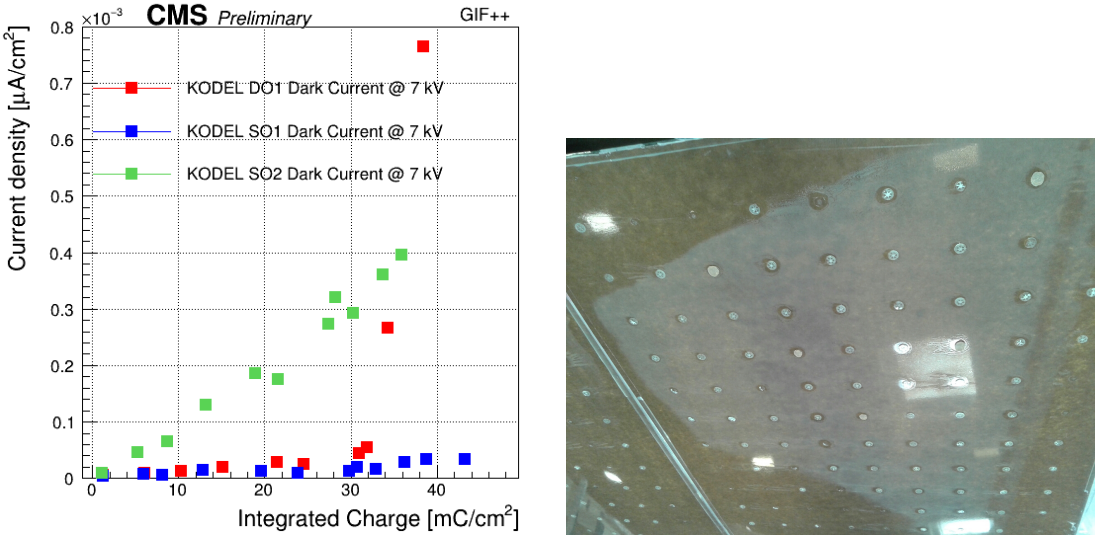

Figure 5.23: Left: dark current of the three irradiated small iRPC prototypes (Double-Oil-1 (DO-1), Single-Oil-1 (SO-1) and Single-Oil-2 (SO-2)), monitored as a function of the integrated charge. Right: picture of the inner gap surface of the Double Oil (DO-1) bottom gap.

been reduced from 12 to 10 mm, in order to reduce the pockets between the spacers and the plate, where the oil can be stuck. From visual inspection, the gap surface seems much more uniform, the defects around the spacers and the edges have been significantly reduced, and the oil thickness increased. Further improvements are still requested, and when the results will satisfy the quality controls, a new aging test will be performed.

6

Search for RPC eco-friendly gas mixture

The Global Warming Potential (GWP) of the present CMS RPC gas mixture is around 1400, mainly due to the $C_2H_2F_4$, which is the main RPC gas component (95.2%). The recent European regulation concerning the GHGs might have a significant impact on the $C_2H_2F_4$ availability and price because other alternative gases are already available for refrigeration systems. In a short-term scale, the SF_6 should be less affected since no valid alternative gases have been found yet.

The quest for a suitable eco-friendly replacement is a multi-parameter problem that has to take into account several aspects, flammability/toxicity/handling hazards, matching with available electronics and compatibility with the materials used in the muon detectors. For the present RPC system, important constraints have to be considered: the front-end electronics use a discriminator threshold corresponding to about 150 fC. Lowering this value would increase the electronic noise to unacceptable levels. Additionally, the high voltage boards are limited to 12 kV which is therefore the maximum possible operation voltage.

For these reasons, in the framework of the CMS RPC upgrade project for HL-LHC, an extensive R&D program was started at Ghent and LNF laboratories, in collaboration with the ATLAS-RPC group, in order to find a replacement for the $C_2H_2F_4$ and eventually for the SF_6. An overview of potential gas candidates can be found in Ref. [45, 104–106]. The most promising candidates to replace the $C_2H_2F_4$ are the fluorinated propene refrigerants called hydro-fluoro-olefins (HFOs)[1], which have a

[1]There are several isomers of HFO and the most commercially available are $HFO-1234yf$ (2,3,3,3-tetrafluoropropene) and $HFO-1234ze$ (1,3,3,3-tetrafluoropropene), with a GWP of 4 and 6 respectively.

GWP less than 6, and they are already used in industrial applications [107]. The HFOs contain the same amount of fluorine atoms as the $C_2H_2F_4$, and one carbon more.

The complete replacement $C_2H_2F_4$ with HFO as main gas component requires operation at much higher applied voltages, more than 13 kV. To overcome this problem, the addition of inert gas to lower the working point can be envisaged [108, 109]. About 40% or 50% of CO_2 is necessary to reach acceptable working point values, but the streamer probability stays higher than with the standard gas mixture. To overcome this issue, it is necessary to increase a bit the SF_6 concentration. Furthermore, even if the CO_2 is a quencher gas, it does not have the same effect on photons absorption as the iC_4H_{10}, which is therefore still needed.

Very interesting results were achieved by testing with cosmic rays a 2 mm wide single-gap RPC, using gas mixtures with different combinations of $HFO-1234ze$ and CO_2 [45]. Figure 6.1 (left) shows that increasing the fraction of $HFO-1234ze$ with respect to the CO_2 moves the working voltage to higher values but reduces the streamer probability. In all the tested mixtures, the plateau region with efficiency above 90% and with streamer probability below a few percent is narrowed with respect to the standard gas mixture. The most interesting gas mixture was composed of 45% of $HFO-1234ze$, 50% of CO_2, 4% of iC_4H_{10} and 1% of SF_6. The results in terms of efficiency and streamer probability were satisfactory, with a streamer probability below 10%, and a working voltage around 2 kV higher with respect to the standard CMS RPC mixture, just at the edge of the high voltage system limits.

An iRPC prototype has been tested as well, with a similar ecogas mixture [45]: 50% of $HFO-1234ze$, 45.2% of CO_2, 4.5% of iC_4H_{10} and 0.3% of SF_6. In Figure 6.1 (right), the efficiency and the cluster size are reported as a function of the effective high voltage for both standard and ecological gas mixture. The efficiency at working point is consistent for both gas mixtures, with a shift of ≈ 1.3 kV. Although an increase of the cluster size in the order of one strip was observed.

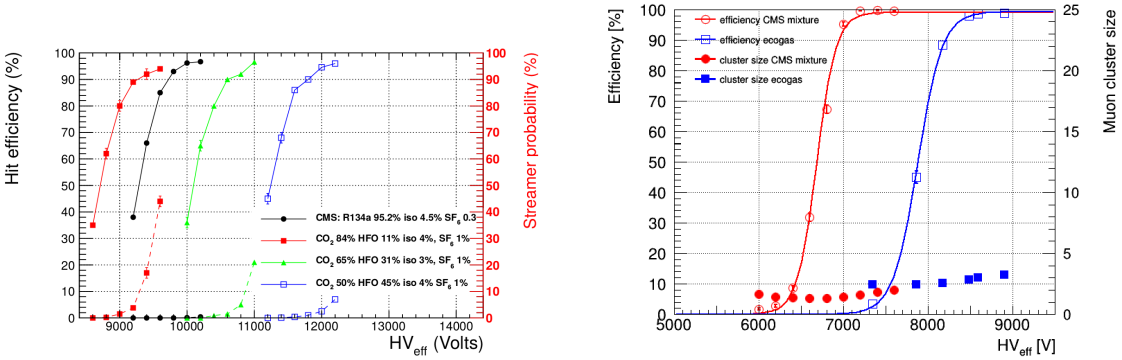

Figure 6.1: Left: RPC efficiency (solid line) and streamer probability (dashed line) as a function of the effective high voltage, measured for gas mixtures with different combinations of $HFO-1234ze$ and CO_2. Right: iRPC efficiency (empty markers) and cluster size (full markers) as a function of the effective high voltage, measured for standard mixture (red) and ecogas mixtures (blue) based on 50% of $HFO-1234ze$, 45.2% of CO_2, 4.5% of iC_4H_{10} and 0.3% of SF_6 [45].

6.1 Eco-friendly gas mixture characterization under irradiation at GIF++

Careful validation of the RPC performance in LHC-like conditions, using ecogas mixtures, has to be carried out at GIF++ to study the rate capability and the detector aging. In this context, a collaboration has been set up among the CMS, ATLAS, ALICE and CERN-EP-DT groups [110].

The experimental set up at GIF++ consists of 5 chambers: 3 single-gap RPCs having 2 mm gas gap and plates thickness (from ATLAS, ALICE and EP-DT), 1 double-gap RPC having 2 mm gas gap and plates thickness (from CMS) equipped with the standard CMS RPC FEB, 1 double-gap iRPC having 1.4 mm gas gap and plates thickness (from CMS). All the chambers operated with the selected ecogas mixture: 45% of $HFO-1234ze$, 50% of CO_2, 4% of iC_4H_{10} and 1% of SF_6.

The chambers have been tested at different gamma background conditions, and in Figure 6.2 the main parameters of the CMS RPC, such as current (left), rate (center) and charge (right), are reported as a function of the effective high voltage.

Because the CMS RPC chamber only was equipped with FEB, the background rate was studied via simulation using the same method described in chapter 5.2. The simulated background rate at different absorption factors is reported for all the 5 cham-

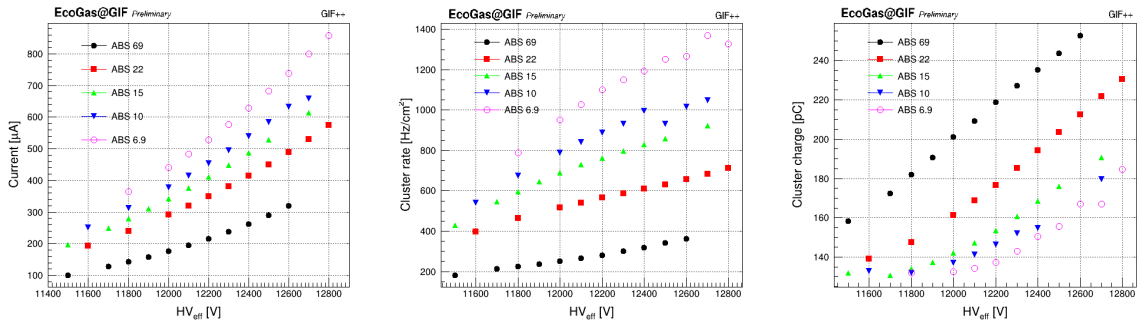

Figure 6.2: Currents (left), rate (center) and average avalanche charge (right) versus the effective high voltage, measured for the CMS RPC at different background conditions (ABS).

bers in Figure 6.3. The measured CMS RPC background rate at around the working point, estimated at the cluster rate plateau, is in a good agreement with the simulation results.

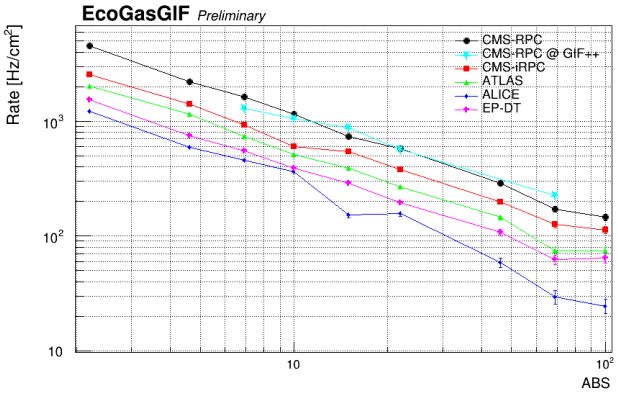

Figure 6.3: Simulated background rate for the 5 chambers under test, and the background rate measured at working point for the CMS RPC equipped with FEB, applying a 150 fC threshold.

The currents measured with the ecogas mixture were compared with those measured with the standard mixture, as reported in Figure 6.4. At the same background rate conditions, the results show a $\approx 2\ kV$ shift for the CMS RPC (left plot) when working with ecogas, and $\approx 1.2\ kV$ for the CMS-iRPC (right plot) when working with ecogas, in agreement with the results found in the previous R&D (see Figure 6.1).

For applications like LHC, where the detectors operate with high background rates, the avalanche charge should be kept low to benefit in terms of rate capability and aging. The low charge, around 27 pC at working point, was successfully obtained with the standard mixture. The average avalanche charge developed in RPC operating with the ecogas mixture was studied, and as reported in Figure 6.5 (left) it was found to

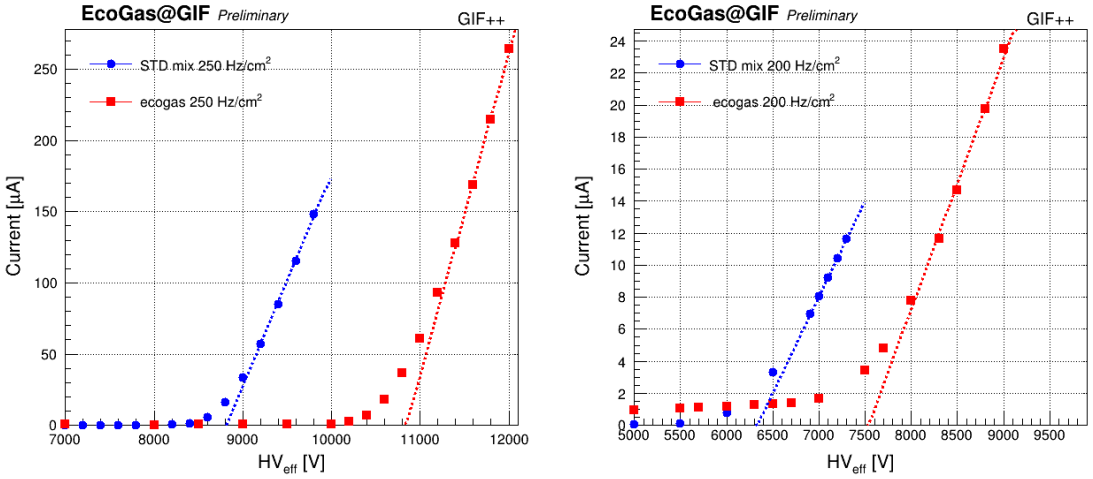

Figure 6.4: Currents versus the effective high voltage, measured in presence of gamma background with the standard gas mixture and with the ecogas mixture. Currents measurements performed for CMS RPC (left), and for CMS-iRPC (right).

be $\approx 150\ pC$ at the working point, around 5 times greater with respect to the standard mixture.

The average gamma cluster size has been studied as well, and as shown in Figure 6.5 (right) it was measured ≈ 2.6 strips at the working point for the ecogas mixture, while ≈ 1.8 strips with the standard mixture.

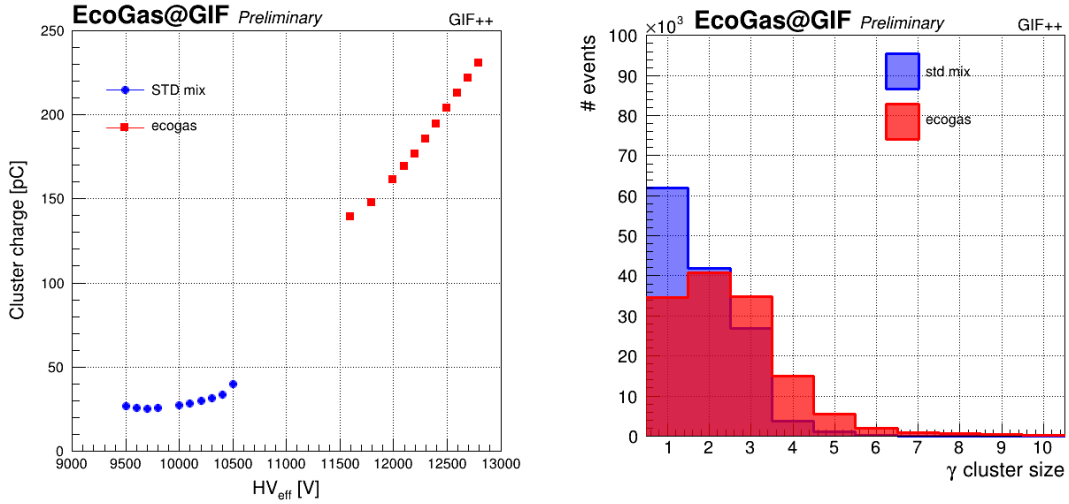

Figure 6.5: Left: CMS RPC average avalanche charge versus the effective high voltage, measured in presence of gamma background, using the standard gas mixture (blue) and using the ecogas mixture (red). Right: CMS RPC average gamma cluster size distribution measured using the standard gas mixture (blue) and using the ecogas mixture (red).

Detailed test are planned at GIF++ to study the detector performance using the ecogas mixture under high background rate.

6.2 Longevity test at GIF++ using eco-friendly gas mixture

The RPC materials compatibility with the ecogas mixtures was investigated [45]. The properties of materials used in the RPC detectors were compared before and after exposure to candidate ecogases in standard operating conditions. To expedite the aging process, materials samples were exposed to candidate gases in a pressurized detector. Preliminary results for RPC HPL samples exposed to $HFO-1234ze$ gas at 2 bar for 6 months do not show any difference in infrared spectrography analyses with respect to unused samples.

The detectors irradiation test has recently started at GIF++ to study the RPC longevity when operating with the ecogas mixture. All the five chambers have been irradiated at $\approx 800\ Hz/cm^2$ as gamma background rate measured at working point, operating with 1 gas volume exchange per hour. The chambers were connected in parallel to the gas line distribution. The longevity procedure is the same described in chapter 4.3. Currently, the collected integrated charge for each chamber is $\approx 5\ mC/cm^2$.

Figure 6.6 shows the dark current curves measured at different irradiation stages for the CMS RPC bottom (left) and top (right) gap. The dark current increased in all the chambers already after only one week of irradiation, and after two weeks the ohmic current was around 4 times higher than the initial one. It was therefore decided to stop the irradiation and just flush the chambers with fresh gas. The dark current keeps increasing for around 4 days, and then it started to decrease, up to reduce a factor ≈ 2 after two weeks. The irradiation was then restarted, and after 1 week the currents were already at the same level measured before the irradiation stop, or even higher in some gaps.

The dark current trend is more evident in Figure 6.7, where the CMS RPC dark current measured at 6 kV (left), which represent the ohmic contribution, and at 12 kV (right), which also includes the gas amplification, are reported as a function of the time. A clear linear trend of the dark current is visible during the irradiation period.

For all the chambers the dark current increase was observed, except in the CMS RPC top gap, for which the increase was much less severe, as shown in Figure 6.6

(right). The reason could be a possible gas effect, since the CMS RPC top gap was the first gap connected in the gas line with respect to the bottom gap. Nevertheless, the same effect was not observed neither in the CMS-iRPC double-gap, nor in the single-gap chambers. Moreover, after the first week of irradiation, the gas flow in the ATLAS chamber was increased from 1 to 3 gas volumes exchanges per hours, but no improving effects were observed.

Further investigation to mitigate the irradiation effect are ongoing.

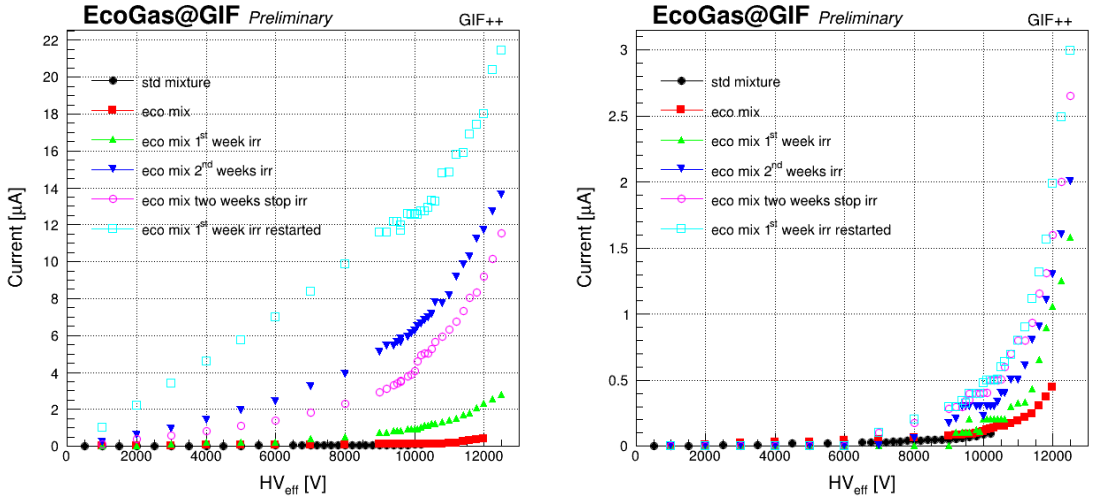

Figure 6.6: Dark currents curves for the CMS RPC bottom gap (left) and for the top gap (right), monitored at different period during the irradiation test at GIF++.

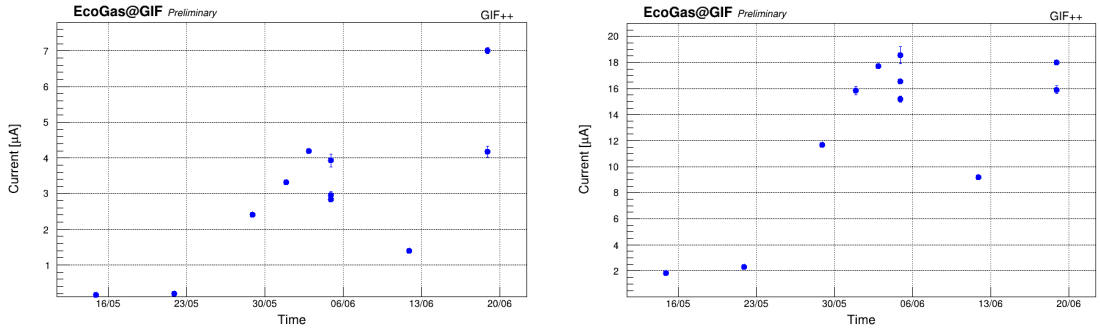

Figure 6.7: Dark currents of CMS RPC bottom gap monitored as a function of the time during the irradiation period at GIF++. The dark current was measured at 6 kV (left) and at 12 kV (right).

6.3 HF study using eco-friendly gas mixture

The HFO molecules, as the $C_2H_2F_4$, can be broken under the effects of radiation and electric field, generating fluorine ions and then HF. Therefore, the HF production in the ecogas mixture was studied, with particular attention because the HF could be the possible cause of the observed dark current increase.

A measurement campaign of the CMS RPC exhaust gas composition was carried out following the same procedure described in chapter 4.2. The results are reported in Figure 6.8, which shows the HF concentration rate as a function of the background current, measured operating the CMS RPC chamber with 1 gas volume exchange per hour of standard mixture (green) or ecogas mixture (black). The HF concentration using the ecogas mixture is around 2.5 times greater than the standard gas mixture. Considering that the HFO constitute only 45% of the ecogas mixture, which contains other components inert in the process, while the $C_2H_2F_4$ represent the 95.2% of the standard mixture, one can conclude that HFO breaks five times more easily than $C_2H_2F_4$. This can also be understood by the fact that HFOs have a very short atmospheric lifetime, which indeed gives the low GWP value, but on the other hand they decompose easier than $C_2H_2F_4$. The Fluoride measurements highlight that if HFOs will be used during

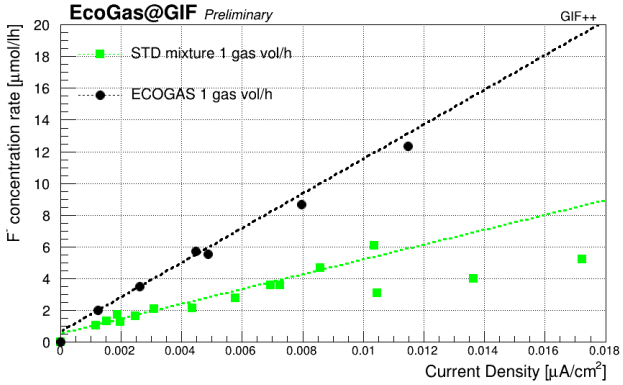

Figure 6.8: Fluoride concentration rate as a function of the background current, measured operating the CMS RPC chamber with 1 gas volume exchange per hour of standard mixture (green) or ecogas mixture (black).

HL-LHC, the accumulation of HF will be higher with respect to $C_2H_2F_4$, with the consequent possible effects on the detector longevity.

Further tests to fine-tune the gas component fractions are needed to find the best compromise between the detector performance and longevity.

7 L1 Muon trigger study

The CMS L1 trigger system is responsible for selecting 10^5 interesting events for physics studies out of 40 million proton-proton collisions occurring every second at the LHC [42]. The goal of the L1 trigger is to efficiently select the interesting events and reject the background. The L1 trigger has to make the trigger decision in less than 4 μs to cope with the rate of the incoming collision data. In order to meet this latency requirement, the CMS L1 trigger system is made of custom hardware processors such as FPGAs that are capable of massive parallel data processing at high speed.

The L1 trigger consists of two parts: the muon trigger and the calorimeter trigger, which both send data to the Global Trigger (GT).

The Run I L1 Muon Trigger system was designed to process the information from each subdetector separately and combine the outputs in a later stage, resulting in a robust muon track reconstruction and momentum assignment [111].

The upgraded L1 Muon Trigger for Run II was designed to exploit the subdetector redundancy at an earlier stage, thus improving the overall performance [112–114]. For this reason, the upgraded system is composed of three separate Muon Track Finders (MTF) covering different η regions. The Barrel Muon Track Finder (BMTF) receives data from DT and RPC detectors, and covers the $|\eta| < 0.83$ [115, 116]. The Endcap Muon Track Finder (EMTF) receives data from RPC and CSC in the region $|\eta| > 1.24$. Finally, the Overlap Muon Track Finder (OMTF) receives data from the three subdetectors in the intermediate region $0.83 < |\eta| < 1.24$. The L1 muon trigger schematic and detector coverage are presented in Figure 7.1.

In the barrel region the muon primitives are sent to the TwinMux, which is a

Table 7.1: DT TPs quality codes identifier.

Description	Symbol	Code
HTRG on inner and outer layer	HH	6
HTRG on inner or outer layer and LTRG on inner or outer layer	HL	5
LTRG on inner and outer layer	LL	4
HTRG on outer layer	H_o	3
HTRG on inner layer	H_i	2
LTRG on outer layer	L_o	1
LTRG on inner layer	L_i	0
Null track		7

preprocessor layer for the track finder. The TwinMux system consists of six μTCA crates with TwinMux processors. At this level the RPC hits in adjacent strips are clusterized into a single Trigger Primitive (TP), and TwinMux can output up to two clusters of RPC hits per bunch crossing and per RPC roll.

Concerning the DT, as described in chapter 3.1.4.1 the chambers from the three innermost stations are equipped with 3 superlayers (SL) consisting of 4, half staggered, layers of parallel DT cells. Two SL measure the muon trajectory along the bending plane (R - ϕ), whereas the remaining SL measures the position along the longitudinal (R - θ) plane. MB4 chambers are, instead, equipped only with two R - ϕ SL. The DT TPs are built in each SL based on the combination of the 4 single DT layers. The evaluated parameters to build the TPs are the position, computed in the SL centre, and the angular k-parameter $k = h\ tan\Psi$, with Ψ being the angle of the track with respect to the normal to the chamber plane in the transverse projection and $h = 13\ mm$ being the distance between the wire planes. The different combinations of the 4 layers give six couples of planes, each one providing a measurement of the position (through a x-equation) and of the k-parameter (through a k-equation) of the track. Therefore each couple gives its own measurement of the track direction. If there is a coincidence of all the six k-parameters, the TP corresponds to the alignment of four hits and it is marked as High Quality Trigger (HTRG), while in any other case, with a minimum of three coincident k-parameters, it corresponds to the alignment of only three hits and it is marked as Low Quality Trigger (LTRG). The different combination of the quality markers for the inner and outer layers of the DT SL are reported in Table 7.1. The TwinMux combines the TPs from DT and RPC, to generate better quality candidates, called superprimitives (SP). The SP data consist of muon stubs, bending angle and

quality bits. The algorithm works as follows.

If the DT TPs have quality code 4, 5 or 6, which means both inner and outer DT layers are present, then the RPC information are not used. These SP are identified with the code "rpc bit0".

If DT TPs have quality code 2 or 3, which means DT TPs having only 1 high quality layer, then the RPC TPs are translated into the DT coordinate conventions and the DT TPs are matched to RPC TPs based on the azimuthal angle, within a three units bunch-crossing window centered around the DT TPs bunch-crossing. For DT TPs that could be matched to an RPC TP, the SP bunch-crossing timing is set based on RPC information. These SP are identified with the code "rpc bit1".

Finally, if the DT TPs have only 1 low quality layer (code 0 and 1), or no DT TPs is found (code 7), then the algorithm tries to build an RPC only segment in the first two stations by correlating the two RPC layers. The position is given by the average angular position (ϕ) of the two clusters in a temporal coincidence and a bending angle (ϕ_b) given by:

$$\phi_b = arctan(\frac{x_2 - x_1}{D} - \phi) \tag{7.1}$$

where x_1 and x_2 are the cluster positions and D is the distance between the two RPC layers. The RPC only primitive with the smallest ϕ_b is chosen. These SP are identified with the code "rpc bit2".

TwinMux is finally in charge of sending the SP to the BMTF and to the OMTF. The BMTF, implemented in 690 series Virtex-7 FPGA, uses the TwinMux data to reconstruct muon tracks and calculate the physical parameters, which are the transverse momentum, the ϕ and η angles, the quality of the candidate and the track addresses.

The OMTF combines simultaneously DT, RPC, and CSC primitives into single tracks using a Golden Pattern (GP) algorithm. The hit pattern is compared to a limited number of pre-computed hit patterns. These GPs hold information about the bending distribution between each layer for a given muon transverse momentum. Reference hits from different layers can be tested, each resulting in an alternative muon p_T hypothesis. The track parameters of the GP closest to the actual hit pattern are chosen. The final result is cleaned for duplicates.

The EMTF uses information from both RPC and CSC. RPC hits are used in case

of missing CSC information. The RPC hits are clustered and assigned coordinates (θ, ϕ) by the Concentration Pre-Processing and Fan-out card (CPPF), which consists of eight μTCA boards with FPGA processors. EMTF compare all track segments to predefined patterns in a region, requiring at least two stations with matches to declare a potential track.

Finally, the output of the three systems is collected by the Global Muon Trigger (μGMT). Each MTF forwards the three best track candidates per 60° sector in ϕ. The μGMT ranks the muons by transverse momentum and quality, removes the reconstruction duplicates across boundary regions, and sends the output muon collection to the Global Trigger (GT).

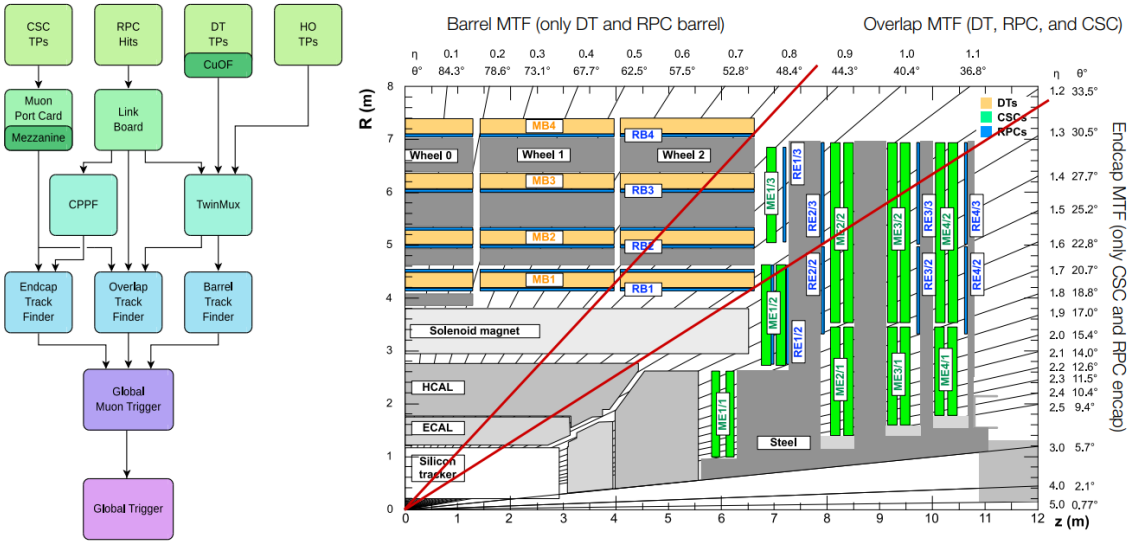

Figure 7.1: Left: L1 muon trigger architecture during LHC Run II. Right: Muon track finder coverage.

7.1 Optimization of the RPC cluster size cut for the L1 muon trigger

So far only RPC TPs with 3 or less strips have been used at L1 muon trigger. The average RPC cluser size is around 2, nevertheless, a not negligible fraction of TP, around 4%, have cluster size higher than 3, as shown in Fig.7.2. This cut was introduced due to MTF firmware limitations in the clustering algorithm, but was never optimized. In view of the next runs, the RPC information usage at the L1 muon trigger has been

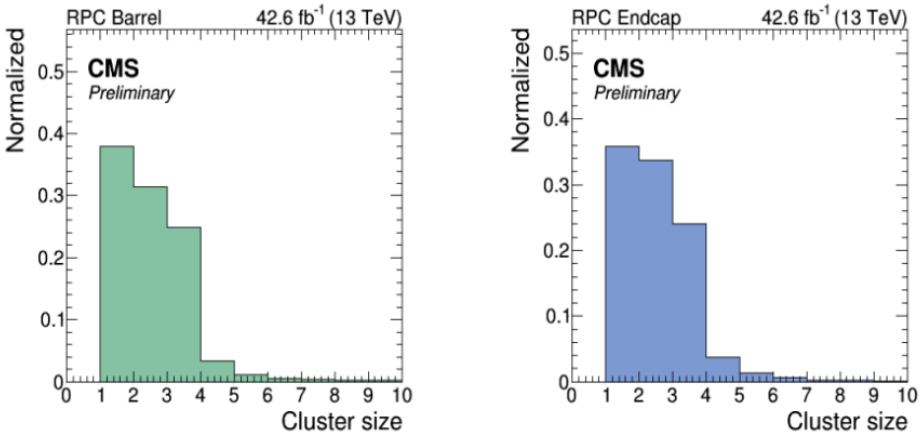

Figure 7.2: RPC cluster size distribution for barrel (left) and endcap (right)

optimized. In particular, a study to optimize the RPC cluster size cut was performed taking into account all the relevant factors such as: the RPC spatial resolution, the RPC TPs rate, the RPC muon hit efficiency, and finally the MTF trigger rate and efficiency. For the study the 2018 Single muon dataset has been used, and the cluster size cut operated by the CPPF and TwinMux has been emulated.

The RPC spatial resolution has been estimated using the segment extrapolation algorithm, where an high quality DT/CSC segment associated to a stand-alone muon track is extrapolated to the RPC strip plane [117]. The spatial resolution is quantified by the standard deviation (σ) of the residuals distribution between the expected hit position ($\phi_{RPC\ hit\ projected}$) and the reconstructed hit position ($\phi_{RPC\ hit}$):

$$\sigma = \phi_{RPC\ hit\ projected} - \phi_{RPC\ hit} \tag{7.2}$$

Figure 7.3 shows the RPC spatial resolution in ϕ coordinate, for both barrel and endcap, as a function of the cluster size cut (left) and the cluster size (right).

The plot in Figure 7.3 (left) shows that, in both barrel and endcap, the spatial resolution remains almost constant and it is not significantly degraded when the cluster size cut is relaxed. This because the relative fraction of hits introduced by relaxing the cluster size cut is small, and because the spatial resolution of the TPs having cluster size greater than 3 is not degraded, as reported in Figure 7.3 (right). It must be specified that in the right plot, the point at cluster size 6 includes all the events having cluster size equal or greater than 6, and the statistical error is huge due to the

low amount of events. The same goes for the left plot, where the last point includes all the TPs and no any cluster size cut is applied.

The slightly different resolution between barrel and endcap is due to the different strip pitch, slightly finer in the latter. Figure 7.4 (left) shows the distribution of the

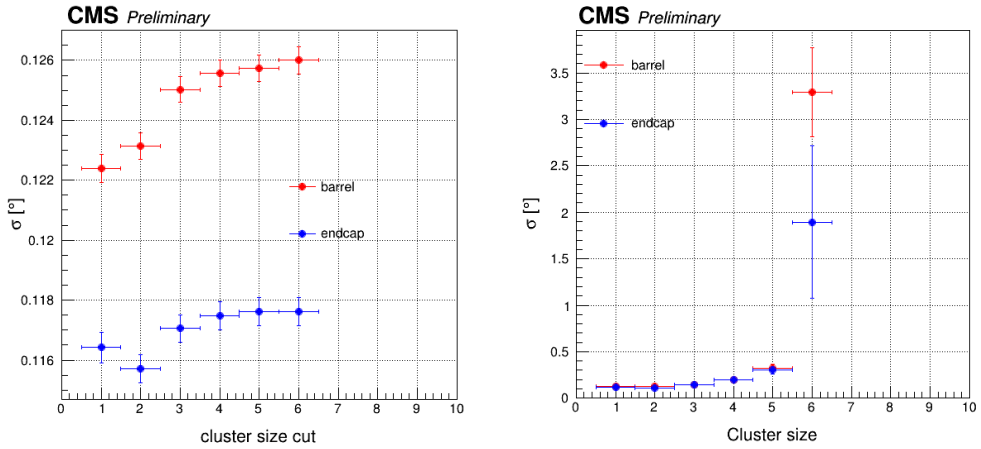

Figure 7.3: Spatial resolution of the RPC TPs in barrel (red) and endcap (blue), as a function of the cluster size cut (letf) and cluster size (right).

RPC TPs sent by the endcap CPPF to the EMTF as a function of the cluster size cut. The TPs slightly increases when the cluster size cut is relaxed, but does not diverge. In particular, the TPs increases of ≈3% applying a cluster size 4 instead of 3.

Figure 7.4 (right) shows the distribution of the SP generated by the barrel TwinMux as a function of the cluster size cut. In yellow is reported the total amount of SP, which slightly increases when the RPC cluster size cut is relaxed. In particular the SP increases of ≈0.2% applying a cluster size 4 instead of 3. The cut relaxation has less impact with respect to the endcap, since in the barrel around 92% of the SP are generated by the DT only.

The contribute of the different SP types are reported as well. A slight decrease of ≈ 0.1% is observed for the SP that use only DT data, identified as "rpc bit-0", when the RPC cluster size cut is relaxed at 4. The decrease is explained by the fact that a fraction of SP used DT only because the RCP TPs was not accepted due to the higher cluster size, while they can be used when the cluster size cut is relaxed. Indeed, the number of SP "rpc bit-1" slightly increases of ≈ 0.1%. Finally, the SP "rpc bit2", that represents the RPC only, increases of ≈ 7% applying a cluster size 4 instead of 3. As expected the main impact of the cluster size cut relaxation is for the

SP RPC only, nevertheless, these SP represent just the 3% of the total SP amount. The RPC contribution is important when the DT TPs present only 1 high quality layer

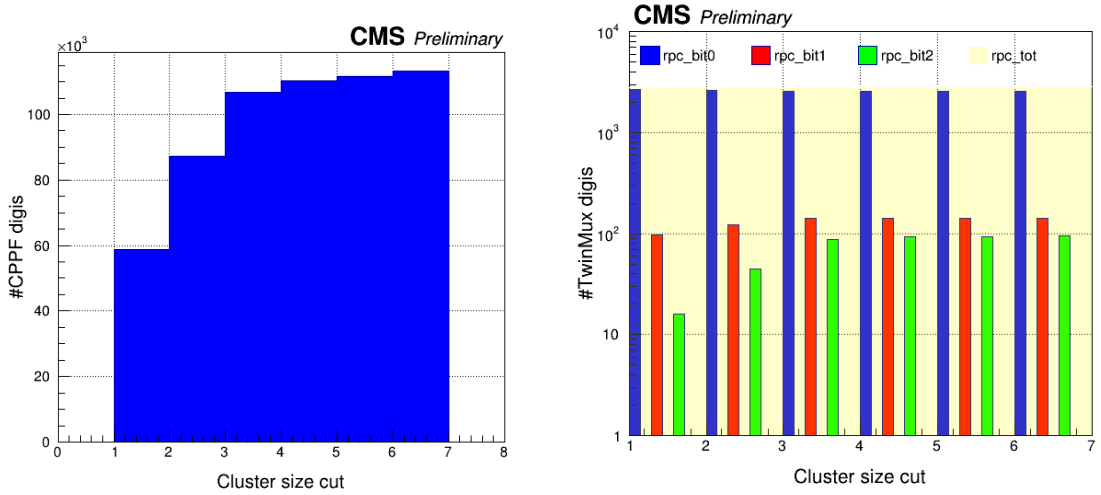

Figure 7.4: Distribution of the TPs as a function of the cluster size cut, in the edcap CPPF (left) and barrel TwinMux (right). For the barrel the contribute of the different TPs types is reported: rpc-bit0, rpc-bit1 and rpc-bit2.

(quality code 2 and 3), and in this case the RPC cluster size relaxation can improve the reconstruction. The TPs having quality code 3 represent around 18% with respect to the total amount, and the sum of the TPs quality 3 and 2 is around 41%. Of this 18%, around the $\approx$ 72% of the TPs are DT only, the SP using DT and RPC are $\approx$ 11%, and the SP RPC only represent the $\approx$ 17%. An example is given in Figure 7.5 (left), which reports the TPs having quality code 3 as a function of the cluster size cut, divided for the different TPs types. As convention, the TPs RPC only are also assigned to the quality code 3. Figure 7.5 (right) reports the same quantities but expressed in percentage. The results report a slight decrease, of $\approx$ 0.2%, for the SPs that use only DT data, when the RPC cluster size cut is relaxed at 4. An increase of $\approx$ 1.5% is observed for the SP that use DT and RPC, and finally an increase of $\approx$ 7% is observed for the RPC only TPs. In total the SPs increase of $\approx$ 1.5%.

All the results reported demonstrate that the cluster size cut relaxation would not have any significant impact on the data transmission.

Figure 7.6 represents the RPC muon hit efficiency as a function of the cluster size cut, in the barrrel (left) and in the endcap (right). For the efficiency calculation, all the RPC chambers have been used, including the problematic one, which are off. This is the reason why the efficiency is 88% at the nominal cluster size cut. The

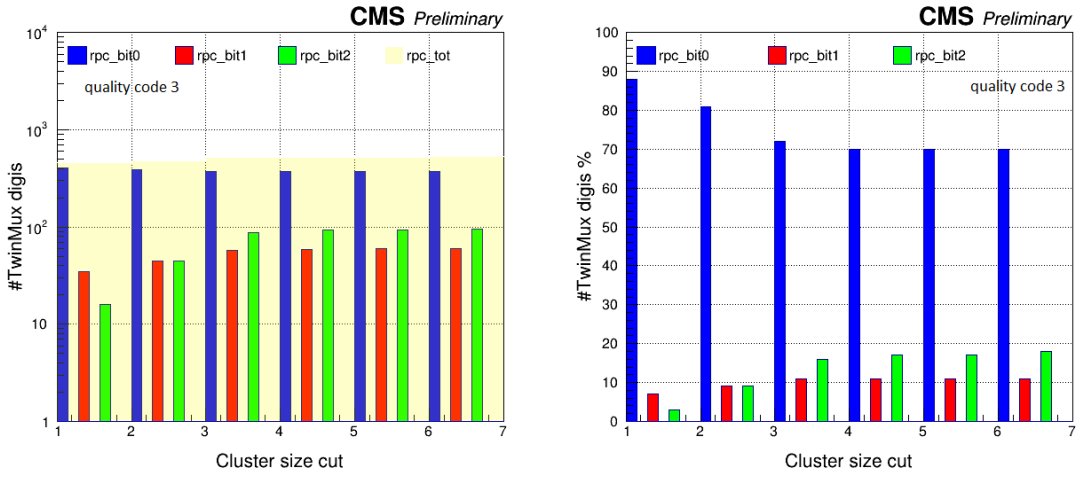

Figure 7.5: Left: TPs having quality code 3 as a function of the cluster size cut, divided for the different types: rpc-bit0, rpc-bit1 and rpc-bit2. In the right plot the TPs contribution is reported in percentage.

efficiency estimation was done using the tag-and-probe method [56]. The RPC muon hit efficiency increase is evident when the relaxation of the cluster size cut is applied. In particular, the efficiency rises of $\approx 2\%$ in the barrel when the cluster size cut is increased at 4, and $\approx 4\%$ in the endcap.

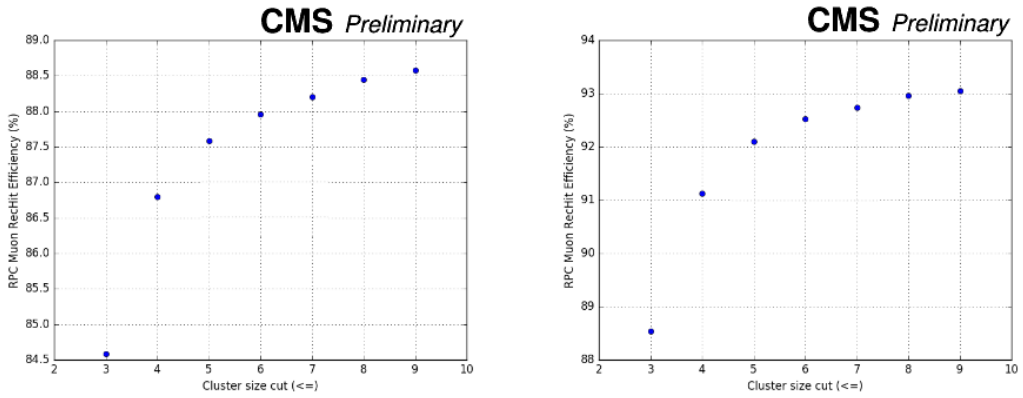

Figure 7.6: RPC muon hit efficiency as a function of the cluster size cut, in the barrel (left) and in the endcap(right).

Finally, the impact of the cluster size cut on the MTF trigger rate and efficiency has been performed using the tag-and-probe method based on the re-emulation of MTF algorithms. The efficiencies simulated in the three MTF applying different cluster size cut are reported as a function of the p_T in Figure 7.7. Relaxing the RPC cluster size cut has a small but positive impact on muon efficiency, especially at high p_T. In particular, the muon efficiency rises up to 0.5% in the OTMF when a cluster size cut

at 4 is applied. The MTF muon trigger rate remains stable when the RPC cluster size

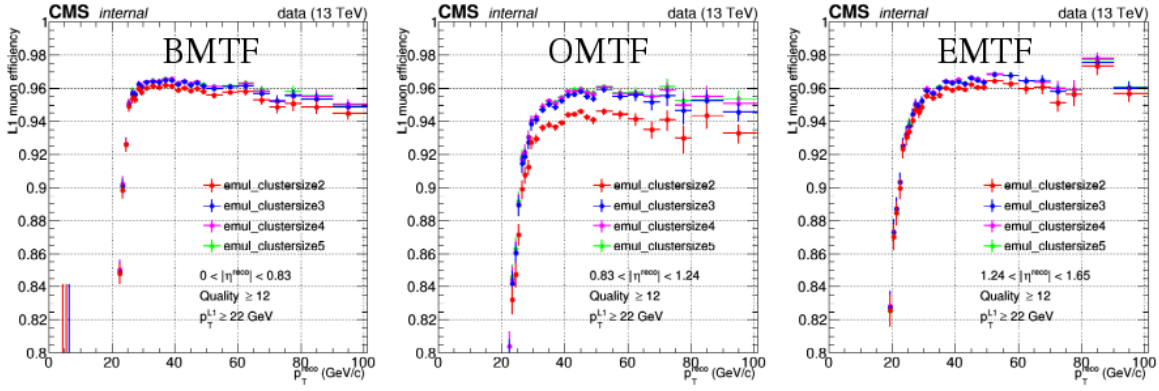

Figure 7.7: MTF efficiency as a function of p_T,applying different RPC cluster size cuts. The results are shown for the three regions: BMTF (left), OMTF (center) and EMTF (right).

cut is relaxed, as shown in Figure 7.8, which represents the muon trigger rate ratio between the trigger rate applying the cluster size cut 3, and the trigger rate applying the cluster size cut 4. The results are shown for the three regions: barrel (left), overlap region (center) and endcap (right).

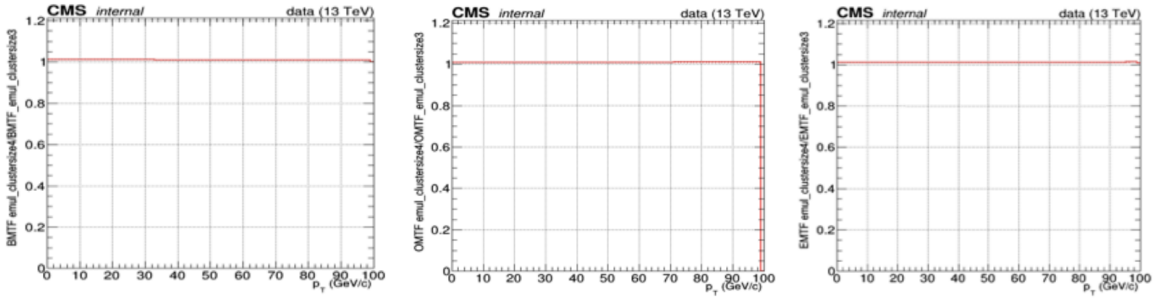

Figure 7.8: MTF muon trigger rate ratio between the trigger rate applying the cluster size cut 3, and the trigger rate applying the cluster size cut 4. The results are shown for the three regions: barrel (left), overlap region (center) and endcap (right).

In conclusion, the study proved that increasing the RPC cluster size cut from 3 to 4, would not affect the spatial resolution, nor the TPs rate, but the RPC muon hit efficiency would increase. Finally, the MTF efficiency have a small but positive increase, without any significant increase in the muon trigger rate.

The study lead to the OMTF community to decide to apply the cluster size cut 4 in the future runs, while in the BMTF and EMTF community the discussion is ongoing to evaluate the impact at the firmware level.

8 Conclusions

During HL-LHC the collider will increase the instantaneous luminosity up to $5 \times 10^{34}\ cm^{-2}s^{-1}$, providing to the experiments an additional integrated luminosity of about 3000 fb^{-1} over 10 years of operation, starting from 2026. The CMS experiment planned a broad upgrade project in order to maintain the excellent performance during HL-LHC. The work described in this thesis is related to the RPC system upgrade project, and the conclusions are summarized following:

- The present CMS RPC system has been certified for 10 LHC years operation, and the longevity studies have shown stable performance after having accumulated in average $\approx 10\ mC/cm^2$, equivalent to almost 7 years of operation. Nevertheless, a general dark current increase was observed, especially in the most exposed regions, and a correlation with the background rate and the gas flow was found. As a possible reason of the detector aging, and in particular for the observed dark current increase, the HF production rate was studied. The HF production has been studied first of all at GIF++, where the measurements demonstrated that the HF production rate depends on the background rate and the concentration depends on the gas flow. It has also been demonstrated that the HF can be trapped and deposit inside the gas gap if the gas flow is not enough with respect to the HF production rate, and it is possible to remove it (or partially remove it) operating the detector with argon. A similar study has been performed in CMS in 3 representative stations, confirming the GIF++ results. Additionally, a linear correlation between the ohmic current and the HF concentration was found, validating the hypothesis that the dark current increase was induced by

the HF. The results demonstrate that for good detector operations it is necessary to fine tune the gas flow as a function of the background rate so that the HF is efficiently removed. These results are very important, especially in view of the next LHC and HL-LHC runs, when the luminosity will increase.

HL-LHC will be a challenge for the RPC system since the expected operating conditions are much harsher with respect to those for which the detectors were designed, and could induce non-recoverable aging effects which can alter the detector performance. A new longevity test to estimate the impact of HL-LHC is started at GIF++ where few RPC detectors are exposed to intense gamma radiation. The main detectors parameters are studied as a function of the integrated charge and the performance studied with muon beam. After having collected a significant amount of the total irradiation, around 70%, the detectors performance and parameters are stable, and no evidence of aging effect has been observed.

- The RPC system will extend the muon eta acceptance from $|\eta| = 1.8$ to 2.4, increasing the muon system redundancy for both muon tracking and triggering in the forward region. Two endcap stations RE3-4/1 will be equipped with the new iRPC detectors, which are based on the RPC technology but with thinner gas gap and HPL thickness, and equipped with a more sensitive FEB.

  A dedicate study to estimate the iRPC expected background rate during HL-LHC was performed. The detector sensitivity has been studied using Monte Carlo methods, first at GIF++ comparing the simulation and experimental data in order to validate the simulated iRPC geometry. The good results achieved allowed to study the iRPC sensitivity with respect to the different particles that compose the CMS background. The sensitivity values were then used to rescale the incident particles fluxes and so to estimate the expected background rate. The study allowed to define the requirement of the minimum iRPC rate capability.

  The extensive R&D activity allowed to define the baseline for the new iRPC detector to fulfil the requirements, and to validate the detector technology and the new front end electronics board at the expected background.

  Finally, the longevity studies to certify the iRPC for the entire HL-LHC are

ongoing at GIF++. Preliminary results highlighted a gaps oiling problem during the production: not polymerized linseed oil that caused a dark current increase was found. Test to improve the oiling procedure and the oil mixture are ongoing.

- A collaboration among CMS, ATLAS, ALICE and CERN EP-DT groups was set up to search an RPC eco-friendly gas mixture. A new ecogas mixture based on HFO has been characterized at GIF++ at several irradiation levels. Preliminary results shown a shift of the working point at higher voltage ($\approx$ 2 kV) with respect to the standard mixture. Additionally, the average avalanche charge was measured around 5 times higher, and the average cluster size around 35% higher.

  The detectors stability study is ongoing and preliminary results show a dark current increase. As a possible reason the HF production was studied, and it was found that the concentration is around 2.5 times higher than the standard mixture. If HFO will be used during HL-LHC, the possible aging effects, including the HF, should be carefully considered. Further studies to fine-tune the gas component fractions are needed to find the best compromise between the detector performance and longevity.

- A study to optimize the use of the RPC information at the L1 muon trigger has been performed. The study was focused on the optimization of the RPC cluster size cut applied at the MTF level. The applied cluster size cut rejects the RPC TP having cluster size higher than three. The cluster size cut was applied due to firmware limitations, but was never optimized, therefore all the important possible implications, have been studied.

  The results demonstrated that increasing the RPC cluster size cut from 3 to 4, does not degrade the spatial resolution of the reconstructed muons and the TPs rate does not diverge, having therefore no significant impact on the data transmission, while the RPC muon efficiency rises of 2-4%, Finally, relaxing the RPC cluster size cut has a small but positive impact on MTF muon efficiency, especially at high p_T, in particular in the OTMF it rises of $\approx$ 0.5%. The study led the OMTF community to decide to apply the cluster size cut 4 in the future runs, while in the BMTF and EMTF community the discussion is ongoing to evaluate the impact at the firmware level.

List of Figures

2.1 Plan of LHC and HL-LHC operation, showing the evolution of the beam energy, the instantaneous and integrated luminosity. 6

3.1 Overall view of CMS detector and its subdetectors. 10

3.2 Overview of the CMS tracker system. 11

3.3 Schematic view of the CMS Muon spectrometer. The interaction point is at the lower left corner. The locations of the various muon stations are shown in color (MB = DT = Drift Tubes, ME = CSC = Cathode Strip Chambers, RB and RE = RPC = Resistive Plate Chambers). M denotes Muon, B stands for Barrel and E for Endcap. The magnet yoke is represented by the dark gray areas. 14

3.4 Illustration of the Drift Tube Chamber: drift cell unit (left), SuperLayers configuration (right). 15

3.5 Cathode Strip Chambers geometry (left), and the principle of operation of a CSC, with cross-section across the wires (right-top) and across the strips (right-bottom). 16

3.6 Left: Double gap RPC layout. Right: Comparison of efficiency curves of CMS RPC double and single-gap, measured with cosmic muons. 17

3.7 CMS RPC system layout in the Barrel (left) and in the endcap (right). 18

3.8 RPC geometry in barrel (left) and endcap (right). The barrel chambers are segmented in two or three rolls. In the endcpap chambers, the top gap layer is divided into two gaps: Top Narrow (TN) and Top Wide (TW), due to the partitioning of the read-out strips into three rolls. The bottom layer only consists in one gap (BOT). 20

3.9 Architecture of the CMS Level 1 Trigger. 21

3.10 *R-z* cross section of a quadrant of the CMS detector, including the Phase-II upgrades (RE3/1, RE4/1, GE1/1, GE2/1, ME0). 24

4.1 RPC hit rate as a function of pseudorapidity for the different RPC stations is shown (blue) with the results of FLUKA simulation superimposed (red). The full markers correspond to the barrel layers, while the empy ones to the endcap. The top plots show the first (left) and second (right) barrel (RB1 and RB2) and endcap (RE1 and RE2) stations, while the bottom plots describe third and forth barrel (RB3 and RB4) and endcap (RE3 and RE4) stations. Hit rate estimated values were evaluated at $1.5 \times 10^{34}\ cm^{-2}s^{-1}$ instantaneous luminosity and an average over ϕ was taken for each layer shown. 29

4.2 RPC average hit rate as a function of instantaneous luminosity for the Barrel (left) and Endcap (right) stations (right). The results have been obtained using 2018 proton-proton collision data, selecting runs with stable beam. The luminosity values are provided by the official CMS luminosity tool. 29

4.3 Overall efficiency distribution during the 4 years of Run II data taking, measured in the Barrel (left) and in the Endcap (right). 30

4.4 CMS RPC efficiency (left) and muon cluster size (right) monitored during Run II as a function of time. The plots on top represent the barrel stations, while the plots on bottom the stations in the positive endcap. Results for the negative disks are similar. 31

4.5 Ohmic currents measured as a function of time. The currents were measured during 2018 in four RPC stations: W0 in the barrel and RE+1, RE+4, RE-4 in the endcap. 32

4.6 Ohmic currents as a function of time, measured at 6.5 kV in four RPC stations: W0 in the barrel and RE+1, RE+4, RE-4 in the endcap. The ohmic currents were measured during the Heavy Ion period at the end of 2018. 33

4.7 Ohmic currents measured at 6.5 kV as a function of the integrated luminosity. The currents were measured during 2018 in four RPC stations: W0 in the barrel and RE+1, RE+4, RE-4 in the endcap. 34

4.8 GIF++ experimental set-up for the HF measurements. 37

4.9 Left: F^- concentration as a function of time, at different background rate (ABS), operating with one gas volume exchange per hour. Right: F^- concentration as a function of time, operating with three different gas flow, at fixed background rate (ABS). 38

4.10 Left: F^- concentration rate as a function of the background rate (and its corresponding current on the top X-axis), measured with three different gas flow: 0.2, 1 and 3 gas volume exchanges per hour. Right: Ratio of the F^- concentration measured at different gas volume exchanges with respect to 1 gas volume exchange per hour. . . 38

4.11 F^- concentration trapped inside the gas gap and not efficiently removed. The concentration was measured at different background rate, and with three different gas flow. The estimation was done considering the F^- accumulated during the last 8 hours of measurements, just after the detector switching off. 39

4.12 F^- concentration as a function of time (left) and as a function of the integrated luminosity (right). The measurements have been performed at the gas exhaust of 3 regions: W0 in the barrel and RE+1, RE+4 in the endcap. 42

4.13 Ohmic current as a function of the F^- concentration. 42

4.14 Linear extrapolation of the average background rate (left) and average integrated charge (right) expected during HL-LHC period at $5 \times 10^{34}\ cm^{-2}s^{-1}$ and 3000 fb^{-1}. 44

4.15 CERN Gamma Irradiation Facility (GIF++) layout. 45

4.16 CMS RPC set-up at GIF++ for the longevity studies (left), and relative position of the chambers with respect to the source. 45

4.17 Integrated charge versus time, accumulated during the longevity test at GIF++ for RE2/2 (red) and RE4/2 (blue) irradiated chambers. The RE4/2 chamber has been turned on a few months later because of the total gas flow limitations. Different slopes account for different irradiation conditions during data taking. 47

4.18 Characteristic current curve for the RE2/2 irradiated chamber operating with pure argon. In the statistics box, the fit parameters values, the resistance, the resistivity and the HV onset values are reported. 48

4.19 Left: average resistivity for both the irradiated chamber (blue) and the reference chamber (red), monitored as a function of the RE2/2 irradiated integrated charge. The resistivity value for each chamber is the average with respect to the three gaps which made up a chamber. The resistivity values are corrected for the temperature variation and normalized at $20^{\circ}C$. Right: resistivity ratio (blue) and current ratio (red) between irradiated and reference chamber. 50

4.20 Top: RE2/2 irradiated chamber currents curves at different integrated charge values. Bottom left and Right: RE2/2 irradiated (blue) and reference (red) chamber currents monitoring versus the integrated charge, at 6.5 kV (left), and at 9.6 kV (right). . . 51

4.21 Left: average noise rate versus the integrated charge, for RE2/2 irradiated (blues) and reference (red) chamber, at 9.6 kV. The electronics threshold is set at 220 $mV \approx$ 150 fC. Right: RE2/2 noise rate strip profile at different integrated charge values, at the working point voltage. 52

4.22 GIF++ beam trigger, composed by threes scintillators: two placed outside on each side of the GIF++ bunker (S_{up} & S_{down}), in order to be shielded from the gamma background and to avoid fake coincidences, and the third scintillator (S_n) is placed in near to the tested chambers. Two additional RPCs (trk-1 & trk-2), represented in green, are used as tracking system. 53

4.23 Time profile (left): typical Gaussian distribution of RE2/2 irradiated chamber hits recorded within the trigger time window. Right: 2D plot shows on the Y-axis the RE2/2 irradiated chamber time profile distribution, and on the X-axis the beam strip profile. 54

4.24 Left: result of the calibration test to obtain the linear function, that associate the tracking chambers hits to the tested RE2/2 irradiated chamber hits. Right: typical Gaussian fit of the residual distribution of RE2/2 irradiated chambers. The residuals are calculated as the difference between the expected fired strip, found from the projected muon track, and the fired cluster center. 55

4.25 Typical RE2/2 irradiated chamber efficiencies as a function of the effective high voltage, measured with muon beam at different background radiation. The Front End Board (FEB) is the standard CMS RPC electronics, and the applied threshold is 220 $mV \approx 150$ fC, as applied in CMS [39]. 56

4.26 RE2/2 irradiated chamber efficiency as a function of the effective high voltage, taken without background (left) and under gamma background rate of about 600 Hz/cm^2 (right). The efficiency is measured during different TB corresponding to different fractions of the target charge to integrate. 57

4.27 Left: RE2/2 irradiated chamber efficiency as a function of the HV gas, at different background irradiations and at different integrated charge values. Right: monitoring of the RE2/2 irradiated chamber resistivity, measured with argon and estimated with the HV rescale method. 58

4.28 RE2/2 irradiated chamber efficiency at working point as a function of the background rate, measured at different integrated charge values. 58

4.29 RE2/2 irradiated chamber density current (left) and deposited charge (right), measured at the working point as a function of the background rate, at different integrated charge values. 59

4.30 RE2/2 irradiated chamber gamma cluster size (left) and muon cluster size (right), measured at the working point as a function of the background rate, at different integrated charge values. 59

5.1 Left: View of CMS disk 3 positive, instrumented with RPC in the rings 2 and 3, while the first ring is empty (in red). Right: Simulated comparison between the L1 single muon trigger efficiencies with and without the RPC information, as a function of $|\eta|$. The contribution of iRPC starts above $|\eta| = 1.8$ 62

5.2 Average charge per avalanche measured on 1.2 mm (full circles), 1.4 mm (open circles), 1.6 mm (triangles), and 2.0 mm (squares) double-gap RPCs, as a function of the electric field strength [81]. Test performed at the KOrean DEtector Laboratory (KODEL). 63

5.3 Efficiency and average cluster size of a 1.4 mm double-gap iRPC (prototype-1) as a function of the effective high voltage, tested without gamma background (left) and under a gamma background rate of $\approx 2\ kHz/cm^2$ (right). The measurements were performed applying a 300 μV $\approx 50\ fC$ threshold. 64

5.4 iRPC efficiency at working point (left), working point (center) and average muon cluster size at working point (right), as a function of the gamma background cluster rate. The measurements were performed applying a 300 μV ≈ 50 fC threshold. . . 65

5.5 Average avalanche charge at working point, as a function of the cluster rate, measured for the standard RPC (black) and iRPC (red). 65

5.6 Front Electronics Board that hosts one PETIROC ASIC and the FPGA that includes the TDC (top right) and the schematics of the PETIROC ASIC (left). 66

5.7 Left: efficiencies as a function of the effective high voltage measured at different background rate. Right: evolution of the efficiency at working point at different background cluster rate. The measurements were performed with 81 fC threshold. 67

5.8 Left: measured time difference of the signal arrival time of each of the two fired strip ends $T_{HR} - T_{LR}$ as a function of the position of the muon beam with respect to the RPC. Right: time resolution at the center of the detector. 68

5.9 Distribution of the time differences of two iRPC detectors. The mean value divided by square of 2 represents the absolute time resolution. 68

5.10 Rate (right) and sensitivity (left) measurements at different background conditions (ABS). The plots show the comparison between experimental data from GIF++ (red squares) and simulated data: without charged particles energy threshold (black) and with charged particles energy thresholds of 100 keV (green) and 200 keV (blue). . 71

5.11 Left: distribution of the position along the detector thickness (Z direction), for both gas gaps, where the primary electrons are produced after the interaction of the incident gammas with the detector materials (HPL gap-1 = red and HPL gap-2 = blue), and where the electrons ionize in the gas gap (gas gap-1 = green and gas gap-2 = yellow). Right: GIF++ gamma energy distribution applying different source filters (ABS). The number of events for each ABS has been normalized. 73

5.12 FLUKA Monte Carlo simulation of the particles rate flux (neutrons, gammas and charged particles) as a function of the energy of the incoming particles, expected during HL-LHC (14 TeV and 5×10^{34} $cm^{-2}s^{-1}$) in the endcap RE3/1 (left) and RE4/1 (right) stations. 74

5.13 Left: Monte Carlo estimation of the iRPC sensitivity with respect to the different background particles (neutrons, photons, electrons and positrons) as a function of the kinetic energy of the incident particles. Right: contribution from the different processes to the detector gamma sensitivity (black) as a function of the gammas kinetic energy: Compton (red), pair production (blue) and photoelectric (green). . 76

5.14 Monte Carlo simulation of the background rate expected in the endcap RE3/1 station during HL-LHC, as a function of the incoming particles energy (left) and as a function of the distance (R) from the centre of the CMS beam pipe (right). The contribution of the different particles is reported. 76

5.15 Top: iRPC prototype-1 dark currents curves at different integrated charge values. Bottom: iRPC prototype-1 dark currents (red) and noise rate (blue) monitoring versus integrated charge, at 5 kV (left), and at 7 kV (right). 78

5.16 iRPC prototype-1 efficiency (left) and working point (right) as a function of the gamma background cluster rate. The measurements have been performed before the longevity test, and after having collected $\approx 90\ mC/cm^2$. 79

5.17 Left: dark current curves of iRPC prototype-2, at different integrated charge values. Right: dark current of iRPC prototype-2, monitored versus the integrated charge, at 5 kV (blue) and at the working point voltage $\approx 7\ kV$ (red). 80

5.18 Pictures of the iRPC prototype-1 inner surface after the irradiation (left), and the typical inner surface of a standard CMS RPC chamber (right). 81

5.19 Left: SEM image of the iRPC prototype-1 area around a spacer. Right: SEM images of the iRPC prototype-1 surface at the non-affected area (left), and the matt stain area (right), at magnification 1 kx (top) and 5 kx (bottom). 82

5.20 Left: picture of the iRPC prototype-1 gap sample used for the Vertical Scanning Interferometry (VSI) analysis. Center: VSI topography of the analysed sample. Right: VSI profile along the red line drawn in the 2-D map. 83

5.21 Left: Energy Dispersive X-ray Spectrometer (EDS/X-ray) of the iRPC prototype-1. The EDS analysis was performed in four sites of interest (SOI), and the chemical components in mass fraction are reported in the bottom left plot. The reported values correspond to the normalized weight percentage (wt.%) of the detected elements. Right: Nitrogen presence in the areas SOI-2 and SOI-3, measured with EDS technique in three different samples: not oiled iRPC, standard RPC, and iRPC prototype-1. 85

5.22 Left: roughness profile of a not oiled and not cleaned iRPC HPL sample, measured using a probe tip. Right: average roughness (R_a), measured in longitudinal and transversal directions, for different not oiled HPL samples, cleaned with different methods. 86

5.23 Left: dark current of the three irradiated small iRPC prototypes (Double-Oil-1 (DO-1), Single-Oil-1 (SO-1) and Single-Oil-2 (SO-2)), monitored as a function of the integrated charge. Right: picture of the inner gap surface of the Double Oil (DO-1) bottom gap. 89

6.1 Left: RPC efficiency (solid line) and streamer probability (dashed line) as a function of the effective high voltage, measured for gas mixtures with different combinations of $HFO-1234ze$ and CO_2. Right: iRPC efficiency (empty markers) and cluster size (full markers) as a function of the effective high voltage, measured for standard mixture (red) and ecogas mixtures (blue) based on 50% of $HFO-1234ze$, 45.2% of CO_2, 4.5% of iC_4H_{10} and 0.3% of SF_6 [45]. 93

6.2 Currents (left), rate (center) and average avalanche charge (right) versus the effective high voltage, measured for the CMS RPC at different background conditions (ABS). 94

6.3 Simulated background rate for the 5 chambers under test, and the background rate measured at working point for the CMS RPC equipped with FEB, applying a 150 fC threshold. 94

6.4 Currents versus the effective high voltage, measured in presence of gamma background with the standard gas mixture and with the ecogas mixture. Currents measurements performed for CMS RPC (left), and for CMS-iRPC (right). 95

6.5 Left: CMS RPC average avalanche charge versus the effective high voltage, measured in presence of gamma background, using the standard gas mixture (blue) and using the ecogas mixture (red). Right: CMS RPC average gamma cluster size distribution measured using the standard gas mixture (blue) and using the ecogas mixture (red). 95

6.6 Dark currents curves for the CMS RPC bottom gap (left) and for the top gap (right), monitored at different period during the irradiation test at GIF++. 97

6.7 Dark currents of CMS RPC bottom gap monitored as a function of the time during the irradiation period at GIF++. The dark current was measured at 6 kV (left) and at 12 kV (right). 97

6.8 Fluoride concentration rate as a function of the background current, measured operating the CMS RPC chamber with 1 gas volume exchange per hour of standard mixture (green) or ecogas mixture (black). 98

7.1 Left: L1 muon trigger architecture during LHC Run II. Right: Muon track finder coverage. 102

7.2 RPC cluster size distribution for barrel (left) and endcap (right) 103

7.3 Spatial resolution of the RPC TPs in barrel (red) and endcap (blue), as a function of the cluster size cut (letf) and cluster size (right). 104

7.4 Distribution of the TPs as a function of the cluster size cut, in the edcap CPPF (left) and barrel TwinMux (right). For the barrel the contribute of the different TPs types is reported: rpc-bit0, rpc-bit1 and rpc-bit2. 105

7.5 Left: TPs having quality code 3 as a function of the cluster size cut, divided for the different types: rpc-bit0, rpc-bit1 and rpc-bit2. In the right plot the TPs contribution is reported in percentage. 106

7.6 RPC muon hit efficiency as a function of the cluster size cut, in the barrel (left) and in the endcap(right). 106

7.7 MTF efficiency as a function of p_T,applying different RPC cluster size cuts. The results are shown for the three regions: BMTF (left), OMTF (center) and EMTF (right). 107

7.8 MTF muon trigger rate ratio between the trigger rate applying the cluster size cut 3, and the trigger rate applying the cluster size cut 4. The results are shown for the three regions: barrel (left), overlap region (center) and endcap (right). 107

List of Tables

2.1 Nominal LHC beam parameters 5

3.1 Main CMS RPC parameters 18

3.2 Main CMS RPC parameters 18

5.1 iRPC geometry implemented in GEANT simulation. Each detector material layer, with its corresponding density and thickness, is reported up to the strip panel placed between the two gaps, then the geometry is repeated for the second gap. 70

7.1 DT TPs quality codes identifier. 100

Bibliography

[1] The LHC Study Group, "The Large Hadron Collider Conceptual Design Report", CERN/AC 95-05, 1995.

[2] M. Benedikt, P. Collier, V. Mertens, J. Poole, and K. Schindl, "LHC Design Report Vol. 3: The LHC Injector Chain", CERN-2004-003-V3, 2004.

[3] L. Evans and P. Bryant, "LHC Machine", *JINST*, vol. 3, S08001 (2008).

[4] Particle Data Group, "Review of Particle Physics", *Phys. Rev. D*, vol. 98, 2018.

[5] https://twiki.cern.ch/twiki/bin/view/CMSPublic/LumiPublicResults

[6] F. Englert and R. Brout, "Broken Symmetry and the Mass of Gauge Vector Mesons," Phys. Rev. Lett., vol. 13, p. 321, (Aug, 1964). doi:10.1103/PhysRevLett.13.321

[7] P. W. Higgs, "Broken symmetries, massless particles and gauge fields", Phys.Lett., vol. 12, p. 132, (Aug, 1964). doi:10.1016/0031-9163(64)91136-9.

[8] The CMS Collaboration, "A New Boson with a Mass of 125 GeV Observed with the CMS Experiment at the Large Hadron Collider", American Association for the Advancement of Science, vol 338, 2012. doi 10.1126/science.1230816

[9] CMS Collaboration, "Precise determination of the mass of the Higgs boson and tests of compatibility of its couplings with the standard model predictions using proton collisions at 7 and 8 TeV", Eur. Phys. J., vol. C75, p. 212, 2015. doi:10.1140/epjc/s10052-015-3351-7.

[10] ATLAS Collaboration, "Observation of a new particle in the search for the Standard Model Higgs boson with the ATLAS detector at the LHC",Phys.Lett., vol. B716, p. 1, 2012. doi:10.1016/j.physletb.2012.08.020, arXiv:1207.7214.

[11] O. Kodolova et al. , "The performance of the jet identification and reconstruction in heavy ions collisions with CMS detector", The European Physical Journal C, 2007.

[12] D. Huterer and D. L. Shafer, "Dark energy two decades after: Observables, probes, consistency tests", Rept. Prog. Phys., 81(1):016901, 2018..

[13] N. Arkani-Hamed, S. Dimopoulos, and G. Dvali, "The Hierarchy problem and new dimensions at a millimeter", Phys.Lett., vol. B429, p. 263, 1998. doi:10.1016/S0370-2693(98)00466-3.

[14] J. L. Feng, "Naturalness and the Status of Supersymmetry", Ann. Rev. Nucl. Part. Sci., 63:351382, 2013.

[15] The ALICE Collaboration, K. Aamodt et al., "The ALICE experiment at the CERN LHC", *JINST*, vol. 3, S08002 (2008).

[16] R. S. Bhalerao and R. V. Gavai, "Heavy Ions at LHC: A Quest for Quark-Gluon Plasma", (2009), https://dx.doi.org/10.1007/978-81-8489-295-6_8, arXIv:0812.1619v1.

[17] The LHCb Collaboration, A. Augusto et al., "The LHCb Detector at the LHC", *JINST*, vol. 3, S08005 (2008).

[18] The LHCb Collaboration, "Observation of *CP* violation in charm decays", http://cds.cern.ch/record/2668357/.

[19] The ATLAS Collaboration, G.Aad et al., "The ATLAS Experiment at the CERN Large Hadron Collider", *JINST*, vol. 3, S08003 (2008).

[20] The CMS Collaboration, "The CMS experiment at the CERN LHC", *JINST*, vol. 3, S08004 (2008).

[21] The CMS Collaboration, "The CMS muon project: Technical Design Report",Technical Design Report CMS, CERN-LHCC-97-032. CERN, Geneva, 1997.

[22] The CMS Collaboration, "The CMS Magnet Project", (1997), https://cds.cern.ch/record/331056.

[23] The CMS Collaboration, "The CMS tracker system project: Technical Design Report", Technical Design Report CMS. CERN, Geneva, 1997.

[24] The CMS Collaboration, "Description and performance of track and primary-vertex reconstruction with the CMS tracker", JINST, vol. 9, (2014), https://dx.doi.org/10.1088/1748-0221/9/10/p10009, arXiv:1405.6569v2

[25] The CMS Collaboration, "The CMS electromagnetic calorimeter project: Technical Design Report", CMS-TDR-4, CERN/LHCC 97-033, (1997).

[26] The CMS Collaboration, "The CMS hadron calorimeter project: Technical Design Report", CMS-TDR-2, CERN/LHCC 97-031, (1997).

[27] The CMS Collaboration, "Performance of the CMS drift tube chambers with cosmic rays", Journal of Instrumentation, vol. 5, T03015, (2010).

[28] The CMS Collaboration, "Performance of the CMS cathode strip chambers with cosmic rays", Journal of Instrumentation, vol. 5, T03018, (2010).

[29] R.Santonico and R.Cardarelli,"Development of resistive palte counters" Nuclear Instruments and Methods in Physics Research 187, 1981.

[30] M. Abbrescia, P. Fonte, V. Peskov, "Resistive Gaseous Detectors: designs, performance, and perspectives", Wiley-VCH, 2018.

[31] M. Abbrescia et al., "Properties of $C_2H_2F_4$ based gas mixtures for avalanche mode operation of Resistive Plate Chambers", CMS Note 97/004.

[32] P. Camarri et al. "Streamer suppression with SF6 in RPCs operated in avalanche mode", Nuclear Instruments and Methods in Physics Research, 414, 1998.

[33] E. Zeballos et al. "Effect of adding SF6 to the gas mixture in a multigap resistive plate chamber", Nuclear Instruments and Methods in Physics Research, 419, 1998.

[34] M.Abbrescia et al., "Resistive Plate Chambers in avalanche mode: a comparison between model prediction and experimental results", Nuclear Instruments and Methods in Physics Research, 1998.

[35] M.Abbrescia et al., "Performance of Resistive Plate Chambers for the muon detection at CMS", Nuclear Instruments and Methods in Physics Research, 1999.

[36] G. Pugliese, The CMS Muon Collaboration,"The RPC system for the CMS experiment", 2006 IEEE NSS Conference Record N24-3, Jan (2007).

[37] K.S. Lee et al. [CMS Collaboration], "Production of gas gaps for the Forward RPCs of the CMS experiment", Nuclear Instruments and Methods in Physics Research A, 2005.

[38] CMS Collaboration, "Technical proposal for the upgrade of the CMS detector through 2020", Technical Report CERN-LHCC-2011-006. LHCC-P-004, CERN, Geneva, Jun 2011.

[39] F. Loddo et al., "Front-end for the RPC detector in CMS", Proceedings of the 4th International Workshop on Resistive Plate Chamber and Related Detectors, Napoli, Italy, 15-16 October 1997.

[40] V. Khachatryan et al., "The CMS trigger system", JINST 12, P01020 (2017).

[41] The CMS Collaboration, "CMS The TriDAS Project:Technical Design Report", CERN-LHCC-2002-026, 2002. https://cds.cern.ch/record/578006.

[42] A. Tapper et al. [CMS Collaboration], "CMS Technical Design Report for the Level-1 Trigger Upgrade", CERN-LHCC-2013-011. CMS-TDR-12, 2013.

[43] CMS Trigger and Data Acquisition Group, "The CMS high level trigger", Eur. Phys. J.C, vol. 46, (2006). https://dx.doi.org/10/1140/epjc/s2006-02495-8.

[44] CMS Collaboration,"Technical Proposal for the Phase-II Upgrade of the CMS Detector", Technical Report CERN-LHCC-2015-010. LHCC-P-008. CMS-TDR-15-02, 2015.

[45] CMS Collaboration, "The Phase-2 Upgrade of the CMS Muon Detectors", CERN-LHCC-2017-012. CMS-TDR-016, 2017.

[46] CMS Collaboration, "The Phase-2 Upgrade of the CMS Tracker", CERN-LHCC-2017-009. CMS-TDR-014, 2017.

[47] CMS Collaboration, "The Phase-2 Upgrade of the CMS Endcap Calorimeter", CERN-LHCC-2017-023. CMS-TDR-019, 2017.

[48] CMS Collaboration, "The Phase-2 Upgrade of the CMS Barrel Calorimeter", CERN-LHCC-2017-011. CMS-TDR-015, 2017.

[49] CMS Collaboration, "The Phase-2 Upgrade of the CMS Level-1 Trigger - Interim Report to the LHCC", Technical Report CERN-LHCC-2017-013. CMS-TDR-017, 2017.

[50] The European Parliament and the Council of the European Union, "Regulation (EU) No 517/2014 of 16 April 2014 on fluorinated greenhouse gases", technical report, EU, 2014.

[51] G. Pugliese et al., "Long-term performance of double gap resistive plate chambers under gamma irradiation", Nuclear Instruments and Methods in Physics Research A 477, 2002.

[52] M. Abbrescia et al., "Study of long-term performance of CMS RPC under irradiation at the CERN GIF", Nuclear Instruments and Methods in Physics Research A, 2004. doi:10.1016/j.nima.2004.07.009.

[53] H. C. Kim et al., "Quantitative aging study with intense irradiation tests for the CMS forward RPCs", Nuclear Instruments and Methods in Physics Research A, 2009. doi:10.1016/j.nima.2008.12.140.

[54] CMS Collaboration, "CMS RPC system operation and performance during LHC Run II data-taking", to be submitted, 2019.

[55] M. A. Shah [CMS Collaboration], "The CMS RPC detector performance during LHC Run-II data taking", PoS EPS HEP2017, 2018. doi:10.22323/1.314.0804.

[56] J. Goh [CMS collaboration], "CMS RPC efficiency measurement using the tag-and-probe method", Journal of Instrumentation, 2018.

[57] M. Abbrescia et al., "HF production in CMS-Resistive Plate Chambers", Nuclear Physics B, 2006.

[58] R. Guida et al., "HF production in CMS-Resistive Plate Chambers", Nuclear Instruments and Methods in Physics Research, 2006.

[59] R. Guida et al., "Results about HF production and bakelite analysis for the CMS Resistive Plate Chambers", Nuclear Instruments and Methods in Physics Research, 2008.

[60] C. Lu et al., "RPC electrode material study", Nuclear Instruments and Methods in Physics Research, 2009.

[61] G. Aielli et al., "Fluoride production in RPCs operated with F- compound gases", Nuclear Physics B, 2006.

[62] H. R. Band et al., "Study of HF Production in BaBar Resistive Plate Chambers", Nuclear Instruments and Methods in Physics Research, 2008.

[63] L. Alvigini, "Studies on impurities in the gas mixture of CERN LHC particle detectors", Thesis, 2018.

[64] A. Gelmi et al. [CMS Muon Collaboration & CERN EP-DT group], "Fluoride production in CMS Resistive Plate Chambers and aging study", PoS EPS HEP2019, 2019.

[65] R. Guida [EN and EP and AIDA GIF++ Collaborations], "GIF++: A new CERN Irradiation Facility to test large-area detectors for the HL-LHC program", PoS ICHEP2016, vol.260, 2016.

[66] D.A. Skoog, "Analytical Chemistry", Saunders College Publishing, 2000.

[67] A. Gelmi et al. [CMS Muon collaboration], "Longevity studies on the CMS-RPC system", Journal of Instrumentation, 2018. doi.org/10.1088%2F1748-0221%2F14%2F05%2Fc05012.

[68] A. Gelmi et al. [CMS Muon collaboration], "Long-term aging studies on Resistive Plate Chambers (RPC) of the CMS muon system for HL-LHC", IEEE Xplore, 2018. doi: 10.1109/NSSMIC.2018.8824516.

[69] M. Abbrescia et al., "Resistive plate chambers performances at cosmic rays fluxes", Nuclear Instruments and Methods in Physics Research A, 1995.

[70] M. Abbrescia et al., "Resistive plate chambers performances at low pressure", Nuclear Instruments and Methods in Physics Research A, 1997.

[71] G. Aielli et al., "Further advances in aging studies for RPCs", Nuclear Instruments and Methods in Physics Research A, 2003.

[72] S. M . Mari et al., "Study of the performance of standard RPC chambers as a function of bakelite temperature", Nuclear Instruments and Methods in Physics Research A 508, 2003.

[73] S. H. Ahn et al., Nucl. Instr. Meth. A 451, 582 (2004).

[74] D. Domenici et al., "An extensive aging study of bakelite Resistive Plate Chambers", Nuclear Instruments and Methods in Physics Research A, 2004.

[75] M. Abbrescia et al., "Cosmic ray tests of double-gap resistive plate chambers for the CMS experiment", Nuclear Instruments and Methods in Physics Research A 550, 2005.

[76] A. Fagot and S. Carrillo, "GIF++ Offline Analysis v6", 2017. URL : $https$: $//github.com/afagot/GIF_Offline Analysis$.

[77] G. Pugliese et al., "Aging study for resistive plate chambers of the CMS muon trigger detector", Nuclear Instruments and Methods in Physics Research A, 2003.

[78] G. Carboni et al., "An extensive aging study of bakelite Resistive Plate Chambers", Nuclear Instruments and Methods in Physics Research A, 2004.

[79] G. Aielli et al., "RPC ageing studies", Nuclear Instruments and Methods in Physics Research Section A: Accelerators, Spectrometers, Detectors and Associated Equipment, 2002. doi:10.1016/S0168-9002(01)01770-3.

[80] G. Ramirez et al. [CMS Collaboration], "Search for Heavy Stable Charged Particles in the CMS Experiment using the RPC phase II upgraded detectors", JINST, 2019.

[81] K. S. Lee et al., "Radiation tests of real-sized prototype RPCs for the Phase-2 Upgrade of the CMS Muon System", JINST, 2016. doi:10.1088/1748-0221/11/08/C08008, arXiv:1605.00440.

[82] K.S. Lee et al., "Thin Double-gap RPCs for the Phase-2 Upgrade of the CMS Muon System", CMS-NOTE-2017-005, CERN, Geneva Switzerland, 2017.

[83] K. S. Lee [CMS Collaboration], J. Instrument 11 C08008, 2016.

[84] K.Shchablo et al., "Performance of the CMS RPC upgrade using 2D fast timing readout system", Nuclear Instruments and Methods in Physics Research Section A, 2019.

[85] J. Fleury et al., "Petiroc, a new front-end asic for time of flight application", IEEE Nuclear Science Symposium and Medical Imaging Conference, 2003.

[86] A. Gelmi et. al [CMS Muon collaboration], "Background rate study for the CMS improved-RPC at HL-LHC using GEANT4", Nuclear Instruments and Methods in Physics Research Section, 2019. doi.org/10.1016/j.nima.2018.10.046.

[87] GEANT website: "https://geant4.web.cern.ch/"

[88] S. Agostinelli et al., "Geant4a simulation toolkit", Nuclear Instruments and Methods in Physics Research Section A, 2003.

[89] J. Allison et al., "Geant4 developments and applications", IEEE Transactions on Nuclear Science, vol. 53, 2006. doi: 10.1109/TNS.2006.869826

[90] J. Allison et al., "Recent developments in Geant4", Nuclear Instruments and Methods in Physics Research Section A, 2016.

[91] D. Pfeiffer, "The radiation field in the Gamma Irradiation Facility GIF++ at CERN",arXiv:1611.00299v3, 2017.

[92] PHYTIA website: "http://home.thep.lu.se/ torbjorn/Pythia.html"

[93] Fluka website: "http://www.fluka.org/fluka.php".

[94] A. Ferrari et al., "FLUKA: a multi-particle transport code", CERN 2005-10 (2005), INFN/TC-05/11, SLAC-R-773.

[95] T.T. Bohlen et al., "The FLUKA Code: Developments and Challenges for High Energy and Medical Applications", Nuclear Data Sheets 120, 2014.

[96] J. T. Rhee et al., "Study of the neutron sensitivity for the double gap RPC of the CMS/LHC by using GEANT4", Journal Korean Physics Society, 2006.

[97] Reimer, L., "Scanning Electron Microscopy", Springer-Verlag, Berlin, 1985.

[98] Vertical Scanning Interferometry (VSI) reference technical manual: "http://erc.ncat.edu/Facilities/Manuals/Wyko.pdf".

[99] Russ, J. C., "Fundamentals of Energy Dispersive X-ray Analysis", Butterworths, London, 1984.

[100] E. Fatarait, "Viscosity and Surface Properties of Melamine-Formaldehyde Resin Composition", Materials Science, 2009.

[101] Epoxy glue technical data sheet "https://multimedia.3m.com/mws/media/66122O/3mtm-scotch-weld-tm-epoxy-adhesive-dp460-ns-and-off-white.pdf".

[102] C. Fornaini et al., "Role of surface tension and roughness on the wettability of Er:YAG laser irradiated dentin: In vitro study", J-STAGE, 2013. doi: 10.5978/islsm.13-OR-15

[103] K.J. Kubiak et al.," Wettability versus roughness of engineering surface", 2011.

[104] L. Benussi et al., "A study of HFO-1234ze (1,3,3,3-Tetrafluoropropene) as an eco-friendly replacement in RPC detectors", 2015. arXiv:1505.01648 [physics.ins-det].

[105] M. Abbrescia et al., "Preliminary results of Resistive Plate Chambers operated with eco-friendly gas mixtures for application in the CMS experiment", JINST, 2016. doi:10.1088/1748-0221/11/09/C09018.

[106] L. Benussi et al., "Properties of potential eco-friendly gas replacements for particle detectors in high-energy physics", 2015.

[107] J.S. Brown, "HFOs new low global warming potential refrigerant", ASHRAE J., 2009.

[108] R. Guida et al., " Characterization of RPC operation with new environmental friendly mixtures for LHC application and beyond", Journal of Instrumentation, 2016. doi.org/10.1088/2F1748-0221/2F11/2F07/2Fc07016

[109] B. Mandelli et al., "Performance studies of RPC detectors with new environmentally friendly gas mixtures in presence of LHC-like radiation background", Nuclear Inst. and Methods in Physics Research, 2019.

[110] G. Rigoletti et al. [Ecogas collaboration], "Studies of RPC detector operation with eco-friendly gas mixtures under irradiation at the CERN Gamma Irradiation Facility", PoS EPS HEP2019, 2019.

[111] The CMS Collaboration, "The CMS trigger system", IOP, 2017. doi: 10.1088/1748-0221/12/01/p01020.

[112] A. Tapper [CMS Collaboration], "The CMS Level-1 Trigger for LHC Run II", PoS, 2017.

[113] L. Cadamuro [CMS Collaboration], "The CMS Level-1 trigger system for LHC Run II", JINST 12 C03021, 2017.

[114] J. Heikkila [CMS Collaboration], "The CMS Level-1 muon trigger for the LHC Run II", PoS, 2018.

[115] J. Ero et al., "The CMS Level-1Trigger Barrel Track Finder", JINST 11 C03038, 2016.

[116] A. Triossi et al., "The CMS Barrel Muon trigger upgrade", JINST 12 C01095, 2017.

[117] CMS collaboration, "Muon Reconstruction in the CMS Detector", CMS AN 2008/097, 2009.

Acknowledges

I wish to thank all the people who made this possible.

I want to thank Prof.ssa Gabriella Pugliese, my supervisor, for giving me the opportunity to work in a so amazing place like CERN, for her guidance, support and time.

A big thank goes to the people involved in the CMS RPC group, which for me represents a big family. I learned something from everyone, and without their help this work would not have been possible.

Finally, thanks to all the people I meet in Bari, for their kindness, and for welcoming me to a lovely city.